Aerodynamic Sensitivity Analysis of the Symmetric Generic Cyclist Model

An Experimental Study

Fleur Vermeulen

Delft University of Technology

TU Delft

Aerodynamic Sensitivity Analysis of the Symmetric Generic Cyclist Model

An Experimental Study

by

Fleur Vermeulen

to obtain the degree of Master of Science
in Aerospace Engineering, specialising in Aerodynamics
at the Delft University of Technology,
to be defended publicly on June 12th, 2026

Student Number:	5071372	
Project Duration	November 2025 - June 2026	
Thesis Committee:	A. Sciacchitano	TU Delft, supervisor
	B.W. van Oudheusden	TU Delft, chair
	L.T. Lima Pereira	TU Delft, examiner

The cover image is generated by AI and should not be taken as accurate

TU Delft

Preface

This thesis, ”Aerodynamic Sensitivity Analysis of the Symmetric Generic Cyclist Model”, marks the end of my MSc Aerodynamics at the Delft University of Technology. Seven years after starting my BSc Aerospace Engineering, I have finally reached my goal: being an Aerodynamics Engineer.

This thesis allowed me to combine my two main interests, sports and aerodynamics. This research is a continuation of previous experiments conducted by Delft University of Technology on the importance of aerodynamics in cycling. During this thesis, I was able to broaden my aerodynamic knowledge by analysing multiple papers on cyclists and using this new information to perform my own wind tunnel experiment. During the experiment, I learned new wind tunnel techniques, software and how to process data for aerodynamic analysis.

I would like to thank my parents for their support and understanding during this thesis, but also during all my years at university, they have gotten me where I am today. Because of them, I have been able to reach my goals and get my dream job.

Finally, I would like to thank my supervisor, Andrea Sciacchitano, for the opportunity to work on this topic and for his feedback and weekly meetings. I also want to thank Wouter Terra for his knowledge on the Generic Cyclist Model and the aerodynamics of cyclists, and for his help during the wind tunnel experiment. Lastly, I want to thank Sajad and José for their help during this thesis.

Fleur Vermeulen
Delft, May 2026

Abstract

Most of the resistance a cyclist must overcome is the aerodynamic drag. To investigate the aerodynamic performance of a cyclist and to reduce the drag, multiple experiments have been performed all around the world. However, each experiment used its own cyclist model, all with different dimensions and for privacy, the geometry is not shared. This limits the follow-up experiments and overall understanding of the cyclists' aerodynamics. To reduce these limitations, a Generic Cyclist Model (GCM) has been developed, and its geometry has been made public. The GCM is positioned in the asymmetric leg position, one leg extended and the other bent, as this yields the highest drag configuration. However, this is not the only leg position a cyclist has during their ride. For this reason, the aerodynamic performance of the lower drag configuration, the symmetric leg position, is analysed. The symmetric GCM is rarely tested during experiments, leading to a gap in the understanding of the aerodynamics of cyclists.

The Symmetric GCM is tested in the wind tunnel to understand the aerodynamic sensitivity and the difference from the Asymmetric GCM. The sensitivity is tested in four categories: the influence of the change in leg positions, the influence of the Reynolds number variation, the influence of crosswind and the influence of the addition of passive flow control devices.

The experiment with the Symmetric and Asymmetric GCM is performed in the open-jet wind tunnel of Delft University of Technology. By using a force balance and 3D particle image velocimetry, or Lagrangian particle tracking, the aerodynamic performance of the cyclist is measured. The drag area, velocity flow field and vorticity flow field give the necessary information to analyse the sensitivity.

The results show that the position of the legs has a great influence on the aerodynamics of the cyclist. A reduction of 4.6% was seen compared to the Asymmetric GCM, which is caused by the reduction of leg wake and repositioning and weakening of the vortices.
The variation in Reynolds number yields a drag area reduction as the velocity is raised. This is caused by the critical Reynolds number; the increase in velocity triggers a transition, causing the airflow to stay attached to the object longer, resulting in a smaller wake. This behaviour is spotted in the velocity flow fields of the left leg, while less for the body wake. This indicates that the leg wake has a great influence on the overall drag area of the cyclist, rather than the body wake having the predominant influence.
The crosswind experiment demonstrates a symmetrical-like behaviour in drag area reduction for the Symmetric GCM, while a non-symmetrical behaviour for the Asymmetric GCM. The rotation of the straighter leg into the airflow yields a larger drag reduction than the opposite rotation. This is mainly caused by the reduction in the left leg wake of the GCM.
Flow control devices are added on the hips, upper arms and legs of the Symmetric GCM. The vortex generators on the hips showed a drag area increase due to the early triggering of the separation. The addition of zigzag strips on the upper arms and lower legs results in drag area reduction, as the wake of the cyclist is affected.

A conclusion can be drawn from the drag area reduction and flow field alterations. The aerodynamics of the legs play a great part in the drag of the cyclist, with small changes to the legs leading to large effects on the drag area.

Keywords: Aerodynamics, Cyclist Aerodynamics, Generic Cyclist Model, PIV, Particle Image Velocimetry, 3D PTV, Wind Tunnel

Contents

List of Figures

List of Tables

Nomenclature

Abbreviations

	Definition		Definition
BL	Boundary Layer	OJF	Open Jet Facility
CAD	Computer-Aided Design	PIV	Particle Image Velocimetry
CFD	Computational Fluid Dynamics	PTV	Particle Tracking Velocimetry
CCR	Counter-Clockwise Rotating	STB	Shake-The-Box
CR	Clockwise Rotating	VG	Vortex Generator
GCM	Generic Cyclist Model	WOF	Wind Off
HFSB	Helium-filled Soap Bubbles	WON	Wind On
LPT	Lagrangian Particle Tracking		

Symbols

Symbol	Definition	Unit
A	Frontal Area	$[m^2]$
c	Characteristic length	$[m]$
C_D	Drag Coefficient	$[-]$
$C_D A$	Drag Area	$[m^2]$
d	Distance between flow field plane and saddle	$[mm]$
e	Chord length	$[mm]$
F_D	Drag Force	$[N]$
h	Height	$[mm]$
L	Hip length	$[m]$
P	Power	$[N]$
p	Pressure	$[Pa]$
R	Air Gas Constant	$[J/kgK]$
R_e	Reynolds Number	$[-]$
S	Sutherland Temperature	$[K]$
s	Spacing between counter-rotating vanes	$[mm]$
T	Temperature	$[K]$
U	Velocity	$[m/s]$
U_∞	Freestream velocity	$[m/s]$
u	Lateral velocity	$[m/s]$
v	Vertical velocity	$[m/s]$
w	Streamwise velocity	$[m/s]$
X_{VG}	Distance between separation line and leading edge	$[mm]$
x	Lateral Distance	$[mm]$
y	Vertical Distance	$[mm]$
z	Distance between vortex generator pairs	$[mm]$
β	Incidence angle	$[^\circ]$
δ	Boundary layer thickness	$[mm]$
ψ	Crosswind angle	$[^\circ]$
ρ	Density	$[kg/m^3]$
μ	Dynamic Viscosity	$[kg/ms]$

1

Introduction

In the world of cycling, it all comes down to one thing: being the fastest to the finish line. As every second counts in the race, the rider's strength is not the only thing that can lead to a win; aerodynamics plays an important role. Studies on the aerodynamics of cyclists have measured that 90% of the total resistance a rider experiences is caused by aerodynamic drag at speeds exceeding the $40\ km/h$, [12]. Others show that the aerodynamic drag has a variation of around 15% during paddling, [6]. The highest drag resistance has been measured at an asymmetric leg position, one leg straight and the other bent, while the lower resistance occurs at a symmetrical position. Furthermore, the wind, especially the angle at which the cyclist reaches the wind, plays a crucial role in the amount of drag a cyclist experiences, [16]. Besides this, fundamental aerodynamic phenomena and studies on bluff bodies have shown different ways of reducing the drag.

To be able to fully understand the aerodynamic performance of cyclists, a Generic Cyclist Model (GCM), an average of fourteen individual cyclists, has been made. The geometry and dimensions of the GCM have been shared all around the world to increase the amount of follow-up wind tunnel experiments [25]. This thesis will utilise the GCM with a modification surrounding the position of the legs, changing from an asymmetric to a symmetric posture. As no prior experiments have been done on the symmetric GCM, the exact aerodynamic sensitivity of the cyclist is unidentified.

Hence, the goal of this thesis will be to research the aerodynamics of the Symmetric Generic Cyclist Model and to answer the research question "*What is the aerodynamic sensitivity of the Symmetric Generic Cyclist Model and how does it differ from the Asymmetric Generic Cyclist Model?*". This will be analysed based on the effect of four different categories on the aerodynamics of the cyclist: the influence of the leg position, the influence of Reynolds Number variations, the influence of crosswind and the influence of adding passive flow control devices. To investigate these influences, the categories are split into the effect on the aerodynamic load, drag area, and the effect on the aerodynamic flow field, especially on the wake and vorticity of the cyclist.

This thesis has been structured in the following way: In chapter 2, the background of cycling aerodynamics as well as prior studies are investigated. Conclusions from the studies have lead to objective and associated research questions. The methodology involved in this thesis is discussed in chapter 3. This entails the facility used, the set-up and equipment required for the experiments and the test plan to ensure all data required to answer the research questions will be tested. Furthermore, a detailed description of the post-processing of the data is given, and the corrections that have been performed are discussed. The outcome of the experiments will be discussed in chapter 4. This entails the analysis of the aerodynamic sensitivity of the cyclist based on the research questions. The results will show both a numerical analysis, mainly the drag area, as well as a visual analysis of the flow field. The conclusion of this thesis and a discussion are provided in chapter 5. Finally, recommendations for future work on the Generic Cyclist Model and other cyclist experiments are given in chapter 6.

2

Literature Study

Aerodynamics plays an important role in the performance of a cyclist. For this reason, multiple computational and experimental studies on cyclist aerodynamics have been performed to increase the chances of winning. Almost all of the studies have shown that the most important thing is the reduction of drag. Research on the sensitivity of the position of the cyclists, the flow conditions, the equipment and the passive flow control devices became crucial to understand. In this chapter, the aerodynamic importance and prior studies are discussed.

2.1. Background

The velocity the cyclist is able to achieve is based on the cyclist's power and the forces working against him. One of the main forces that works against the cyclist is the aerodynamic drag force. Hence, the power and aerodynamic characteristics of a cyclist must be understood to improve performance.

2.1.1. Cycling Power

For a cyclist to move forward, they must overcome multiple forces, such as aerodynamic force, friction, etc, [17]. A schematic image of the forces' action on the cyclist during an uphill climb is presented in Figure 2.1. During an uphill climb, the cyclist's weight must also be overcome, while for a downhill climb, the weight works beneficially as less power is needed to overcome the aerodynamic drag, friction, etc.

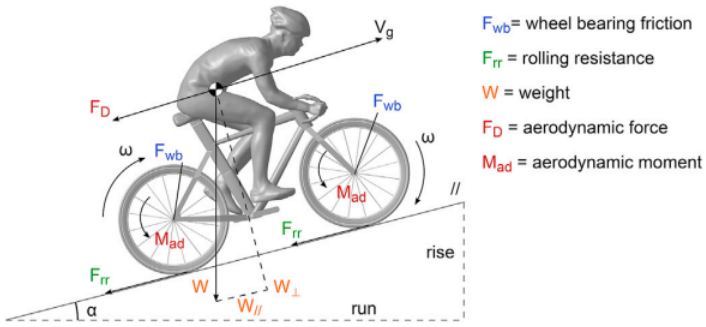

Figure 2.1: Schematic drawing of forces acting on a cyclist during an uphill climb, [17]

A study, [19], generated a mathematical formulation of the power to overcome the power caused by resistance, which is given in Equation 2.1. This study, [19], showed that the aerodynamic drag, or the resistance caused by aerodynamics, was the largest, which is approximately 56% up to 96% of the total resistance for uphill and downhill directions, respectively. Similarly, a study by Kyle and Burke (1964) [12] indicated that 90% of the total resistance is attributed to aerodynamic drag at high velocities.

$$P = P_{Aerodynamic} + P_{Rolling\ Resistance} + P_{Wheel\ Baring} + P_{Potential\ Energy} + P_{Kinetic\ Energy} \quad (2.1)$$

As stated above, aerodynamic drag is the biggest resistance that a cyclist must overcome. Thus, it can be said that the power formulation can be simplified to Equation 2.2. Rewriting the $P_{Aerodynamics}$, shows that the main influence is the drag force the cyclist experiences, and thus must be reduced.

$$P \approx P_{Aerodynamics} \approx F_D \cdot U \tag{2.2}$$

The drag force depends on the flow conditions, such as density, ρ, and the velocity, U, and on the cyclists frontal area, A and the drag coefficient, C_D, [17], see Equation 2.3. From this, it can be concluded that the cyclist should reduce their frontal area and the drag coefficient to decrease the drag force. These parameters are named to be the drag area of the cyclist, $C_D A$, and can be changed by altering the cyclist's posture and clothing.

$$\text{Drag Force:} \quad F_{Drag} = \frac{1}{2}\rho C_D A U^2 \qquad \text{Drag area:} \quad C_D A = \frac{F_{Drag}}{\frac{1}{2}\rho U^2} \tag{2.3}$$

2.1.2. Bluff Body Aerodynamics

Before the drag can be reduced for a cyclist, the aerodynamic principles must be understood. Cyclists are often considered bluff bodies as they display large separation regions, [7]. Due to the bluff body characteristic, most of the aerodynamic resistance (or drag) is caused by pressure drag, [10]; turbulent wake and low-pressure vortices that occur behind the cyclist. These are caused by the separation of the airflow from the body. The pressure drag, and its magnitude, stems from the difference in the high pressure in front of the cyclist and the low pressure behind it, [18]. Therefore, to decrease the pressure drag, the pressure difference around the body must be reduced. This reduction can be done by increasing the low pressure behind the cyclist, which is done by reducing the wake (the area of disturbed airflow).

The width of the area of disturbed airflow, the wake width, of bluff bodies such as cylinders and cyclists, depends on the Reynolds number. This number is related to the velocity of the airflow and can indicate whether the airflow separation is laminar or turbulent. According to Achenbach [1] [2], for a low (sub-critical) Reynolds number, $R_e < 10^5$, the flow separation is laminar, meaning the boundary remains smooth over the geometry until separation occurs, which happens around the shoulder region of the cylinder. This results in a wide wake and thus a high drag coefficient. As can be seen in Figure 2.2, the cylinder in sub-critical condition shows a wide wake due to this laminar separation, [27]. Increasing the Reynolds number shows an effect on the wake width of the cylinder. With a critical Reynolds number, $10^5 < R_e < 5 \cdot 10^5$, the flow is in a transition state, as the flow goes from laminar to turbulent separation. This transition triggers the reattachment of the separated flow to the boundary layer, leading to a longer attached flow. Visualised in Figure 2.2, this leads to a small wake width and results in a reduced drag coefficient. This reattachment causes the separation line on the cylinder to move downstream. The Reynolds number can be adjusted by changing the velocity, Equation 2.4 and keeping the density, ρ, characteristic length, c and kinematic viscosity, ν, constant, [7]. This effect of the critical Reynolds number on bluff bodies can be utilised to reduce the drag area of the cyclist.

$$R_e = \frac{\rho U c}{\nu} \tag{2.4}$$

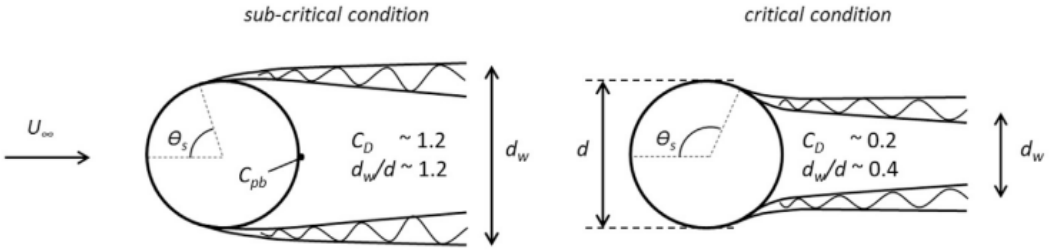

Figure 2.2: Schematic drawing of the wake in low (sub-critical) and critical Reynolds numbers, [27]

2.2. Prior Studies on Cyclists and Bluff Bodies

As has become clear, the aerodynamic drag of the cyclist must be analysed and reduced to become faster. For this reason, multiple studies over the years on cyclists as well as bluff bodies have been performed on the posture, flow conditions and flow control devices.

2.2.1. Position of the Cyclist

The position of the cyclist has the biggest influence on the aerodynamics, as the wake is generated around the bluff bodies and the position alters the frontal area, A. The position of the cyclist can be changed in several ways: the posture (bending of the upper body), the leg position, the arm position and the head position. Based on this, a few different studies have been performed.

2.2.1.1. Effect of the Cyclist Posture

The posture of the cyclist influences the aerodynamic drag; therefore, an experimental study has been performed comparing three postures, [8]. The rider is placed in an upright, dropped or time trial position, as visualised in Figure 2.3, and placed in a wind tunnel at a velocity of $10\ m/s$. The drag area of each position has been measured and compared. According to the paper [8], the lowering of the cyclist's head leads to a lower frontal area and thus a reduced drag area. The time trial posture shows the lowest frontal area and reduces the frontal area by 31% compared to the upright position. Compared to the dropped position, the time trial decreases the area by 20%. Analysing the drag area, a reduction of 22% and 13%, respectively, for the time trial posture. The combination result is a smaller reduction due to the interaction between the aerodynamics of the bicycle and the cyclist and the influence of the drag coefficient, C_D.

Figure 2.3: Cyclist position: (a) Upright, (b) Dropped, (c) Time trial, [8]

2.2.1.2. Effect of Leg Position on the Aerodynamic Drag

The cyclist's position changes during the ride as he pedals, meaning the configuration and thus position of the leg differ. During an experimental study [6], the effect of the leg position on the flow topology, and thus aerodynamics, is investigated. For this study, a mannequin with similar dimensions of a male cyclist was placed in a time trial position and placed in an open jet wind tunnel. With the use of pressure taps, the aerodynamic drag and the flow field are visualised. The mannequin's leg positions are changed by rotating them around the panel, this is done in increments of $15°$. These changes by rotation are called changes in the crank angle of the rider. The measurements of the experiment are done over a full circle, $360°$. The circle or crank cycle can be split into two halves, $0° - 180°$ and $180° - 360°$, as they are opposites of each other.

The experiment shows that the crank angle has a large effect on the aerodynamic drag, as it has a variation of approximately 20% in drag over the crank cycle. Next to this, comparing both halves to each other shows a small variation, no more than 5%, indicating that the model is in a symmetry. The outcome of the study in terms of aerodynamic drag is plotted in Figure 2.4, which clearly indicates that the drag area as well as drag coefficient are highest at the crank angles $75°$ and its opposite position $255°$. This is the position with one extended leg and the other bent. The lowest drag position happens at $0°$ and $180°$, which are the symmetrical positions, since the upper legs are symmetrical to each other. The position of the legs influenced the hip angles, as an extended leg leads to a large hip angle while a raised leg leads to a small hip angle. In other terms, the hip angle is directly related to the crank angle. This relation is plotted in the second graph of Figure 2.4, which shows, for example, that a crank angle of $90°$ has a hip angle of approximately $75°$ for the left hip and $15°$ for the right. The changes in crank angle and hip angle, thus leg position, have an effect on the frontal area, and consequently on the drag

area, which is plotted in the first graph. As can be seen, the highest drag coefficient and the highest frontal area happen at the same crank angle, hence at this angle at which the drag area is the largest. The drag area variation is a combination of the variation of the frontal area and the drag coefficient. However, as the frontal area variations are within 2% of each other, this cannot be the reason for the drag area variation. Hence, the drag coefficient variation, which has a maximum variation of 15%, is the main contributor to the drag area variation.

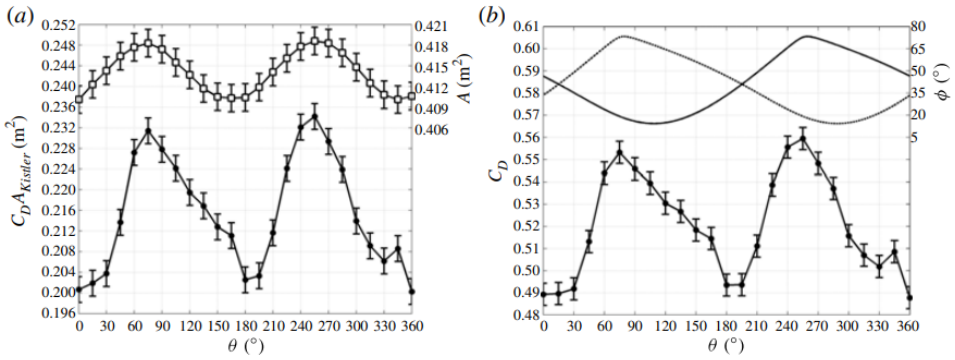

Figure 2.4: Variation in (a) drag area (line: $-\bullet-$) and frontal area (line: $-\square-$), and (b) drag coefficient (line: $-\bullet-$) and hip angle (left hip: $(-)$, right hip: $(\cdots)$), with respect to crank angle [6]

Based on the drag coefficient findings, it can be concluded that the crank angle affects the flow field around the cyclist [6]. Based on the flow field data, retrieved with the use of probes, it can be seen that the variations are primarily caused by the flow separation from the hips and the lower back of the rider. The flow separations lead to rotations in the airflow; these vortex structures are visualised in Figure 2.5, for both symmetrical and asymmetrical leg positions. In the symmetrical, low-drag position, symmetrical vortices are formed from the inner thigh and upper hips. As can be seen, the four vortices, are in a quadrupole arrangement and are symmetrical around the centre axis. The left side of the mannequin leads to clockwise rotation vortices, while the right side generates an anti-clockwise rotation. On the other side, in the asymmetric, high drag position, the vortices are at different locations. For the raised leg, an inner thigh vortex is present, while it is not for the lowered leg. Furthermore, there is no upper hip vortex present for the raised leg position, compared to the lower leg, where there are two vortices at the upper and lower hip. This leads to an asymmetric vortex structure that lasts longer than for the symmetric condition. Due to this, the wake is larger, and its drag is higher.

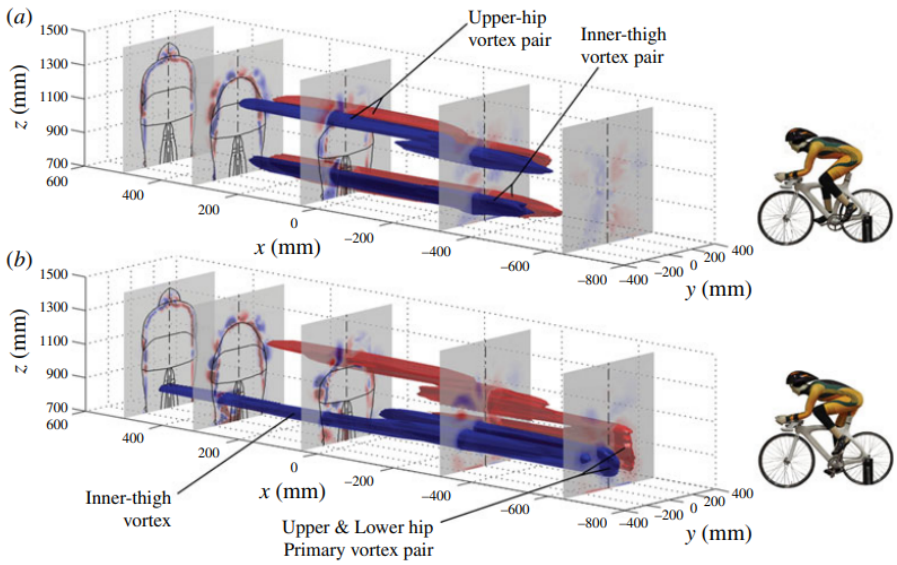

Figure 2.5: The vortex structures around the cyclist in (a) symmetrical, low drag position and (b) asymmetrical, high drag position. Blue indicates clockwise rotation, while red represents anti-clockwise. [6]

To provide a more distinct visualisation of the vortices of the two leg positions, a schematic drawing has been made from the left and right perspectives [6] [7], see Figure 2.6. The symmetric position shows the two counter-clockwise rotating vortices on the right side of the cyclist, one is the upper-hip vortex and the other the inner thigh. As the asymmetric position leads to different vortex locations on the left and right sides of the cyclist, two perspectives are given. The upper hip vortex on the right side, extended leg, is bigger than on the left side, bent leg.

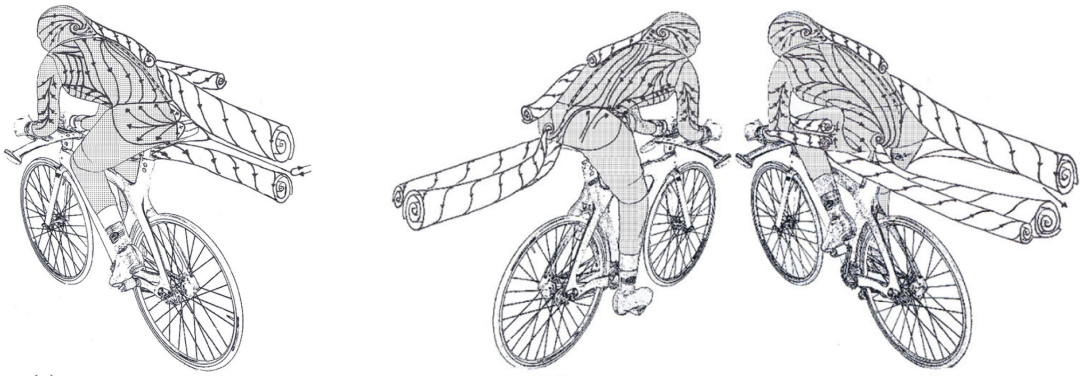

(a) Symmetric position **(b)** Asymmetric position

Figure 2.6: Schematic drawing of the vortices on the Symmetric and Asymmetric leg position [6] [7]

From this study, [6], it can be concluded that the higher drag happens at an asymmetric leg position, at crank angles $75°$ and $255°$, due to the asymmetry in the flow field caused by the vortex structure. While the lowest occurs at a symmetrical position, at crank angles $0°$ and $180°$.

2.2.1.3. Effect of the Arm Position

The position of the cyclist on the bike affects the aerodynamic performance. Therefore, the position of the arms of a male mannequin in the time trial position has been investigated using computational fluid dynamics (CFD), [15]. In the study, three different hand positions, ranging from low to high, and two elbow positions, narrow and wide, were tested. Every position and its combinations are tested with and without the bicycle to understand the effect of the bicycle itself.
From the CFD results, it was seen that the most optimal, lowest drag area position was a combination of a very high hand position and narrow elbows. This combination reduces the drag area by approximately 11% for only the cyclist, while the drag area including a bicycle is only reduced by 9.4%. When analysing the flow topology, Figure 2.7, a clear effect can be seen in the wake. The elbows generate a wake that is extended and clearly visible in the baseline topology. When narrowing the elbows, the wake becomes more contained. Similarly, by raising the hands, the upper wake becomes more contained.

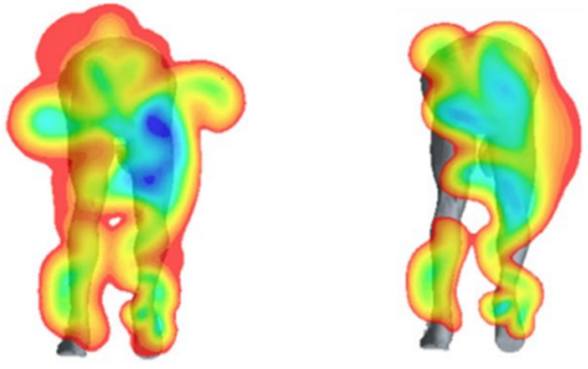

(a) Baseline **(b)** Very high hand + narrow elbows

Figure 2.7: Flow topology of the baseline and very high hand and narrow elbows at a velocity of $14\ m/s$, [15]

Furthermore, a different study on the effect of arm position on the aerodynamics has been performed, [11]. In this study, four different positions, at a velocity $15\ m/s$, were tested to understand the effect of hand and elbow position. The outcome of this study results in a similar position, keeping both hands and elbows together and raising the hands.

2.2.2. Airflow Conditions

Besides the position of the cyclist, the flow field conditions surrounding the rider influence the aerodynamic behaviour. As discussed in subsection 2.1.2, the Reynolds number, and thus incoming air velocity, has an effect on the separation, wake and drag of a bluff body. Hence, several experiments have been performed to understand the effect of Reynolds number on the cyclist. Next to this, during outside cycling races, the wind does not reach the cyclist's head on but rather at an angle. Hence, the effect of crosswind is investigated to understand whether crosswind angles affect the aerodynamic performance.

2.2.2.1. Effect of Reynolds Number Variation

A critical Reynolds number leads to a small wake and subsequently a low drag coefficient, which has been noted in numerous experiments on bluff bodies. This effect, where increasing velocity leads to a drag coefficient reduction, is also referred to as a drag crisis. As a cyclist is considered a bluff body, the drag crisis and thus the Reynolds number effect have been investigated. During the experimental study [25], a male mannequin in a time trial position and in a sprint position are placed in a wind tunnel and is placed in asymmetrical leg position, as this yields the highest drag coefficient based on the crank angle study, as explained in subsubsection 2.2.1.2. The variation in Reynolds number is tested by changing the airflow velocity, which in this study ranges from 5 to $25\ m/s$.

The outcome in drag caused by the velocity variation is plotted in Figure 2.8 for both the time trial and sprint position. As can be seen in the graphs, increasing the velocity leads to a decrease in the drag coefficient and drag area. With a decrease of approximately 15% of both positions when comparing the slowest to the fastest velocity. According to the paper [27], this Reynolds number effect is, to a certain extent, caused by the boundary layer transition over the mannequin's arms and legs. The increase in velocity leads to a delay in flow separation, resulting in a narrower wake and, consequently, a lower drag coefficient. In Figure 2.9, the effect of the increase in velocity on the wake around the upper and lower parts of the extended leg is shown. The upper part of the leg barely shows a difference when increasing the velocity; however, a slight reduction can be seen at $10\ m/s$. The lower part is more influenced by the velocity increase, as the decrease in wake, especially around the calf, is noticeable. As described earlier, the leg acts as a bluff body, which, in a critical condition, results in a narrower wake. Based on the flow topology of the lower leg shown in Figure 2.9, the critical Reynolds number is exceeding $25\ m/s$. While the upper leg has a critical velocity of around $10\ m/s$. The knee shows a different behaviour than the upper and lower leg, and seems to be in a critical condition at $20 - 25\ m/s$.

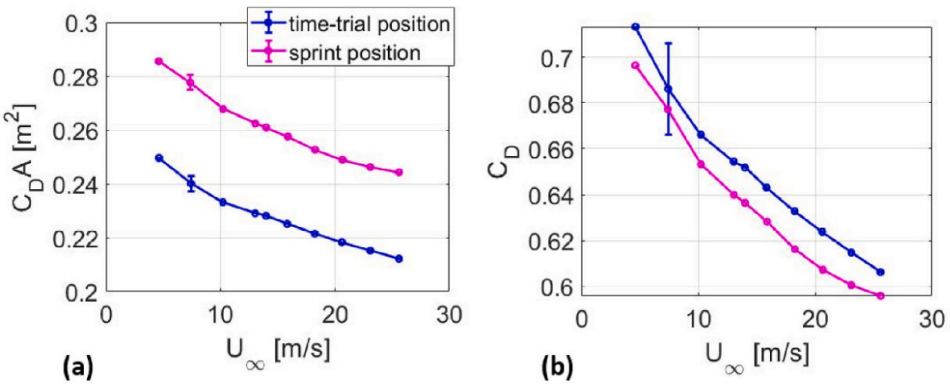

Figure 2.8: Variation in (a) drag area, and (b) drag coefficient, with respect to velocity variation, [25]

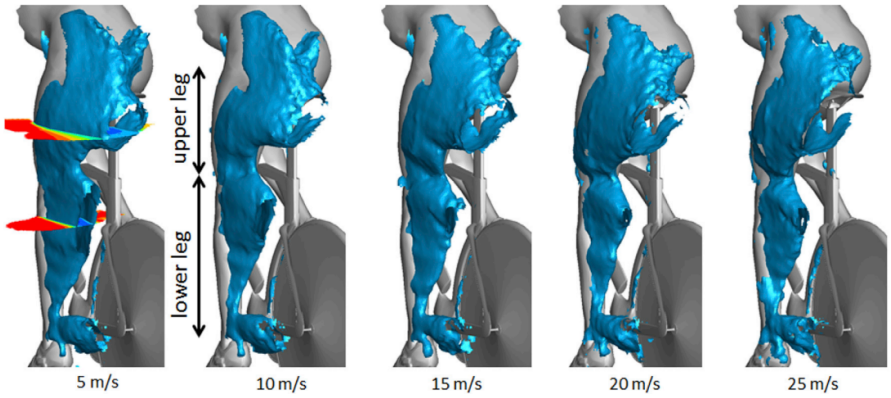

Figure 2.9: The flow field around the upper and lower part of the extended leg at different velocities, [27]

2.2.2.2. Effect of Crosswind at Different Reynolds Numbers

Commonly, during experimental studies conducted in wind tunnels, the cyclists are placed tangentially to the airflow, thereby assuming the wind to be head-on. However, a cyclist on the road experiences crosswind, leading to the airflow reaching the cyclist at an angle. Therefore, an experimental study is done on the crosswind at different Reynolds numbers to understand the aerodynamic sensitivity, [16].

This study was a continuation of the experimental study of subsubsection 2.2.2.1, and thus the same model, asymmetric position, and wind tunnel have been used. In order to analyse the crosswind, the model is placed at an angle, yaw, ranging from $-20°$ to $20°$. The outcome of the aerodynamic drag area with respect to yaw angle at different velocities is plotted in Figure 2.10. It can be seen that the negative yaw angle results are fairly constant for each velocity, while the drag area for positive yaw decreases as yaw is increased. The difference between the positive and negative yaw on the drag area is caused by the asymmetric leg position, as the left leg is in the extended position while the right leg is raised. It can also be seen that head-on wing, around $0°$ yaw angle, the drag area is the highest. From the graph, it can also be seen that increasing the velocity decreases the drag area, which is in line with the previous experiment about Reynolds number effects.

Subsequently, the flow topology is looked at for different yaw angles to have a better understanding of the effect of the yaw angle on the drag. The flow at different yaw angles is visualised in Figure 2.11. As can be seen, at $0°$ yaw, thus no cross winds, the wake behind the cyclist is largest as it covers the lower back and the extended leg fully. Compared to the negative yaw condition, the wake of the extended leg is slightly reduced and split from the lower back wake. This is in line with the plotted drag area; a slightly lower drag is noted. With regards to positive yaw, a bigger effect is seen in the wake of the cyclists. The wake of the extended leg is quite reduced, while the lower back wake is slightly increased in width. As the wake is reduced, and more energy stays in the air, the drag area is therefore lower.

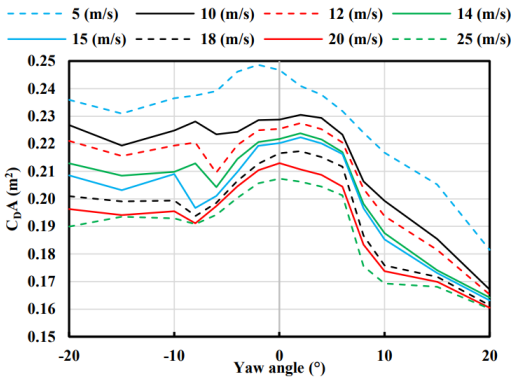

Figure 2.10: Variation in drag area with respect to yaw angle at different velocities, [16]

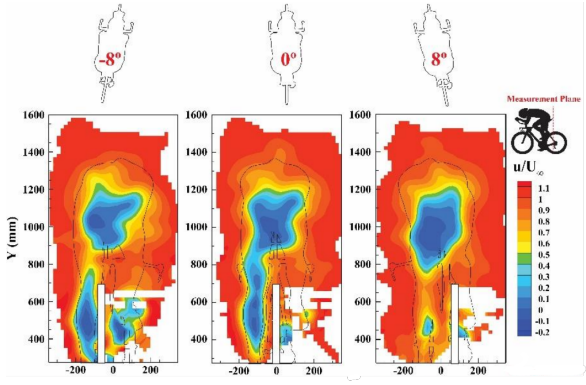

Figure 2.11: The flow topology behind the saddle at yaw angles; $-8°$, $0°$ and $8°$ at a velocity of $14\ m/s$, [16]

To summarise, this experimental study shows that crosswinds have an effect on the drag area and wake of the cyclists. Positive yaw, airflow reaching the bended leg first, has a positive effect with up to 35% reduction in drag area compared to headwind.

2.2.2.3. Effect of Turbulence Intensity

During wind tunnel experiments, the turbulence intensity is less than 2%, [4], when in reality the turbulence during outdoor conditions is much higher due to the outdoor environment and the wake of other cyclists. For this reason, the effect of the turbulence intensity on the aerodynamic performance has been investigated. During the experiment, an asymmetric male mannequin is placed in a wind tunnel in a time trial position. With the use of grids with different dimensions, the intensity of the turbulence is affected and ranges from 1% to 9%.

The paper [4] indicated that turbulence has an effect on the drag area of the cyclist. In Figure 2.12a, the drag area is plotted as a function of velocity for each turbulence intensity. As visualised, the increase in turbulence leads to a reduction in drag area, with in high turbulence the drag is reduced by approximately 22% compared to the lowest intensity. Furthermore, velocity changes have a less strong effect on the drag area at lower turbulence intensity. An intensity of 1.4% only shows a reduction of 9% when comparing the lowest to the highest velocity, while an intensity of 9.1% results in a reduction in drag area of around 26%. The effect the turbulence has on the drag area is a result of the attachment of the airflow. When the airflow is in a transition or turbulent state, it is able to stay attached longer to the body, causing a reduction in wake.
The experiment is repeated with the mannequin wearing a skin suit, in Figure 2.12b. The drag area decreases as velocity increases; however, it plateaus at velocities above $16\ m/s$. Even at some turbulence levels, the drag area increases at higher speeds. This indicates that the turbulence intensity has effects on the drag area but differs under diverse circumstances.

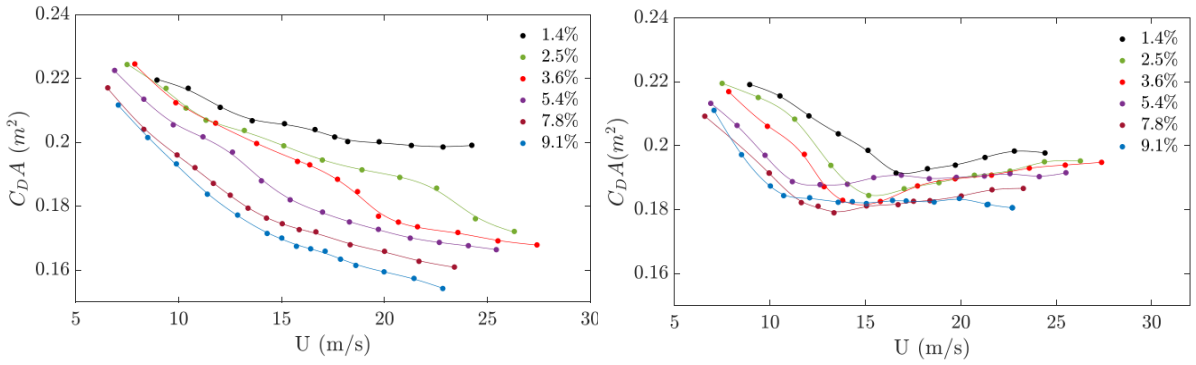

(a) Male mannequin

(b) Male mannequin wearing a skin suit

Figure 2.12: Effect of turbulence intensity on the drag area at different velocities, [4]

The flow field behind the cyclists is measured with pitot tubes [4]. The wake is visualised at the different turbulence intensities in Figure 2.13. A small increase, from 1.4% to 2.5% or to 3.6% has minor changes in the wake, with the elbow wake being slightly reduced as well as the upper wake (combination of shoulder and head). An increase to 5.4% results in significant effects, the wake of the elbows is barely present, and a reduction in wake losses is seen at the legs. The increase in turbulence intensity leads to the leg's boundary layer transitioning earlier and thus delaying separation. Increasing the intensity from 5.4% to 7.8% or 9.1% only shows mirror effects in the wake.

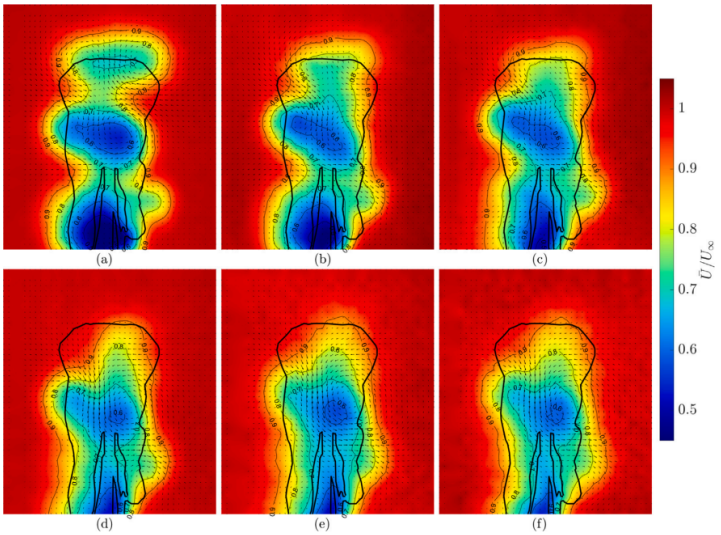

Figure 2.13: Flow field behind the cyclist at different turbulence intensities: (a) 1.4%, (b) 2.5%, (c) 3.6%, (d) 5.4%, (e) 7.8% and (f) 9.1% [4]

2.2.3. Passive Flow Control

A different way to reduce the wake of a bluff body is to trigger a transition from laminar to turbulent flow, such that the air can reattach to the boundary layer. In a way, this is similar to an increase in the Critical Reynolds number; however, without changing the velocity, as it is based on the drag crisis phenomena. This can be done by introducing passive flow control devices.

2.2.3.1. Effect of Vortex Generators

A method to control the separation of the airflow is by introducing vortex generators, [14]. Vortex generators (VG) are airfoil-type geometries that, under an angle, generate a rotation in the flow. The rotation leads to a re-energized boundary layer, which, in turn, delays separation. Thus, placing the VG in front of the separation region leads to a reduction in drag [14].

Based on this, an experimental study is performed to delay the separation of cylinders and the limbs of the running athletes [5]. The effect of introducing vortex generators on the leg of a runner on the drag area is visible at multiple velocities. According to the paper [5], a drag reduction of around 7.3% is noted when adding two strips of VGs to the thigh and calf of the leg. Next to this, it was seen that combining VGs of different heights and spacing tailored to the specific leg segments results in more drag reduction [5]. As the VGs are placed tangentially to the flow, crosswind can influence the effectiveness. Therefore, the VGs were tested under a yaw angle of $15°$ and compared to VGs at a yaw angle of $0°$ and to a yaw of $0°$ with no VGs present. From this experiment, it was clear that the yaw angle reduced the effectiveness; however, there is still a drag reduction seen.

2.2.3.2. Effect of Zigzag strip

Triggering transition can be done by adding a roughness strip of a zigzag tape to the surfaces. Based on an experimental study [20], the height of the strip or tape influences the transition as the height is related to the critical Reynolds number. According to the study, the roughness strip would has a critical roughness height Reynolds number of 600, while a zigzag tape of a height of $0.35\ mm$ has a Reynolds number of 200. This means that a zigzag tape requires a lower height to trigger a transition. For this reason, zigzag tapes are investigated on the surface of bluff bodies and athletes.

In an experimental study [28], the effect of zigzag tapes and their placement is tested on both a cylinder and on the leg of a speed-skater. The drag coefficient of the cylinder is measured over a range of Reynolds numbers. The effects of the placement, meaning the angle at which the zigzag tape is placed, and the thickness of the zigzag tape are shown in Figure 2.14. Increasing the angle at which the tape is placed leads to a decrease in the drag coefficient, until it converges. Meaning placing the zigzag tape just in front of the separation region leads to the biggest reduction in drag coefficient. On the other hand, the thickness of the tape shows a small influence on the effectiveness.

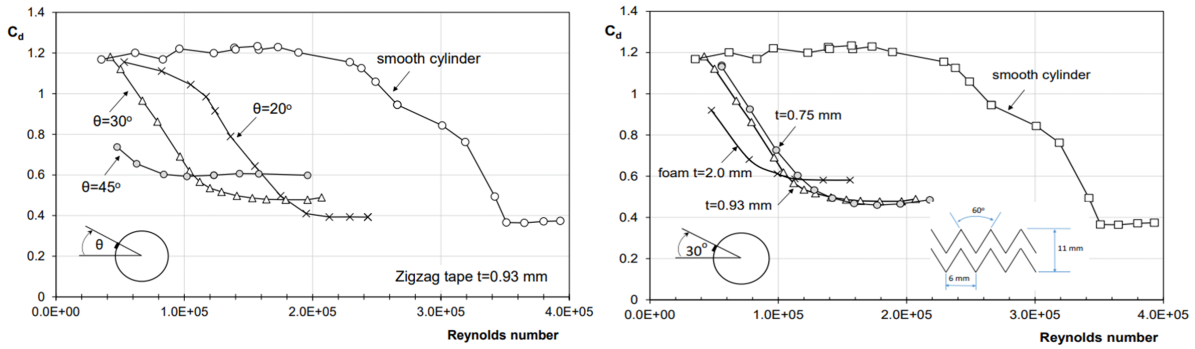

(a) Effect of placement of the tape

(b) Effect of the thickness of the tape

Figure 2.14: Effect of zigzag tape on the drag coefficient of a cylinder [28]

Based on this information, [28] placed the zigzag tape on the leg of the speed-skater. The region behind the tape is attached turbulent flow and thus delays separation, as seen in Figure 2.15. The effect on the drag coefficient of the tape is plotted in Figure 2.16 at different angles of attack. At all angles, the zigzag tape reduces the drag coefficient; however, a greater reduction is seen at negative angles, while at positive angles the reduction becomes smaller.

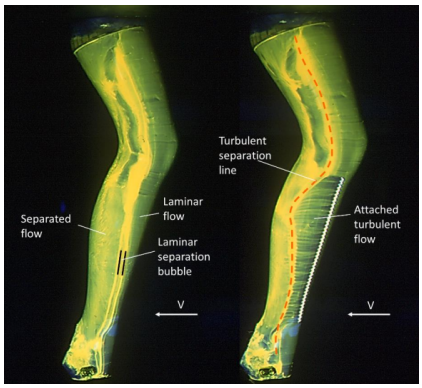

Figure 2.15: Flow visualisation of the separation delay using zigzag tape, [28]

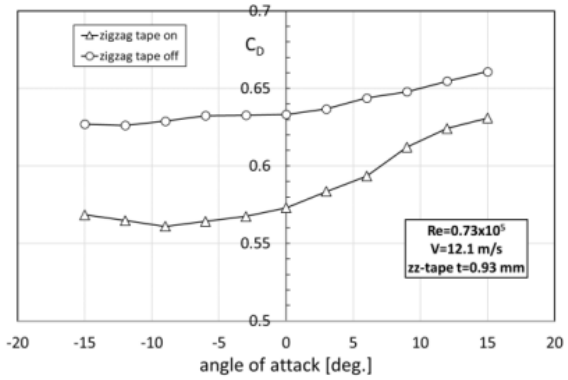

Figure 2.16: Drag reduction at different angles of attack due to zigzag tape, [28]

A different experimental study conducted by [26], proved that the application of zigzag tape can lead to a decrease in drag on the legs of cyclists.

2.3. Project Scope

The subject of this thesis will follow from the conclusion drawn from the literature study, the hypotheses made from them and finally the research questions to answer the hypotheses.

2.3.1. Conclusion from Literature Study

From the literature study, multiple conclusions can be drawn about the aerodynamic influence on the cyclists' performance. The main obstacle a rider must overcome is the aerodynamic drag [19]. Hence, reducing the drag is of the utmost importance. Reduction in drag can come from multiple different reasons and can be categorised into three main reasons: (1) the position of the cyclist, (2) the airflow conditions, and (3) passive flow control devices.

First, the time trial position results in the lowest drag configuration as the frontal area is reduced. Based on this, most experiments have been done with a cyclist in a time trial position. In this time trial position different crank angles were tested. The outcome showed that in a symmetrical leg position, the drag area, $C_D A$, is at its lowest as symmetrical quadruple vortices are generated behind the cyclist. The

most drag is developed in the asymmetrical leg position, as the vortices are asymmetric and last longer. Besides the leg position, the position of the arm affects the aerodynamics. A few computational studies revealed that positioning the hands together and raised in combination with keeping the elbows together reduced the drag area as the wake becomes more contained.

Secondly, the airflow conditions were investigated to understand the effect on the aerodynamics. Several studies on the Reynolds number variation demonstrate that increasing the velocity reduces the aerodynamic drag area and coefficient. The velocity increase leads to a delay in the flow separation, thus a less wide wake. On the road, the incoming air is often at an angle, crosswind. An experimental study reveals that the yaw angle can have a significant effect on the asymmetric time trial cyclist. A reduction in the drag area up to 35% is noted when the incoming air reaches the bent leg first. Consequently, the turbulence intensity of the airflow impacts the aerodynamic drag area of the cyclist. In wind tunnels, the intensity is lower than 2%, while in the outdoor environment, the intensity is higher. An experiment showed that an increase in turbulence intensity leads to a reduction in drag area. Similarly, higher intensities lead to bigger reductions in drag area when the velocity is increased.

Lastly, several studies were performed on the introduction of passive flow control devices. To trigger transition to allow turbulent flow to reattach itself to the surface, separation is delayed. Adding vortex generators or zigzag tape in front of the separated region leads to reattachment and thus a drag reduction.

2.3.2. Research Objective

Conclusions can be drawn from the experiments that have been performed. However, the male mannequin differs in each study, which introduces multiple issues. First, the outcomes of one study can be fully influenced by the cyclist geometry and lead to different outcomes when a different geometry is used. Secondly, as the dimensions of the cyclists are not shared, continuation of the experiments is not possible. Therefore, a Generic Cyclist Model (GCM) is generated [25], which eliminates the issues. The GCM geometry is shared such that multiple follow-up wind tunnel experiments can be performed, and the cyclist aerodynamics can be shared.
Currently, the GCM has only been tested in an asymmetric time trial and sprint position, as this is the highest drag leg configuration. On the GCM, a couple of experiments have been performed about the influences of the Reynolds Number and of the crosswind. Investigations of the GCM in the symmetric position of the legs have not been carried out. Therefore, in this thesis, the Symmetric Generic Cyclist Model will be researched in the wind tunnel, and the effect of multiple parameters on the aerodynamics will be analysed.

2.3.3. Research Question

This thesis will answer the research question "*What is the aerodynamic sensitivity of the Symmetric Generic Cyclist Model and how does it differ from the Asymmetric Generic Cyclist Model?*". To investigate the sensitivity of the GCM, the question is split up into four categories, each having multiple specific sub-questions.

Influence of the symmetric leg position

- What is the effect of the change in leg position on the drag area of the Generic Cyclist Model?
- How does the symmetric leg position alter the aerodynamic flow field of the Generic Cyclist Model?

Influence of Reynolds number on the Symmetric Generic Cyclist Model

- What is the effect of the Reynolds number variation on the drag area of the Symmetric Generic Cyclist Model?
- How does the Reynolds number effect of the Symmetric Generic Cyclist Model compare to the Asymmetric Generic Cyclist Model?
- What is the effect of the variation in Reynolds number on the aerodynamic flow field of the Symmetric Generic Cyclist Model?
- How does the behaviour caused by the variation in Reynolds number of the aerodynamic flow field compare to the Asymmetric Generic Cyclist Model?

Influence of Crosswind on the Symmetric Generic Cyclist Model

- What is the effect of crosswind on the drag area of the Symmetric Generic Cyclist Model?
- Does the crosswind effect on the Symmetric Generic Cyclist Model have a symmetrical behaviour?
- How does the crosswind effect compare to the Asymmetric Generic Cyclist Model?
- What is the effect of the crosswind on the aerodynamic flow field of the Symmetric Generic Cyclist Model?
- Does the wake of the Symmetric Generic Cyclist Model have a symmetrical shape?
- How does the behaviour caused by the crosswind affect the aerodynamic flow field compared to the Asymmetric Generic Cyclist Model?

Influence of passive flow control devices on the Symmetric Generic Model

- What is the effect of introducing passive flow control devices on the hips of the Symmetric Generic Cyclist Model?
- What is the effect of introducing passive flow control devices on the extremity of the Symmetric Generic Cyclist Model?
- How does the effectiveness of the flow control devices on the Symmetric Generic Cyclist Model change due to the Reynolds number variation and crosswind?
- What is the effect of the flow control devices on the Symmetric Generic Cyclist Model on the aerodynamic flow field?
- How does the aerodynamic flow field of the flow control devices change under the Reynolds number variation and crosswind?

3 Methodology

To be able to investigate the aerodynamic sensitivity of the Symmetric GCM, the model needs to be adjusted, and the experiment must be set up. The methods and procedures required for the experiment are discussed in this chapter.

3.1. Generic Cyclist Model

The experiment is a continuation of previously conducted tests on the Generic Cyclist Model (GCM). The GCM is an average of fourteen male elite cyclists and was designed by Terra [25]. Each of the cyclists is specialised in one of the categories: climbers, classics, sprinters, time-trialists, punchers and general classifications, which leads to a wide range of body dimensions. Each rider was scanned from the left and right side in an asymmetric time trial and sprint position while wearing their regular cycling clothes. After the scans were completed, artefacts such as the bike and floor were removed, and the left and right sides were combined. This results in fourteen individual scans [25]. Landmarks on the scans are used to connect the cyclist to the base model, and all the scans are placed over the base model. A weighted average is used to generate the generic model, as the cyclists all have different dimensions that can be linked to their weight. Afterwards, the generic model is post-processed to enhance the quality [25]. Finally, the computer-aided design (CAD) is designed and shown in Figure 3.1. The cyclists were scanned in the asymmetric leg position, and thus some modifications to the model have to be applied to get a symmetric position. The dimensions of the asymmetric model can be found in [25]. To obtain the symmetric leg position, the crank angle was rotated by $60°$, resulting in the left foot in front of the right foot. The CAD of the Symmetric GCM can be seen in Figure 3.2. The model is positioned in the time trial position, meaning the hands and elbows are placed together and are in a raised position.

The calculations required for the aerodynamic parameters, certain values related to the GCM, must be measured. The frontal area of the Asymmetric GCM, including the bike, is calculated to be $0.35 \pm 0.01\ m^2$ and is obtained from the digital scans, [25]. To obtain the frontal area of the Symmetric GCM, the frontal areas of both models in CAD were calculated and compared to each other. This showed a less than 1% difference, hence the Symmetric GCM has the same frontal area as the Asymmetric GCM, $0.35 \pm 0.01\ m^2$. Furthermore, the hip width of the GCM is required and measured to be $0.335\ m$ for the Asymmetric GCM [25]. Similarly, the difference between the hip width of the Asymmetric and Symmetric GCM is negligible, and thus assumed to be the same.

Figure 3.1: CAD of the Asymmetric GCM

Figure 3.2: CAD of the Symmetric GCM

Through additive manufacturing, a full-scale symmetric GCM is produced and polished to create a smooth surface with roughness of $k < 0.1\ mm$ [25]. The model is produced in different parts; the arms and legs can be detached to simplify the setup as well as allow for clothing options. In this experiment, the model is not wearing any clothing options, as this would lead to surface roughness influences on the aerodynamics and might alter the results of the passive flow control devices. For this reason, the detachment lines are covered by insulation tape to reduce their aerodynamic influences [25]. The GCM is placed on a Scott Plasma 5 frame bike with rim brakes and has a Shimano DuraAce wheelset. Furthermore, the model is equipped with a Kask Mistral helmet and shoes of Shimano SPhyre RC902 [25]. In Figure 3.3 and Figure 3.4, the symmetric GCM on the bike is shown in CAD and during the experiment.

Figure 3.3: CAD of the Symmetric GCm on the bike

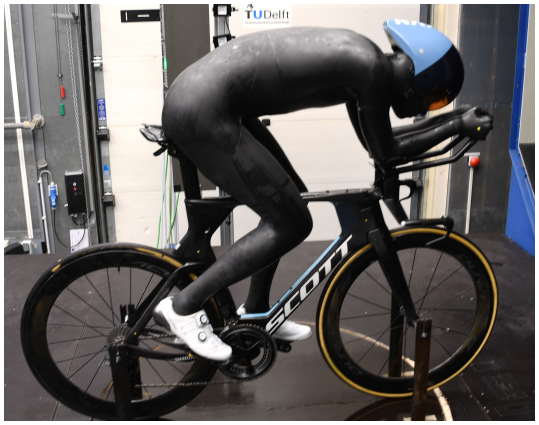

Figure 3.4: Printed symmetric GCM placed on the bike

3.2. Passive Flow Control Devices

As chapter 2 has indicated, the drag of the cyclist must be reduced to allow for faster times. A way to reduce the drag is by adding passive flow control devices to the cyclist, as has been mentioned in subsection 2.2.3. There are three positions where the flow control devices can be placed to influence the aerodynamics, the hips, the arms and the legs of the Symmetric GCM.

3.2.1. Devices on the Hip

The airflow conditions in front of the hip separation are not known, as no prior investigations have been performed. As the airflow is affected by multiple different parts, it cannot be assumed that it is laminar, but rather in transition or turbulent. As a result, only flow control devices that work in turbulent conditions are considered for the hips: vortex generators.

Vortex generators (VGs) are devices that work in laminar, transition and turbulent conditions [14]. VGs generate rotations in the airflow due to the pressure difference caused by the VG. The rotation leads to 'cleaner' air being moved onto the surface of the model, meaning they re-energise the boundary layer. Based on an experimental study of low-profile vortex generators in turbulent air, [14], the effects of different VGs are investigated. A summary of the effectiveness in the reduction of separation is plotted in Figure 3.5a. As can be seen, the four most effective VGs can be categorised as vane-type and Wheelers VGs. The geometry of these different VGs is drawn out in Figure 3.5b. The vortex generations are tested on a backwards-facing ramp at relatively low speeds ($40\ m/s$). During the test, the vortex generator devices (of the same style) are placed next to each other as the distance in between also affects the separation.

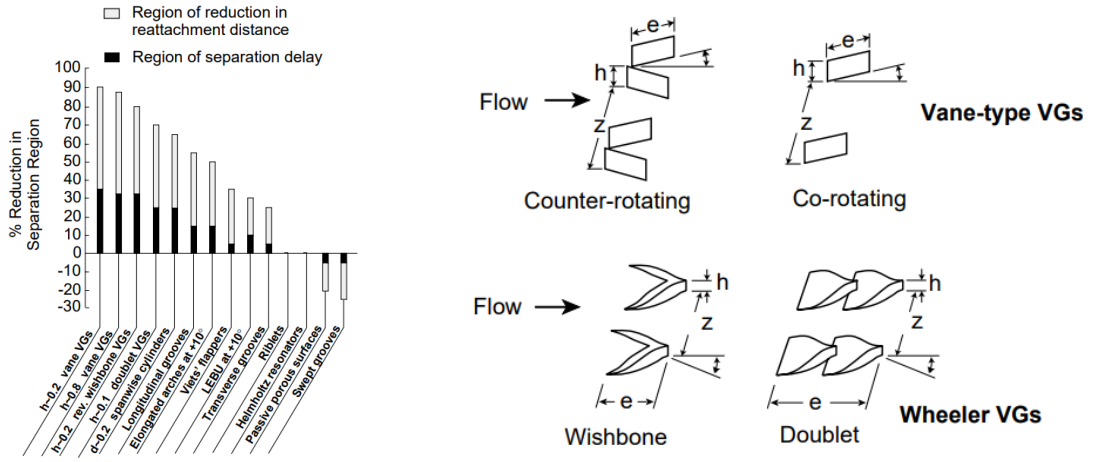

(a) Summary of effectiveness in separation reduction

(b) Geometry of different VG types

Figure 3.5: The effectiveness and geometry of different vortex generators [14]

The effectiveness of the vortex generator in reducing separation depends on the dimensions of the VG itself. The dimensions are related to the boundary layer (BL) thickness, δ. They are low-profile vortex generators, meaning the height is smaller than the BL thickness. The other dimensions are based on the height of the device; these parameters are the chord length, the spacing between the devices, the incidence angle and the distance from the separation line. In Table 3.1, the dimensions of the four most effective devices are given.

Table 3.1: Relation between vortex generator dimensions and boundary layer thickness [14]

		Height h	Chord length e	Distance Δz	Incidence angle β	Distance from separation ΔX_{VG}
Vane - type	Co-rotating & Counter-rotating	0.2·δ 0.8·δ	$4 \cdot h$	$9 \cdot h$*	±25	$10 \cdot h$
Wheeler - type	Revered wishbone	0.2·δ	$3 \cdot h$	$4 \cdot h$	±23	$10 \cdot h$
	Doublet	0.1·δ	$13 \cdot h$	$8 \cdot h$	±25	$20 \cdot h$

* For counter-rotating vanes: the spacing between the two vanes is $s = 1 \cdot h$

Since vortex generator devices have never been tested on the hips of cyclists, it is unclear which type and dimension would work best. The most common vortex generators are counter-rotating vanes; hence, they will be used during the test. Furthermore, a range of dimensions will be tested to understand the effect of the VG on the separation.

For the dimensions of the VG, the boundary layer thickness of the hip must be calculated; however, this has never been done before. This is why an assumption based on scaling is made to estimate the BL thickness of the hip. In a paper, [9], about the reduction of the drag of a cylinder, a relation between the diameter of the cylinder and the boundary layer thickness is found. It is stated, that, based on experimental data, a cylinder with a diameter of $9\ cm$ has a BL thickness of around $1\ mm$. Therefore, the scaling would be $\delta\ [mm] = 1\ [mm] \cdot \frac{d_{GCM}\ [cm]}{9\ [cm]}$.

The diameter of the hip of the GCM is approximately $23\ cm$. Using the scaling above, the boundary layer thickness would be approximately $2.5\ mm$. The range of dimensions is related to the boundary layer thickness; three different heights will be tested. A low-profile VG, meaning a thickness smaller than the boundary layer, a height similar to the BL thickness and a height larger than the estimated BL thickness, which are 0.5δ, 1.0δ and 1.5δ, respectively.
The dimensions of the three devices are given in Table 3.2 and are based on the relation with the BL thickness mentioned in Figure 3.5. The VGs will be placed on a strip of approximately $25\ cm$ long, so that it will cover the entire hip area.

Table 3.2: Dimensions of the vortex generator devices

VG type	Height $h\ [mm]$	Chord $e\ [mm]$	Distance $\Delta z\ [mm]$	Spacing $s\ [mm]$	Incidence angle $\beta\ [°]$	Distance from separation $\Delta X_{VG}\ [mm]$
Counter-rotating h-0.5δ	1.25	5	11.25	1.25	25	12.5
Counter-rotation h-1.0δ	2.5	10	22.5	2.5	25	25
Counter-rotation h-1.5δ	3.75	15	33.75	3.75	25	37.5

The distance between the leading edge of the vortex generators and the separation line is of influence. Based on the table above, the preferred distance per VG is mentioned. To give an indication as to where the VG strips will be placed and how long the strips must be, the shear stress on the model is investigated using CFD. In Figure 3.6, the shear stress on the right and left sides of the symmetric GCM are shown. The shear stress is indicated using the colour scheme. Red indicates high shear stress, while blue indicates low (or zero) shear stress. The dark blue line on the upper legs shows the separation line. Besides the shear stress, the airflow streamlines are visualised. At the dark blue line, the streamlines are not connected; this is another indication of the separation line.

The CFDs give an indication of the separation line location, based on this, it is estimated that a VG strip of $25\ cm$ long will be sufficient. The exact location of the VG strips on the GCM will be measured after the separation line on the model has been visualised by using oil flow visualisation.

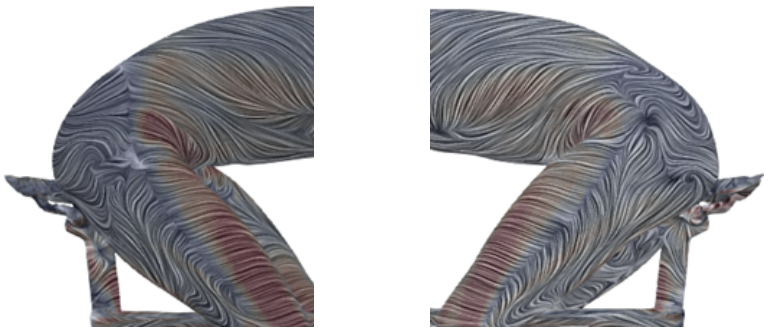

(a) Right side **(b)** Left side

Figure 3.6: Skin friction on the symmetric GCM in CFD

The three different types of vortex generator strips are 3D printed for accuracy and to keep them flexible. This flexibility is needed to be able to place them on the hips of the GCM. The three different dimensions of VGs are shown in Figure 3.7

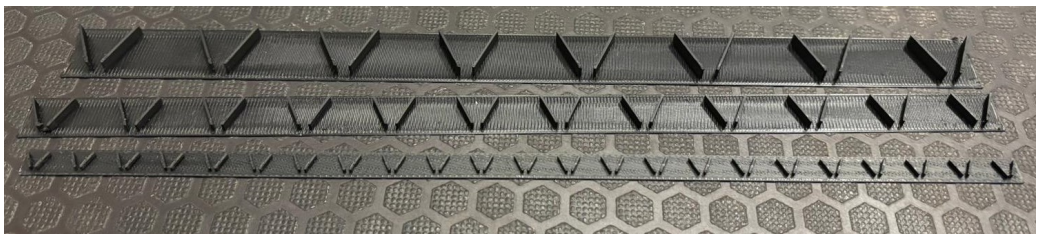

Figure 3.7: Printed vortex generator strips

3.2.2. Devices on the Arms and Legs

The airflow around the upper part of the arms is considered to be laminar as the incoming air is not disturbed. Due to this, the arms can be considered bluff bodies, similar to a circular object. One of the more conventional devices for circular bluff bodies are zigzag strips, as they can trigger transition in the airflow. Based on prior experiments with zigzag strips on bluff bodies and athletes, mentioned in subsubsection 2.2.3.2, the dimensions and location of the strip are selected.

The zigzag strip is taped to the outside of the upper arms of the GCM, at an angle of approximately $45°$ from the front, see Figure 3.9a. The length of the strip is based on the distance between the inner elbow and the armpit. The dimensions of the zigzag strip are mentioned in Table 3.3.

An alternative method is to place flow control devices on the legs of the Symmetric GCM. The legs are divided into two parts, the lower and upper parts of the leg.
The lower legs are assumed to be in laminar airflow, meaning zigzag strips can be used. The airflow reaching the upper legs has not been investigated in prior experiments. For this reason, and simplicity, it is assumed to be either laminar or in transition. Thus, the exact same zigzag strip as the lower legs will be used for the upper part. The dimensions can be found in Table 3.4, as can be seen, the thickness is less than of the zigzag strips placed on the arms. This choice was based on the availability of the zigzag strips within the experiment.

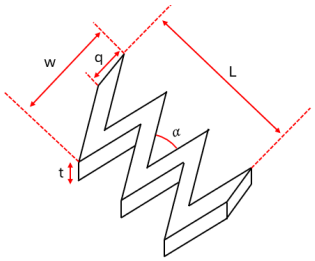

Figure 3.8: Schematic drawing of the zigzag strip dimensions and location

Table 3.3: Dimensions of the zigzag strip on the GCM's arms

Parameters		Value
Thickness	t	$0.79\ mm$
Strip width	w	$12\ mm$
Zigzag width	q	$6\ mm$
Angle	α	$60°$
Length	L	$20\ cm$

Table 3.4: Dimensions of the zigzag strip on the GCM's legs

Parameters		Value
Thickness	t	$0.65\ mm$
Strip width	w	$12\ mm$
Zigzag width	q	$6\ mm$
Angle	α	$60°$
Length	L	$38\ cm$

(a) The zigzag strip on the arms

(b) The zigzag strip on the upper leg

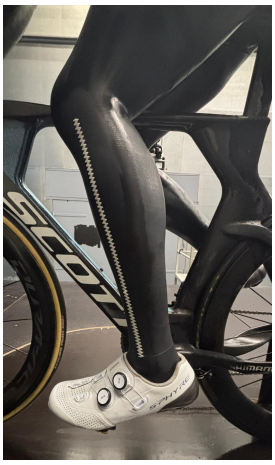

(c) The zigzag strip on the lower leg

Figure 3.9: Zigzag strip placed on the arms and legs of the Symmetric GCM

3.3. Data Acquisition

The aerodynamic sensitivity can be understood by measuring aerodynamic loads as well as capturing the flow field around the cyclist and on the cyclist's surface. The data is collected via three methods: the loads are measured via a balance measurement, the flow field behind the cyclist is captured with particle image velocimetry and the surface boundary layer is visualised by flow visualisation techniques.

3.3.1. Atmospheric Measurements

During the experiment, the atmospheric data, such as air velocity, pressure, temperature and dynamic pressure, are recorded. The data is used to calculate the Reynolds number for each GCM configuration. The Reynolds number depends on the density, velocity and dynamic viscosity of the airflow as well as the characteristic length of the model, see Equation 3.1. The characteristic length, c, of the symmetric GCM is set to be the hip length, $0.335\ m$.

$$R_e = \frac{\rho U c}{\mu} \tag{3.1}$$

The density of the airflow can be calculated using the ideal gas law, Equation 3.2[1]. For this, the measured atmospheric pressure, the ambient temperature (in Kelvin) and the air gas constant, $R = 287.058\ J/kgK$ are needed. Lastly, the dynamic pressure is calculated using Sutherland's empirical relationship, Equation 3.3 [23]. The equation needs the measured ambient temperature in the wind tunnel and the reference temperature, dynamic viscosity and Sutherland's temperature, which are $273.15\ K$, $1.716 \cdot 10^{-5}\ kg/ms$ and $110.4\ K$, respectively [23].

$$\rho = \frac{p}{RT} \tag{3.2}$$

$$\mu = \mu_{ref} \left(\frac{T}{T_{ref}} \right)^{3/2} \frac{T_{ref} + S}{T + S} \tag{3.3}$$

3.3.2. Force Balance Measurements

The aerodynamic loads experienced by the cyclist during the experiment are measured using a balance. The balance measures the loads of the cyclist in three directions, x, y, and z, drag force, side force and lift force, respectively, as well as the moment arms around each axis. The data is measured for 30 seconds at a frequency of $2\ kHz$, after which the data is averaged.

The loads measured are in the direction of the cyclist, see Figure 3.10, thus the cyclist's aerodynamic loads are measured. Meaning that if the cyclist is placed under an angle to the incoming airflow, the drag force with respect to the airflow is under the same angle. Hence, no crosswind corrections have to be applied.
The drag force will be used to calculate the aerodynamic performance, the drag area, $C_D A$, of the cyclist, using Equation 3.4, [25]. For this equation, the atmospheric measurements, density, ρ and freestream velocity, U_∞ are required. The drag area is related to the velocity, hence the Reynolds number has an influence.

$$C_D A = \frac{F_D}{\frac{1}{2}\rho U_\infty^2} \tag{3.4}$$

The force balance has a maximum streamwise error in the measurement of around $0.15\ N$ [25]. This error leads to slightly difference result when the tests are repeated. The effect on the aerodynamic loads is further discussed in section 3.8.

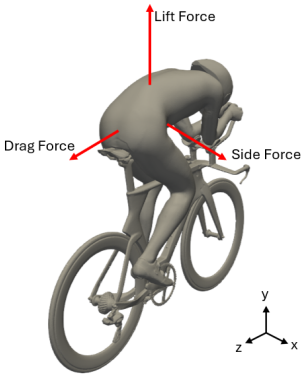

Figure 3.10: The direction of the aerodynamic load measurements

3.3.3. Particle Image Velocimetry

Subsequently, with the load measurements, the flow field will be analysed. The flow field behind the saddle is investigated to understand the wake of the cyclist under different conditions. The flow field is visualised using particle image velocimetry (PIV). Specifically, Lagrangian particle tracking (LPT) or 3D particle tracking velocimetry (3D PTV), [22]. A 3D volume is captured and measured rather than obtaining a 2D plane with conventional PIV. This allows for the flow field to be analysed at different positions relative to the cyclist, for instance, behind the saddle or behind the rear wheel. This enables a better understanding of which parts of the GCM produce which characteristics in the flow field.
PIV or LPT is based on the tracking of the airflow. This is done by injecting tracer particles, which are Helium Filled Soap Bubbles (HFSB), into the airstream by a seeding mechanism [16]. These HFSB are illuminated by LED flashlights and captured by multiple cameras over a period of time. The cameras photograph the volume every couple of milliseconds. These images require post-processing to extract the flow field.

With the use of the DaVis software, the images taken by the LPT can be processed. In the case of LPT, the individual tracer particles are followed through the images in the 3D volume. This differs from conventional PIV as cross-correlation on the particles would be used to extract the flow field [22].
The individual tracer particles in the volume are identified by using triangulation. Using the images of

[1] Ideal Gas Law - Khan Academy

the multiple cameras, the particles are matched to each, meaning that a particle in one image must be matched to itself in a different image from another camera.
For example, two images are taken at the same time by two cameras of the same flow field. Since the cameras are at different locations, the particles are at different positions relative to the cameras. The matching, done by triangulation, finds the particles in one images and finds them in the second image.

After the particles have been matched, the software will predict their trajectories in space and time. The amount of tracer particles in the airflow does lead to limitations; in cases with a high ratio of particles to air, the software cannot predict all the trajectories. This leads to ghost particles, which are residual particles that cause inaccuracies in the velocity field. To increase the accuracy and thus reduce the ghost particle, the Shake-The-Box method (STB) is applied [22]. The particles in the image are moving slightly (within two pixels), shaken, until the software can predict a trajectory.

After the tracer particles have been identified and their tracks have been found, the flow field can be extracted. The flow field is based on the velocity vectors of each of the tracked particles. The velocity is measured in three directions, lateral, vertical and streamwise, see Figure 3.11a. As the LPT measures in a volume, from this, the flow field at multiple planes (different z-locations) can be obtained. See Figure 3.11b, where the measurement volume is shown in yellow and the different planes in black.

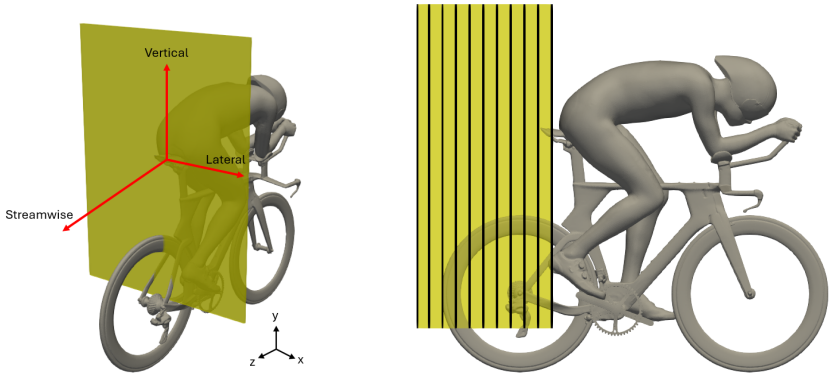

(a) Directions **(b)** Z-planes

Figure 3.11: The direction of the PIV measurements and the location of the z-planes

3.3.4. Surface Flow Visualisation

The airflow is predicted to separate from the model around the back/hip area. The model's boundary layer and thus airflow separation can be visualised using the high viscosity flow visualisation technique, [21]. A fluid with high viscosity (higher than that of air) is moved by the frictional force exerted by the surrounding air. Using this principle, the fluid is placed on the surface of the model and then placed in the airflow. The fluid is influenced by the pressure gradient of the airflow and the shear stress on the model. When air flows over the model, the fluid moves along which visualised the surface streamlines. In the case of separation, the shear stress vanishes; hence, the high viscosity fluid will not move. On the model, a brighter region can be spotted, as this is where the fluid has accumulated. Similarly, the reattachment line can be spotted, as this area is dark since the fluid has been swept away, [21].

3.4. Experiment Setup

The experiments are performed in the Open Jet Facility (OJF) wind tunnel of the Delft University of Technology at the faculty of Aerospace Engineering, [24]. The wind tunnel is a closed-return OJF; a schematic drawing of the facility can be seen in Figure 3.12. The OJF is able to reach a maximum velocity of $35\ m/s$ in the test section due to the fan, which is driven by a $500\ kW$ engine. The test section has an orthogonal cross-section of $2.85\ m \times 2.85\ m$. The turbulence intensity of the freestream airflow in front of the nozzle is measured to be 0.5% [13], however, due to the PIV system, a seeder is placed inside the wind tunnel, increasing the turbulence intensity to around 0.8% [27]. The effect of the turbulence intensity increase on the aerodynamics will not be included in the results.

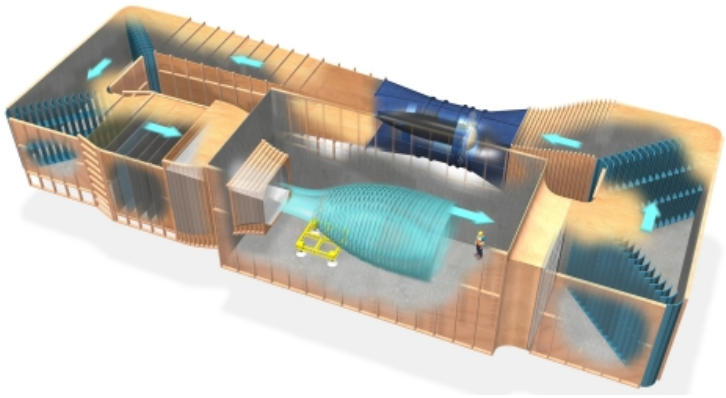

Figure 3.12: Schematic images of the Open Jet Facility at TU Delft, [24]

A similar setup as previous experiments, [16] [25], is used, such that the data can be compared to the prior results without introducing unknowns or errors caused by different setups.

The GCM is mounted on a fake floor in front of the wind-tunnel nozzle, where the fake floor is aligned with the nozzle's exit, as can be seen in Figure 3.13a, which is approximately $1.5\ m$ above the ground. The floor of the dimensions $4\ m \times 3\ m$ has a detached circular floor of $1.2\ m$ diameter in the middle, underneath the GCM. The circular floor is attached to the force balance, which is used to calculate the aerodynamic loads, and to four vertical struts. These struts are connected to the GCM's bike, with two struts holding the front wheel and two the rear. The GCM, struts, circular floor and force balance are connected to each other, and are able to rotate to simulate crosswind.
Besides the GCM setup, the attributes needed for the PIV setup are visualised in Figure 3.13a. This setup consists of 3 LED's to illuminate the helium-filled soap bubbles, which are placed on the left side of the GCM. The volume the LED's illuminate leads to the volume in which particles can be tracked using Shake-The-Box, see Figure 3.13b. The LED's are LED-Flashlight 300 from LaVision[2] and have a cross-section of $0.3\ m \times 0.1\ m$, which contain 72 smaller LED lights. In front of the LED's, a black plate is placed to limited the area that is illuminated. This plate blocks the light that is pointed towards the GCM, as only the flow field behind the cyclist is investigated.
The cameras needed to photograph the illuminated particles are positioned in the left corner and about $4\ m$ behind the GCM. The four Photron FastCam Mini AX100[3] cameras are placed on top of each other, ranging from $1.5\ m$ to $3\ m$ above the ground. The positions are based on the field of view of each camera and the combined view, as they must cover the area around the cyclist. The cameras are equipped with Samyang lenses with a focal length of $50\ mm$. For the PIV measurements, the camera lenses have an f-stop of 5.6.

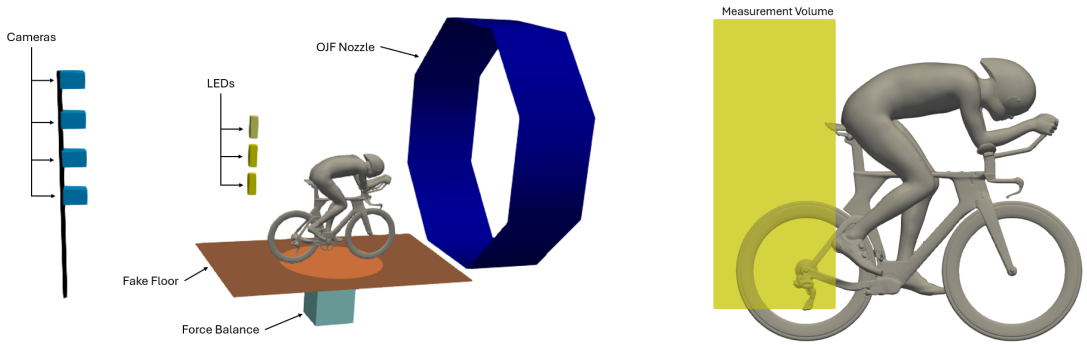

(a) Schematic drawing of the experiment setup

(b) Schematic drawing of the PIV volume

Figure 3.13: Drawing of the experiment setup and PIV measurement volume

[2] LaVision - LED-Flashlight 300
[3] Photron - FASTCAM MINI AX

Besides, the above-mentioned parts of the experiment setup, two parts have not been mentioned. The seeder mechanism that injects the helium-filled soap bubbles into the airflow, and the setup of the oil flow visualisation. The seeder itself is located in the settling chamber of the OJF, a couple meters upstream of the nozzle. The seeder has a cross-section of $1\ m \times 2\ m$ and is positioned on the ground. The oil flow visualisation setup consists of 6 UV lights and a Nikon camera. The UV lights are attached to a beam and placed on top of each other, with the camera placed above the lights. The beam is located on the right side of the GCM about $2\ m$ away from the right hip.
The complete experimental setup is shown in Figure 3.14, including detailed images of the required equipment, such as PIV cameras, the LEDs, Flow vis cameras, UV lights and the seeder.

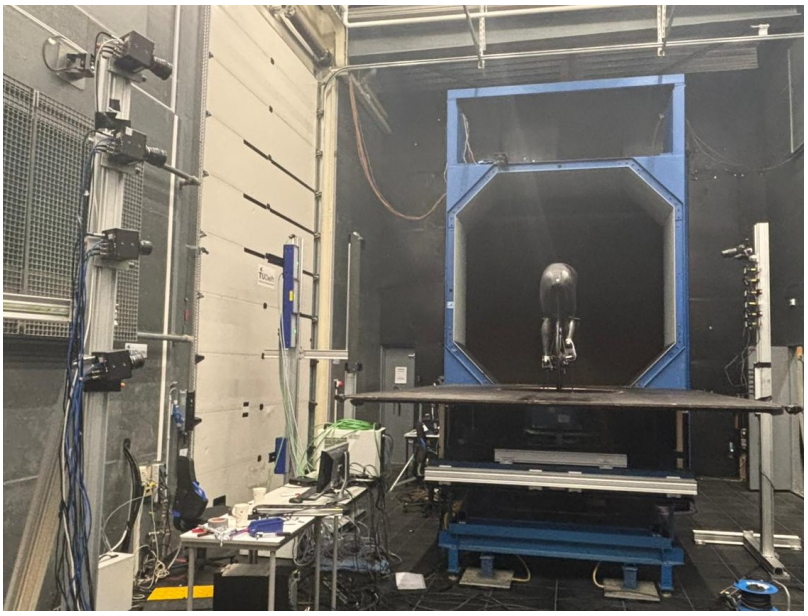

(a) The experiment setup in the OJF

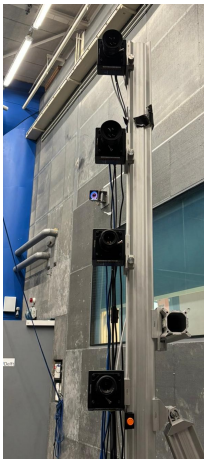

(b) PIV cameras

(c) LED's

(d) Flow Vis camera and lights

(e) Seeder

Figure 3.14: The setup of the experiment with detailed images of the different parts

3.5. Test Plan

To answer all the research questions in subsection 2.3.3, the experiment is split into the three categories: Reynolds number effects, crosswind effects and effects of flow control devices. For the experiment, a test plan is written based on the categories. In addition to the symmetric GCM experiment, the asymmetric GCM will be retested, as not all data have been obtained during prior experiments.
The first two categories are based on the airflow conditions in the wind tunnel. The force balance and PIV measurements are obtained at different airflow configurations, meaning combinations of velocity

and crosswind angles. The force balance will be measured at all configurations, while the PIV will only be obtained at certain configurations. Table 3.5 shows the values of the airflow conditions which will be tested.

The Reynolds number effect is tested by varying the velocity. The full range of velocity starts at low velocity, $5\ m/s$, and is increased in steps of 5 to $25\ m/s$, thus testing at $10\ m/s$, $15\ m/s$ and $20\ m/s$. Furthermore, the experiment will be conducted at $14\ m/s$, as this is the most representative velocity during the time trial [25]. Moreover, velocities surrounding the representative velocity are added ($12\ m/s$ and $18\ m/s$) to get more detailed results.
The PIV will be performed at the representative velocity, $14\ m/s$, as well as the velocities $10\ m/s$ and $18\ m/s$. This is done to visualise the wake of the GCM due to the difference in Reynolds number.

The effect the crosswind has on the aerodynamic performance will be quantified by measuring the forces and obtaining PIV measurements at different yaw angles. A large range of yaw angles is tested from $-10°$ to $10°$ with steps of $2°$, in addition, the angles $15°$ and $20°$, both positive and negative, will be tested to generate a larger dataset and understand the effects large crosswinds have on the cyclist. The force balance will obtain the loads at all yaw angles, while the PIV will only obtain the wake at $0°$, $4°$, $-4°$, $6°$, $-6°$, $8°$ and $-8°$ (which will be further mentioned as $0°$, $\pm4°$, $\pm6°$, $\pm8°$).

Table 3.5: Velocity and crosswind conditions measured during the experiment for the force balance and PIV

	Velocity $[m/s]$	Crosswind angle $[°]$
Force balance	5, 10, 12, 14, 15, 18, 20, 25	$0,\ \pm2,\ \pm4,\ \pm6,\ \pm8,\ \pm10,\ \pm15, \pm20$
PIV measurements	10, 14, 18	$0,\ \pm8$*

* For the Symmetric GCM, at $14\ m/s$ PIV will also be conducted at the crosswind angle $\pm4°$ and $\pm6°$

Before the flow control devices are tested, oil flow visualisation is applied to the hip area of the GCM to show the separation line. The six flow control devices will be tested at all velocities; however, only at the yaw angles: $0°$ and $\pm8°$ to reduce the test plan. Based on the results of the three vortex generators and three zigzag strips, the devices that reduce the drag area have PIV measurements. The PIV will be obtained at $14\ m/s$ and $18\ m/s$ at the crosswind angles $0°$ and $\pm8°$.

The detailed test plan of the entire experiment is given in Appendix A.

3.6. Data Post-Processing

The data acquired must be processed before any conclusions can be made. The balance force data requires corrections to eliminate non-aerodynamic loads. From the PIV images, techniques and filters are applied to extract the flow fields.

3.6.1. Force Balance Measurements

The balance underneath the cyclist measures the loads and moments in three directions, the drag, side and lift forces and their moments. The balance measures all the loads and sums them together, thus it does not differentiate between what forces are caused by the weight of the model, the weight of the balance itself and the aerodynamic loads. Hence, corrections must be made on the balance measurements to retrieve only the forces caused by the aerodynamics of the cyclist. To remove the forces caused by the weight of the model, the loads are measured when the airflow in the wind tunnel is turned off, meaning when the velocity is $0\ m/s$. The wind off (WOF) force data is subtracted from the total forces measured by the balance during wind on (WON) measurements. Equation 3.5 shows the calculation to retrieve the WON drag force.

$$F_{D_{WON}} = F_{D_{total}} - F_{D_{WOF}} \tag{3.5}$$

After this correction has been done, the forces caused by the model supports must be removed. This is done by disassembling the model from the balance and measuring the forces at the different velocities. The forces measured during the disassembled tests are subtracted from the WON data, leading to the corrected drag force, Equation 3.6.

$$F_{D_{corrected}} = F_{D_{WON}} - F_{D_{disassembled}} \tag{3.6}$$

Besides the corrections needed for the balance forces, corrections can be done for the walls of the wind tunnel, called blockage correction. The correction for the Generic Cyclist Model in an open-jet wind tunnel is approximately 4%. As this correction is relatively low it is omitted from the calculations, [25] [3]. Furthermore, the correction has not been performed during the previous experiments.

3.6.2. Particle Image Velocimetry Measurements

For the PIV measurements, four cameras each take multiple images during the test. The number of images taken differs per velocity, as higher velocities require more images to achieve higher accuracy. During testing, it was found that an image rate of $750\ Hz$ for a velocity of $14m/s$ gave good results, and thus is set as the baseline. The image rate of the other velocities is based on the calculation: image rate $= 750\ [Hz] \cdot \frac{\text{velocity } [m/s]}{14\ [m/s]}$. The image rate determines the duration of a single image; multiply it by the number of images result in the full duration of the measurement.
Table 3.6 and Table 3.7 shows the number of images taken, as well as the image rate and the duration of the measurements per velocity for the Asymmetric and Symmetric GCM.

Table 3.6: PIV camera data for the Asymmetric GCM

Velocity $[m/s]$	Images $[-]$	Image rate $[Hz]$	Duration $[s]$
10	5000	530	9.4
14	5000	750	6.7
18	7000	960	7.3

Table 3.7: PIV camera data for the Symmetric GCM

Velocity $[m/s]$	Images $[-]$	Image rate $[Hz]$	Duration $[s]$
10	6000	530	11.3
14	6000	750	8.0
18	7000	960	7.3

Figure 3.15a shows an image taken by one of the PIV cameras. These images, or raw images, must be pre- and post-processed to extract the flow field. The raw image shows the GCM as well as the wind tunnel itself in the background. Next to this, the hips and the wheel of the GCM are brighter than the particles themselves. This must all be corrected as it interferes with the post-processing of the data and results in errors in the flow field.

The pre-processing part consists of the removal of the background by applying an image preprocessing filter. This filter removes the minimum intensity of the first 5 images from the remaining images and removes 5 pixels in space. This leads to the raw images being darkened, and only the HFSB are illuminated, see Figure 3.15b.

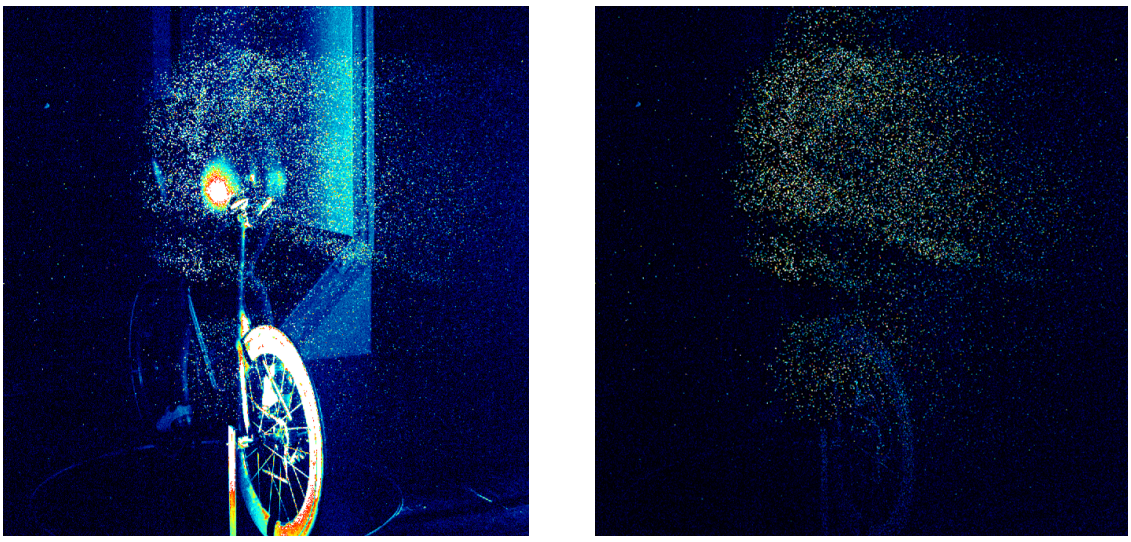

(a) Raw image **(b)** Pre-processed

Figure 3.15: Pre-processing of the PIV images takes from DaVis

After all images have been pre-processed, the Shake-The-Box (STB) algorithm is applied. The STB has multiple parameters, of which its values can be changed, leading to different results. Hence, all parameters must be tested to achieve higher accuracy and flow field quality. The accuracy is determined by the ratio between active tracks and total particles in the STB.
Most of the parameters are kept the same as the values from the prior experiment, [16]. One of the most important parameters is the threshold for particle detection, meaning which particles will be tracked. In the pre-processing image, the wheel of the cyclist is still visible and being tracked as particles. By increasing the threshold to 80 counts, the wheel is not taken into account during the STB, while the HFSB are still detected.
All the optimal parameters of the STB filter are written down in Table 3.8. Which leads to a ratio between active tracks and all 3D particles of 51% and is deemed accurate enough. The ratio of each image is plotted in Figure 3.16 for the Symmetric GCM at $14\ m/s$ at $0°$. Based on the data, the total amount of particles is around 23,000, with approximately 12,000 particles being tracked.

Table 3.8: Values for the Shake-The-Box post-processing

Parameter	Value	
Number of passes	1	
Allowed triangulation error	1	Voxel
Refine particle position and intensity	4	iteration
Remove particle closer than	1	Voxel
Make OTF smaller	1	times
Threshold for 2D particle detection	80	counts
Adding particles	4	iterations
Shake particle position	0.1	Voxel
Remove the particle with intensity weaker than	0.1	of the average intensity

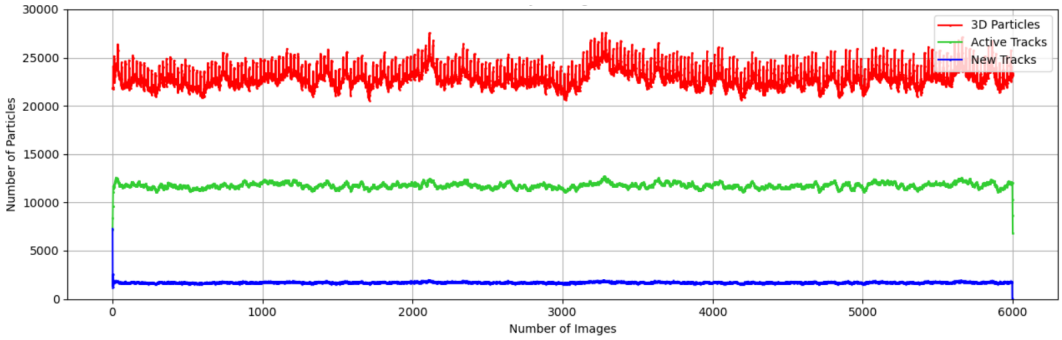

Figure 3.16: Accuracy of the Shake-The-Box filter in the post-processing of the Symmetric GCM at $14\ m/s$ at crosswind $0°$

Afterwards, a range filter is applied to remove inaccurate tracks. These tracks show different behaviour than others and have a much larger velocities. The range filter applies a limit on the velocities and removes the particles that exceed the limit. Table 3.9 gives the velocity range of the filter. The ranges are determined by investigating the tracks in the STB and identifying the particles with irrational tracks. All the tracked particles during the STB are visualised in a volume, see Figure 3.17a, where the colours indicate the streamwise velocity. The effect on the tracked particles due to the applied range filter can be seen in Figure 3.17b. The difference between the two volumes is clear, as the range filter has removed particles with higher velocities (red particles). As part of the tracked particles are removed, the ratio between tracked particles and total particles is lowered. The prior STB ratio was 51% and has been lowered to approximately 35%, which, even though it is lower, is still deemed acceptable. Moreover, information about the flow field from prior experiments on the GCM has been taken into account for the determination of the ranges.

Table 3.9: Values for the range filter post-processing

Parameter	Range
Lateral Velocity	$-0.5 \cdot U_\infty$ to $0.5 \cdot U_\infty$
Vertical Velocity	$-0.5 \cdot U_\infty$ to $0.5 \cdot U_\infty$
Streamwise Velocity	$-0.1 \cdot U_\infty$ to $1.5 \cdot U_\infty$

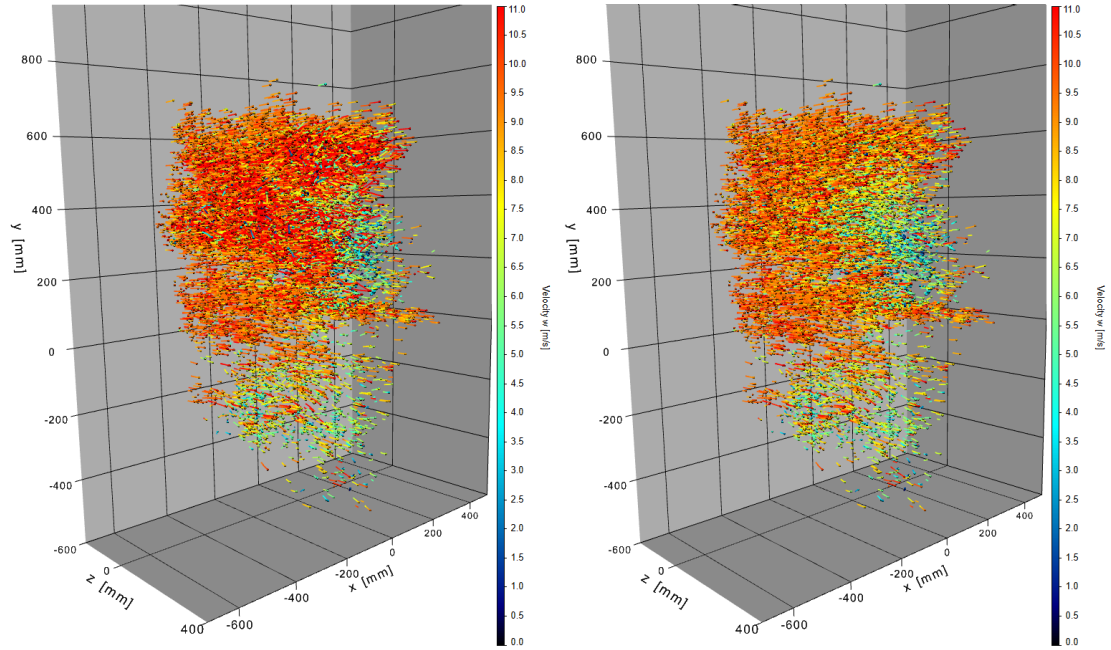

(a) Prior to range filter

(b) After the range filter

Figure 3.17: Tracked particles in the Shake-The-Box volume before and after the range filter for the Symmetric GCM at $10\ m/s$

The final step of the post-processing is the binning. The binning filter is performed after the STB and converts the active particle tracks into a vector dataset. The parameters and their values of the binning filter are written down in Table 3.10. An important parameter of the binning filter is the sub-volume size, which is selected to be $15\ mm$. This size was selected since it is the smallest bin size that still allows a large number of particles surrounding the wake of the cyclist. The number of particles in a bin is connected to the accuracy; large amounts in a bin create higher accuracy. However, a larger bin size causes the average to be incorrect. Meaning, that the most accurate binning is the smallest size with large amounts of particles, hence $15\ mm$ was chosen.
The binning filters lead to an averaged vector field, from which the velocity and vorticity fields can be derived. An example of the velocity field and the vorticity field with vectors downstream of the GCM is visualised in Figure 3.18.

Table 3.10: Values for the Binning post-processing

Parameter	Value	
Sub-volume size	60	mm
Overlap	75	%
Grid spacing	15	mm
Border tolerance	90	%
Spatial polynomial order	2	
Filter length (time steps)	5	

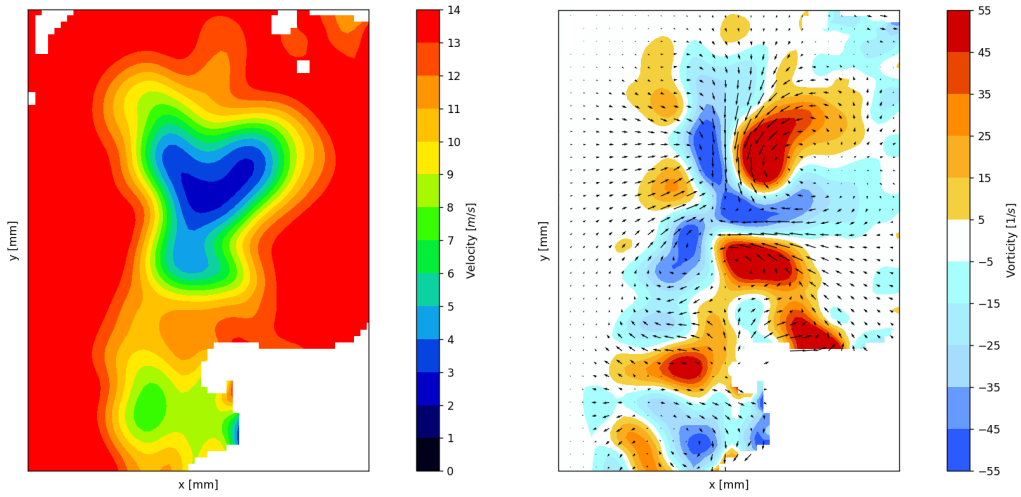

(a) Velocity field **(b)** Vector and vorticity field

Figure 3.18: Post-processing of the PIV images

3.7. Crosswind Corrections

To simulate crosswind in the wind tunnel, the GCM is rotated around its axis and thus receives the incoming airflow at an angle. However, in the real world, the cyclist is moving into the oncoming airflow at a crosswind angle. This difference between the real world and the wind tunnel must be corrected in both the aerodynamic loads and the flow field.

Due to the crosswind angle, the velocity of the air the cyclist experiences head-on alters from the airflow velocity of the wind tunnel, see Figure 3.19 for clarification. The rotation of the cyclist leads to a lower head-on velocity than the wind tunnel airflow; for this reason, the air velocity of the wind tunnel must be increase to ensure the cyclist's head-on velocity is similar to that at $0°$ by introducing a correction.

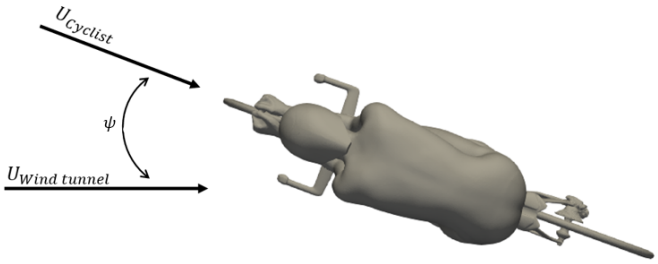

Figure 3.19: Schematic drawing of the Reynolds number - Crosswind correction

The correction is performed by applying Equation 3.7 to determine the wind tunnel velocity. The Reynolds number-Crosswind correction is only applied to the three highest yaw angles, $\pm 10°$, $\pm 15°$ and $\pm 20°$, as the smaller angles show an insignificant influence.

$$U_{\text{wind tunnel}} = \frac{U_{\text{cyclist}}}{\cos \psi} \tag{3.7}$$

The corrections are based on the reference run at $0°$, as the wind tunnel velocities are not similar to the input velocity, which will be discussed in subsubsection 3.8.1.1.
The differences caused by the Reynolds number-Crosswind correction are written down, and results are plotted in Appendix B, B.1. This shows that the differences are within 3%, outside of the repeatability margin (of 1%. Furthermore, the difference values differ for each velocity and crosswind angle, meaning the correction is inconsistent. Hence, it must be taken into account when comparing the drag area of high crosswind angles to low angles.

3.7.1. Flow Field Correction

During the crosswind tests, the GCM is rotated around its axis. However, the PIV system does not rotated with the GCM, and thus keeps its original axis system, as seen in Figure 3.20. Due to this, the velocity directions remain the same in the wind tunnel axis system. However, the flow field must be in the axis system of the cyclist to allow for comparisons. Hence, the PIV planes, or the post-processed data, must be rotated.

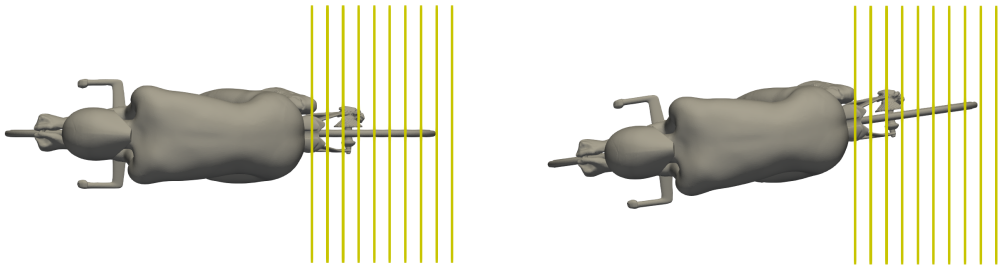

(a) No crosswind **(b)** At crosswind

Figure 3.20: The effect of the rotation of the GCM on the PIV planes

The rotation is applied to the velocity and vorticity of the flow field. The rotation is done by applying a rotation matrix to the data, see Equation 3.8 for the rotation on the velocity data. After this rotation, the velocities are in the axis system of the cyclist and are interpolated back onto the original planes. This ensures that the flow field can be compared at similar planes regardless of the crosswind angle.

$$U_{rotated} = \begin{bmatrix} \cos(\psi) & 0 & \sin(\psi) \\ 0 & 1 & 0 \\ -\sin(\psi) & 0 & \cos(\psi) \end{bmatrix} \times \begin{bmatrix} u & v & w \end{bmatrix}^T \tag{3.8}$$

The effect of the rotation and interpolation can be seen by comparing the non-rotated lateral velocity flow field, Figure 3.21a, to the rotated lateral velocity field, Figure 3.21b. The positive rotation of the flow field leads to lateral velocity, mostly coloured blue, with the vectors pointing to the left. From this rotated field, little information can be taken on the behaviour. Therefore, a correction on the lateral velocity must be applied to ensure readable flow fields. The correction is performed by Equation 3.9, which corrects for the lateral velocity of the freestream airflow velocity under a crosswind angle. The corrected lateral velocity flow field is given in Figure 3.21c. The correction looks similar to the non-rotated flow field; the effect is relatively small as the crosswind angles during the PIV measurements are small themselves, $\leq 8°$.
Given the small crosswind angles, the streamwise velocity shows a marginal to negligible change. However, for consistency and comparison, the flow field will be rotated.

$$u_{corrected} = u_{rotated} + U_{\infty} \cdot \sin(\psi) \tag{3.9}$$

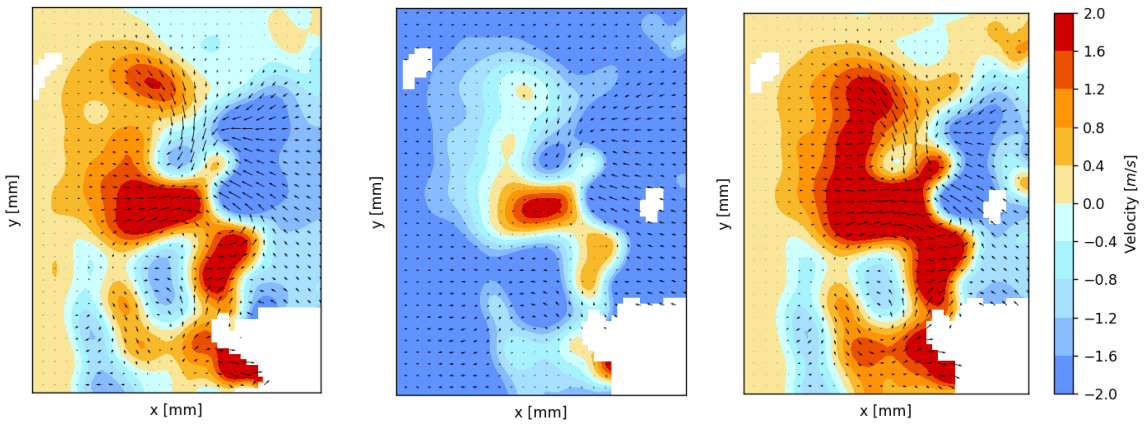

(a) Non-rotated **(b)** After rotation **(c)** After correction

Figure 3.21: The effect of the crosswind correction on the lateral velocity

3.8. Uncertainty

The experiment in the wind tunnel has uncertainty when it comes to its measurements. The uncertainties can lead to errors in the results and incorrect conclusions. For this reason, the uncertainty in the acquisition of the data must be quantified, and the influence on the results needs to be understood.

3.8.1. Aerodynamic Loads

The force balance has a maximum streamwise error in the measurements of around $0.15\ N$ [25]. This leads to different results when repeating tests. Furthermore, the PIV seeder has three different settings, which can lead to different results. Lastly, the boundary layer of the nozzle can lead to interference. The acceptable margin in the uncertainty of the drag area for the Symmetric and Asymmetric GCM is set at 1%. Meaning,

3.8.1.1. Velocity during the experiment

The wind tunnel experiment has different tests at multiple velocities ranging from 5 to $25\ m/s$. The wind tunnel is set up in a way that the preferred air velocity is input, which turns on the fan to a corresponding RPM (revolutions per minute). Within the wind tunnel, measurement devices such as wall surface pressure taps calculate the actual air velocity in the tunnel. The actual velocity and the input velocity do not always match, which is caused by the meshes in the wind tunnel not being clean.

The accuracy of the actual velocity in the wind tunnel compared to the input velocity is measured for all the individual tests. The median accuracy is listed in Table 3.11 for each velocity. As can be seen, for $14\ m/s$ and $15\ m/s$ the accuracy is around 100%, this is done on purpose, as these velocities are considered the representative velocity, and thus must be precise. In order to achieve a high accuracy, the input velocity value is increased until the actual velocity reaches the $14\ m/s$ or $15\ m/s$. This was not done for the other velocities. Based on the median, it can be seen that increasing the velocity leads to a decrease in accuracy, meaning the blockages in the meshes have stronger effects. In Appendix B, B.2, a more detailed figure shows the accuracy of all the velocities that were tested.

Table 3.11: Accuracy of the tested velocities

	Input Velocity $[m/s]$							
Parameter	5	10	12	14	15	18	20	25
Actual Velocity $[m/s]$	4.7	9.4	11.2	14.0	15.0	16.9	18.5	22.5
Accuracy	94.1%	93.7%	93.7%	99.9%	99.9%	93.8%	92.6%	90.0%

3.8.1.2. Comparison to prior experiment

The Asymmetric GCM has been tested prior to this experiment, which contained a first aerodynamic analysis as well as a crosswind study, [25] [16]. Next to this, the GCM has been tested once more in the OJF, and an experiment has been performed at Monash University in Australia. Between the prior tests, it was seen that the repeatability varies, leading to slightly different results.

For this reason, the Asymmetric GCM drag area results are compared to each of the prior experiments, see Appendix B, B.3 for plotted comparison. This showed that the current experiment lies within a respectable margin, as it lies between the other experiments' results.

The crosswind effect will be tested on the Symmetric GCM and compared to the Asymmetric GCM. Only one experiment has performed a crosswind test, [16], hence it is important to understand the difference between the two. Table 3.12 shows these differences at $0°$. From this, it can be seen that the current experiment yields higher drag area results than the prior experiment, with a maximum difference of 3.6%. Moreover, because the difference exceeds 1%, the drag area values cannot be compared with each other; however, the trends can.

Table 3.12: Difference in drag area to the prior yaw experiment of the Asymmetric GCM

	Input Velocity $[m/s]$							
Configuration	5	10	12	14	15	18	20	25
Asym GCM	1.4%	3.2%	3.6%	1.5%	1.0%	1.5%	2.0%	2.8%

3.8.1.3. Influence of the height of the fake floor

The cyclist is placed on a fake floor elevated to the exit of the wind-tunnel nozzle. The height of the fake floor can influence the aerodynamics of the cyclist, as the boundary layer of the OJF nozzle interacts with the cyclist. During the prior crosswind experiment with the Asymmetric GCM, the fake floor was placed at $2\ cm$ below the nozzle exit [16].
To limit the wind tunnel's boundary layer interaction, it is preferred to have the fake floor at $0\ cm$ above the nozzle, i.e. flush with the exit. Hence, the difference must be quantified.

The experiment yields that the difference between the heights is negligible; hence, all further tests can be performed with the fake floor flush to the nozzle. The results of the fake floor are plotted in Appendix B, B.4.

3.8.1.4. Influence of the PIV seeder

The PIV seeder, which is used to inject helium-filled soap bubbles (HFSB) into the airflow during the PIV measurements, is positioned in the settling chamber of the wind tunnel. This means that even during test which do not have PIV measurements, the seeder is still present. The seeder itself has three options: be fully turned off, be turned on with air injected into the airflow or be turned on with HFSB. The HFSB are only used during PIV measurement for cost-saving reasons. During the force balance measurements, the seeder is turned on with air. Hence, the difference in drag area between the seeder options must be quantified.

Table 3.13 shows the difference between the seeder turned off, and the seeder turned on with HFSB to the seeder turned on with air. On average, the seeder turned off has a difference of 0.2%. However, as the difference is both positive and negative, meaning the turned off seeder has a lower drag area for lower velocities and higher drag area for higher velocities. For this reason, it is better to look at the absolute values for the difference, which leads to an average of 1.1%. This, next to the highest values being around 2%, means the difference cannot be neglected. Hence, all force balance tests must be done with the seeder turned on with air.
Looking at the seeder turned on with HFSB, the average is -0.3%, while absolute values lead to 0.6%. This shows that the difference between the turned on with air or HFSB is within the acceptable margin, hence, force balance measurements can be done without having the HFSB. Appendix B, B.5 shows the influence of the seeder options for different crosswind angles. It shows that the HFSB for both $-8°$ and $8°$ have an average of 0.6% difference compared to the seeder turned on with air.

Table 3.13: Difference in drag area between the options of the PIV seeder at $0°$ crosswind compared to the seeder turned on with air, tested on the Asymmetric GCM

	Input Velocity $[m/s]$							
Configuration	5	10	12	14	15	18	20	25
Seeder Off	-1.8%	-1.0%	-0.2%	0.8%	1.0%	2.1%	1.2%	-0.8%
Seeder on with HFSB	-0.4%	-0.2%	-0.3%	-0.8%	-1.2%	0.5%	0.3%	-*

* No measurements were performed with the HFSB at $25\ m/s$

3.8.1.5. Repeatability

The repeatability error of reinstating the cyclist mentioned in subsubsection 3.8.1.2 was for the Asymmetric GCM compared to prior experiments, and hence, the repeatability of the Symmetric GCM during the same experiment must be investigated. As the force balance itself has an error in its measurements, as well as the rotation in the fake floor and disassembling and reinstating the GCM, lead to uncertainties in the drag area.

The repeatability is tested in different ways, the repeatability in consecutive runs, in non-consecutive runs, between before and after dismounting the GCM and the repeatability using hysteresis.
The consecutive repeatability is tested by performing the same test with the same configuration twice in a row. While the non-consecutive repeatability is performing the same test with the same configuration on different days, with a different configuration being tested in between. The reinstating of the GCM, as mentioned before, was retested as there is wiggle room in the placement of the bike on the struts and the rider on the bike. Lastly, the hysteresis is tested. All tests are performed by starting the test at $5\ m/s$,

then performing measurements at $10\ m/s$, increasing the velocity again until all tests are performed. During the hysteresis, the tests were opposite, meaning starting at $25\ m/s$, and then lowering the velocity until all the tests have been done.

To quantify the uncertainty, the error of each repeatability case is calculated compared to the reference run. This run is the first run of the Symmetric GCM. All the errors per case per velocity is written down in Table 3.14, while more detailed results can be found in Appendix B, B.6. As seen, the consecutive repeatability showed only an error of 0.2% on average, with an outlier of 0.6%, all within the acceptable margin. The non-consecutive repeatability, on the other hand, shows a bigger error of, on average, -0.5%. This shows that as the experiment progresses, the drag area decreases. Outside of the outlier of 2% at $5\ m/s$, the error remains within an acceptable margin.

Thirdly, the dismount-mount repeatability is tested, the error is split into two categories; the error between the run just before the dismount and the run after the dismount (the mount) and the error between the mount and the reference run. Based on Table 3.14, it shows that the error between the dismount and mount is high for lower velocities, while the error reduces at higher velocities. On average, the error is 1.2% with is outside of the acceptable margin; however, it is in line with the error from previous experiments as mentioned in subsubsection 3.8.1.2. When comparing the (re-)mounted GCM to the reference run, the error is reduced, except for the error at $5\ m/s$, it falls within the acceptable margin. For this reason, the experiment is continued without altering the GCM position.
Lastly, the hysteresis is investigated. The error, on average, is only -0.3%, and thus within the margins. By testing in the opposite direction, from high velocities to low, the drag area is lower than the reference run at velocities lower than the representative velocity.

Table 3.14: The error in drag area in repeatability of the Symmetric GCM for the consecutive, non-consecutive, dismount-mount and hysteresis cases at $0°$ crosswind

	Input Velocity $[m/s]$							
Case	5	10	12	14	15	18	20	25
Consecutive	-0.1%	-0.2%	0.1%	0.2%	0.6%	0.2%	0.1%	0.1%
Non-consecutive	-2.0%	-1.0%	-0.8%	-0.5%	-0.2%	-0.2%	-0.1%	0.4%
Mount to dismount	3.8%	1.5%	1.3%	0.9%	0.8%	0.2%	0.4%	0.7%
Mount to reference	1.8%	0.5%	0.5%	0.4%	0.6%	0%	0.2%	1.1%
Hysteresis	-0.7%	-1.0%	-0.6%	-0.4%	0%	-0.1%	0.1%	0.6%

Based on the uncertainty of the multiple repeatability cases, several cases have higher errors than the acceptable margin. For this reason, all the Symmetric GCM runs at $0°$ will be averaged when comparing to different configurations. The averaging reduced the uncertainty and gives a more accurate result.

3.8.2. Particle Image Velocimetry

During the post-processing of the flow field captured by PIV, the results of the flow field per image are averaged into one flow field (per location relative to the GCM). All images show variations in the flow field compared to the average; therefore, the standard deviation of the velocity field is examined. The standard deviation of the lateral, vertical and streamwise velocity is given in Figure 3.22.
Based on the figures, the streamwise velocity has a higher standard deviation compared to the lateral and vertical velocities. This can be linked to the streamwise velocity having a higher magnitude, and the streamwise velocity is linked to the lateral and vertical flow. Meaning, changes in the lateral velocities will be seen in the streamwise flow; similarly, changes in both the lateral and vertical velocities are combined and thus greater in the streamwise direction.

The higher standard deviation areas surround the wake of the Symmetric GCM. This indicates that the wake oscillates behind the cyclist. The higher region of deviation near the lower left leg can be explained in a similar way, oscillating leg wake.
The maximum deviation is 30%, which is in line with previous experiments, [16]. Hence, the data is deemed accurate enough to investigate the effects of the Reynolds number, crosswind and flow control devices.

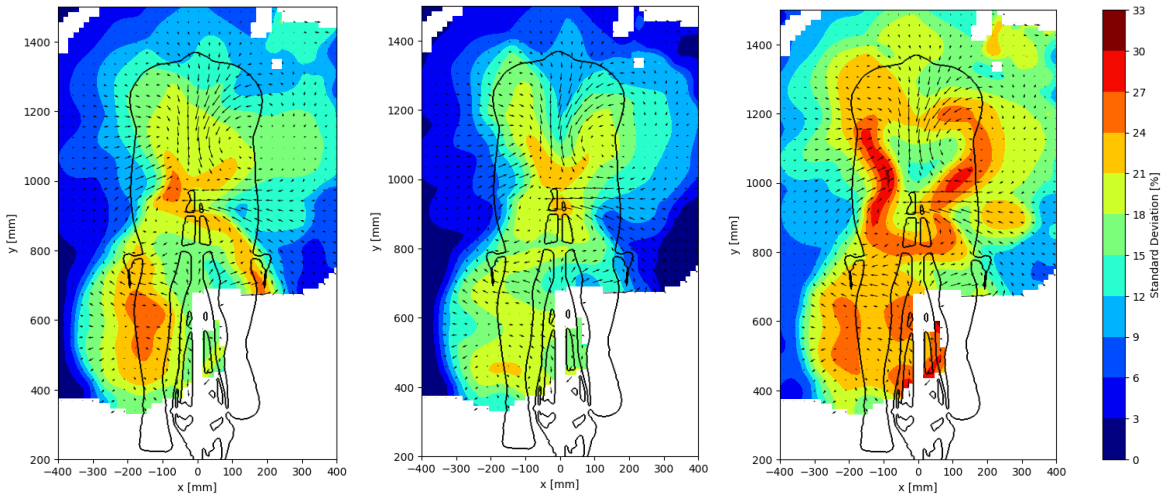

(a) Lateral velocity **(b)** Vertical velocity **(c)** Streamwise velocity

Figure 3.22: Standard deviation of the velocity of the post-processing of the PIV images of the Symmetric GCM at $14\ m/s$ at $0°$

Next to the Symmetric GCM, the Asymmetric GCM has been tested in the experiment. The standard deviation at $14\ m/s$ of the Asymmetric GCM is given in Figure 3.23a. Similarly, the deviation surrounds the wake of the GCM, however, some differences can be noted. The Asymmetric GCM has a much higher standard deviation near the left leg, due to the straighter position compared to the Symmetric GCM.
For a direct comparison between the standard deviations, the contours of the region of at least 24% are drawn and compared in Figure 3.23b. From this, the differences are even clearer, especially near the left leg of the GCM's.

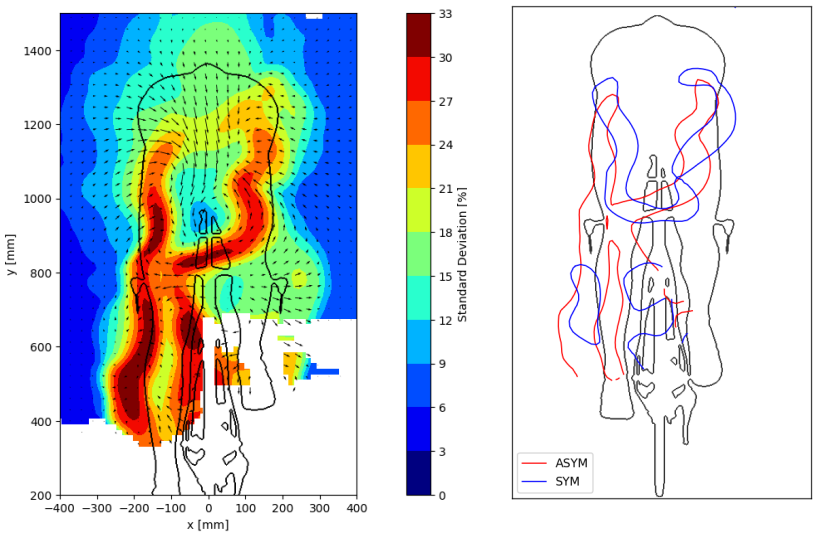

(a) Asymmetric GCM **(b)** Contour of the standard deviation at 24%

Figure 3.23: Comparison of the streamwise velocity standard deviation between the Asymmetric and Symmetric GCM at $14\ m/s$ at $0°$

Besides the standard deviation at $14\ m/s$ at $0°$, different velocities and crosswinds were tested, as well as flow control devices. These standard deviations can be found in Appendix B, B.7.
The standard deviation at the velocity $10\ m/s$ or at a crosswind angle of $8°$ are larger than the deviation of the reference velocity and no crosswind.

4

Results

This chapter details the results of the force balances and PIV measurements of the Symmetric and Asymmetric GCM. The sections are linked to the categories to answer the research question: influence of the leg position, Reynolds number variations, crosswind and the addition of flow control devices.

4.1. Influence of the Position of the Legs

In the experiment, the aerodynamic flow field is measured in a 3D volume by using LPT (Lagrangian Particle Tracking) or 3D PIV. The volume is located behind the cyclist up to the end of the rear wheel. This allows for a detailed flow field analysis and the effect of moving downstream the volume.

The Symmetric and Asymmetric GCMs are tested during the experiment to evaluate the influence of the symmetric leg position compared to the asymmetric position. In Figure 4.1, the wake, the disturbed airflow, is visualised for both GCMs. The airflow is coloured based on the velocity, with red meaning freestream velocity, $14\ m/s$, and blue indicating $\approx 3\ m/s$. Certain characteristics are similar: the body generates a large upper wake, with the head wake on top of it. Another similarity is the low velocity region behind the cyclist, near the saddle (indicated in blue).

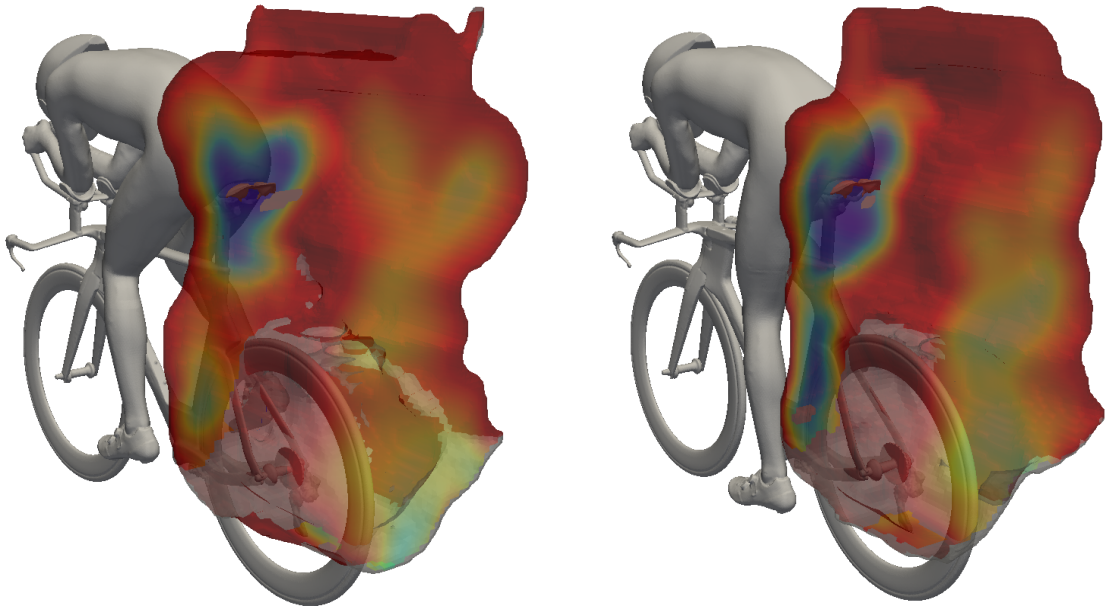

(a) Symmetric GCM **(b)** Asymmetric GCM

Figure 4.1: The aerodynamic flow field in 3D of the Symmetric and Asymmetric GCM at the reference velocity, $14\ m/s$

Differences between the Symmetric and Asymmetric GCMs are evident in the 3D volume, particularly in the shape of the upper wake and the lower-velocity region behind the left leg. The differences in the wake can be linked to the position of the legs, meaning that the posture shows a great effect.

Furthermore, it is calculated with the force balance measurements that the Symmetric GCM has a 4.6% lower drag area at the reference velocity, $14\ m/s$, compared to the Asymmetric GCM.

The 3D images of the aerodynamic flow field and the drag area can already provide an answer to the first category of the research question; the position of the legs influences the aerodynamics of the GCM.

In addition to the aerodynamic wake of the cyclists, the vortices generated by the model can be visualised in the 3D volume. The Symmetric GCM has multiple vortices generated by the hips and thigh, which are shown in Figure 4.2. The Symmetric GCM has three distinct vortices near the hips and thighs, with a counter-clockwise rotating vortex, CCR, (red), stemming from the right upper hip, a CCR vortex (red) underneath the saddle, likely generated by the upper front body and thighs and a counter-rotating vortex, CR (blue). The CR vortex is a combination of four smaller vortices stemming from the lower hips, both left and right, the left upper hip and the left inner thigh.
The lower part of the GCM has multiple smaller vortices, two CCR vortices generated by the calves, and vortices generated by the ankles, feet, paddles and parts of the wheels.

The upper vorticity flow field of a cyclist in a symmetric leg position has been investigated previously, [6]. In this experiment, it was found that the vortices were symmetrical, with two upper hip vortices and two inner thighs. This experiment shows a different location of vortices. The discrepancies can lie in multiple things, for instance, the cyclist's posture. In the current experiment, the head is positioned down, and the arms are pointed upwards and placed close together. The older experiment has the head positioned up with the arms pointing downwards and further apart. Secondly, the measurement technique is different. Furthermore, the legs are in the opposite direction.
During the prior experiment, pressure probes were used at different 2D plane locations and using interpolation, the vortices were calculated. However, in this case, the vorticity was measured in a 3D volume by PIV.

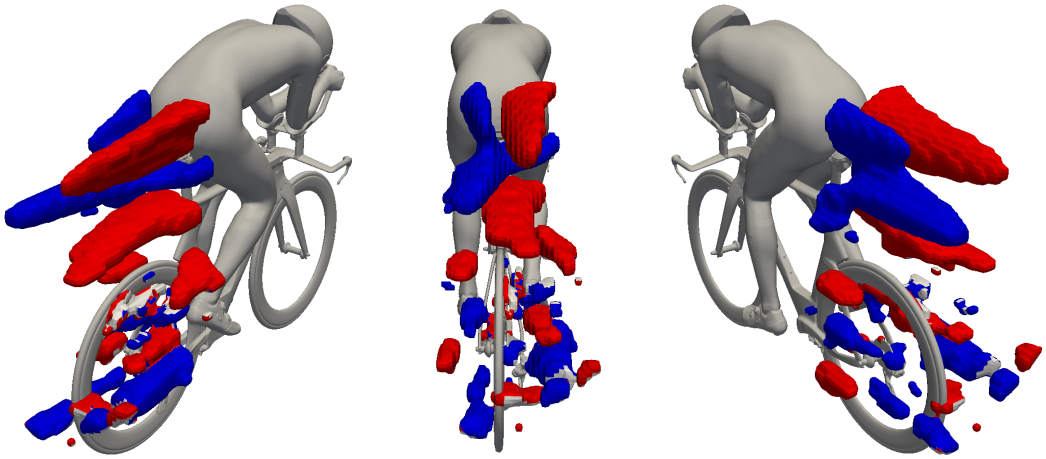

Figure 4.2: The 3D streamwise vorticity of the Symmetric GCM at $14\ m/s$
Counter-clockwise rotating vortex indicated by red and clockwise rotating vortex indicated by blue
Note, only vortices with a strength of $|\omega \cdot L/U_\infty| \geq 1$ are visualised

The vorticity of the Asymmetric GCM is shown in Figure 4.3. As can be seen, the vortices are at different locations compared to the Symmetric GCM. Here, there are three upper vortices: a large CCR vortex generated by the inner thighs and two CR vortices stemming from the left upper and lower hips. The Symmetric GCM has the same two CR vortices on the left; however, they are less strong, indicating that an extended left leg makes them stronger. The right lower CR hip vortex on the Symmetric GCM, is barely visible in the Asymmetric case. This leads to a single CCR inner thigh vortex. On the other hand, it can be said that the stronger CCR inner thigh vortex and connections to the small upper right hip vortex do not allow for a lower right hip vortex, since a lot of upwash is generated behind the right hip. As the Symmetric GCM has a weaker inner thigh vortex that is also positioned lower, it allows for a CR vortex at the lower hip, which splits the two CCR vortices. The vortices of the Asymmetric GCM last longer due to the higher strength than the Symmetric GCM. This observation has been seen in

prior experiments on the crank angle, [6].
In terms of the lower vortices, differences are more difficult to find. A clearer difference is the CCR vortex behind the left leg, which is weaker in the Symmetric case, which can be tied to the leg being less straight and positioned more forward.

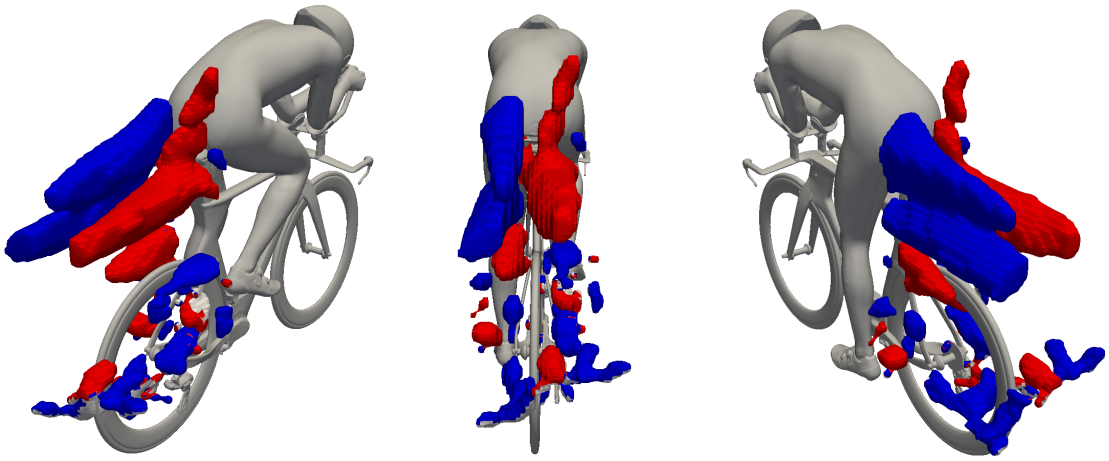

Figure 4.3: The 3D streamwise vorticity of the Asymmetric GCM at $14\ m/s$
Counter-clockwise rotating vortex indicated by red and clockwise rotating vortex indicated by blue
Note, only vortices with a strength of $|\omega \cdot L/U_\infty| \geq 1$ are visualised

The leg position of the cyclist influences multiple aerodynamic behaviours, including the wake and the vortices. By moving from an asymmetric to a symmetric position at the reference velocity, the cyclist reduces its drag area by 4.6%. This is visualised by the changes in the flow field, where the velocity in the wake is increased; next to this, the shape becomes more symmetrical. Moreover, the vortices are moved to slightly different locations and dissipate earlier, meaning the strength is decreased.

4.1.1. Planar Flow Field Behind the Saddle

From the 3D volume of flow field data, 2D flow fields can be taken at different locations behind the cyclist. The streamwise velocity field of 6 planes behind the cyclist and the distance relative to the end of the saddle, d, is visualised in Figure 4.5. The locations of these planes relative to the GCM are shown in Figure 4.4.

Moving downstream, from plane 1 to 6, shows that the wake size is reducing and the velocity within the wake is increasing. The differences in wake size and velocity are mainly visible in the upper region. The lower region, wake caused by the legs, shows a slight expanding motion due to the presence of the wheel. The rear wheel stops the combination of the left and right leg wakes. Additionally, the wheel, chain and sprockets have a wake.
Another difference in the 2D planes is the amount of white area. The white regions in the figures are caused by the lack of particles in that region. The particles do not reach the bottom part of the cyclist, due to the position of the seeder in the OJF. Also, due to the PIV cameras and LEDs being on the left side of the cyclist, the rear wheel blocks part of the view, resulting in white data around the right knee. Moreover, the flow field is measured at the rear wheel; thus, they must be blocked as there are no particles in this region.

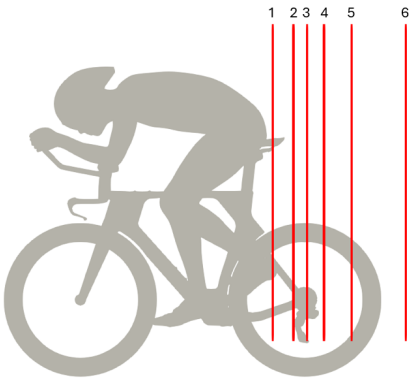

Figure 4.4: Location of 2D planes

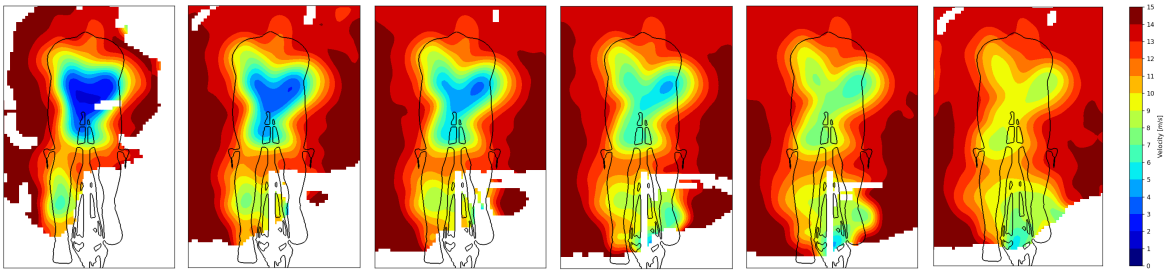

(a) Plane 1 $d = -54\ mm$ **(b)** Plane 2 $d = 36\ mm$ **(c)** Plane 3 $d = 97\ mm$ **(d)** Plane 4 $d = 173\ mm$ **(e)** Plane 5 $d = 294\ mm$ **(f)** Plane 6 $d = 536\ mm$

Figure 4.5: 2D streamwise velocity at different planes behind the Symmetric GCM at $14\ m/s$

To examine the flow field of the Symmetric GCM and for comparisons with prior experiments, the 2D field behind the saddle, between plane 1 and 2, will be analysed.

The velocity flow field behind the saddle of the Symmetric GCM at $14\ m/s$ is given in Figure 4.6. The flow field indicates the wake of the Symmetric GCM. The wake consists of two regions of lower velocity: the upper region caused by the body and the lower region caused by the legs. Besides the velocity flow field, the magnitude and direction of the lateral and vertical velocity are visualised by vectors. The upper wake region shows a lower velocity relative to the legs. This can be explained by two things: the body is larger than the lower leg, leading to more airflow being displaced, thus generating a larger wake. Secondly, the lower left leg is positioned more upstream than the rearward part of the body, meaning that this plane shows the wake further away from the leg, leading to a more recovered wake.
Due to the lack of flow field data in the right lower region, the wake of the right lower leg cannot be visualised and hence, no conclusion can be made on the leg wake.

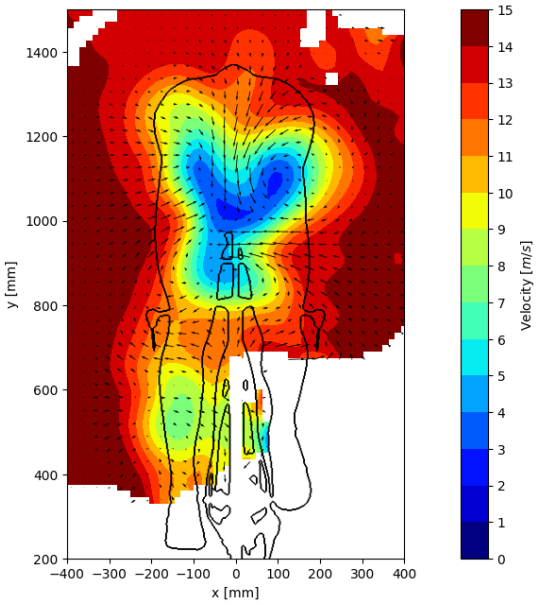

Figure 4.6: Velocity flow field of the Symmetric GCM at $14\ m/s$

For comparison reasons, the velocity is normalised, which is done by dividing by the freestream velocity, in this case $14\ m/s$. The velocity field can be split up into the three directions, lateral, vertical and streamwise velocity, which is given in Figure 4.7.

The normalised lateral velocity shows clear characteristics, inwash over the right hip (bended leg) indicated by the blue region, inwash above the left hip indicated by the red area, and an outwashing motion over the legs, air flowing to the left behind the left leg, indicating an expanding leg wake. The inwash on both sides is a logical response as the airflow must be recovered behind the object. The difference

in strength of the left and right side of the inwash can be linked to the position of the legs, with the right hip giving a stronger response due to the bend in the leg.
The normalised vertical velocity shows a strong downwash over the back of the GCM. This is because the airflow follows the curvature of the head, neck and back of the cyclist. The downwash is only at the centre of the back as the sides are affected by inwash, leading to a small upwashing motion.
The normalised streamwise velocity indicates the wake of the cyclist behind the saddle. The characteristics of the lateral and vertical velocities are visible in the wake shape, as the wake is compressed near the hips and near the back. The expanding movement seen in the lateral velocity can be seen in the streamwise velocity flow field by the lower velocity region behind the left calf.

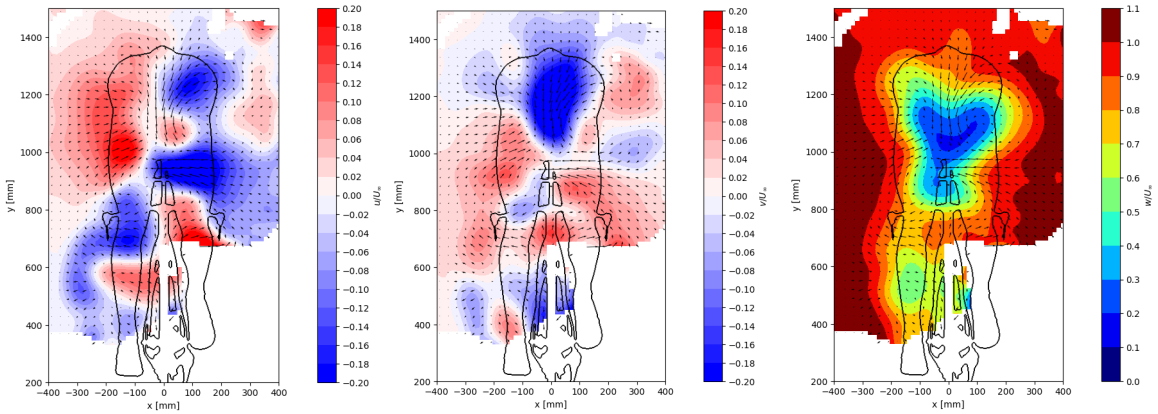

(a) Lateral velocity **(b)** Vertical velocity **(c)** Streamwise velocity

Figure 4.7: The velocity flow field in three directions of the Symmetric GCM at $14\ m/s$

The vorticity of the GCM, meaning the rotations in the airflow, is analysed in a 2D plane behind the saddle. The vorticity, which was already shown in the 3D volume, is in the streamwise direction, ω_z. For comparisons, a normalisation has been applied by multiplying by the hip length and dividing it by the freestream velocity, $(\omega_z \cdot L/U_\infty)$.
In Figure 4.8a, the normalised vorticity flow field of the Symmetric GCM at the reference velocity, $14\ m/s$ is given. The 2D plane shows the three upper vortices, the two counter-clockwise rotating (CCR) vortices of the upper right hip and the inner thighs, and the clockwise rotating (CR) vortex that is a combination of the upper left hip, lower hips and the left inner thigh. The upper CCR vortex can be linked to the downwash over the cyclist's back and the inwash over the right shoulder. The second CCR vortex, generated by the inner thighs, is linked to the inwash over the right hip. Similarly, CR vortices are related to downwash on the back and inwash on the right hip.

The vorticity in the leg region shows multiple areas with different rotations. With CCR airflow near the left knee and a CR airflow near the calf. The right leg has too little information to analyse the vorticity.

To determine the strength of the vortices, the Q-criterion is analysed. The Q-criterion is normalised by multiplying it by L^2/U_∞^2 and given in Figure 4.8b. From this, the three vortices in the upper region become clearer. It can be seen that the inner thigh vortex is a combination of two vortices positioned above each other. Moreover, the lower hip vortex before combining with the main CR vortex is visible. Furthermore, the two CCR vortices are stronger at the saddle plane.
Additionally, the vortices near the lower legs become more visible, with the knee and calf vortices. Similarly, around the left ankle, a vortex is present; however, as it is on the border of the data volume, no definite conclusions can be made. Likewise, the Q-criterion flow field shows two vortices between the right leg and wheel, which, due to being on the border of the data volume, cannot be taken into account for the analysis.

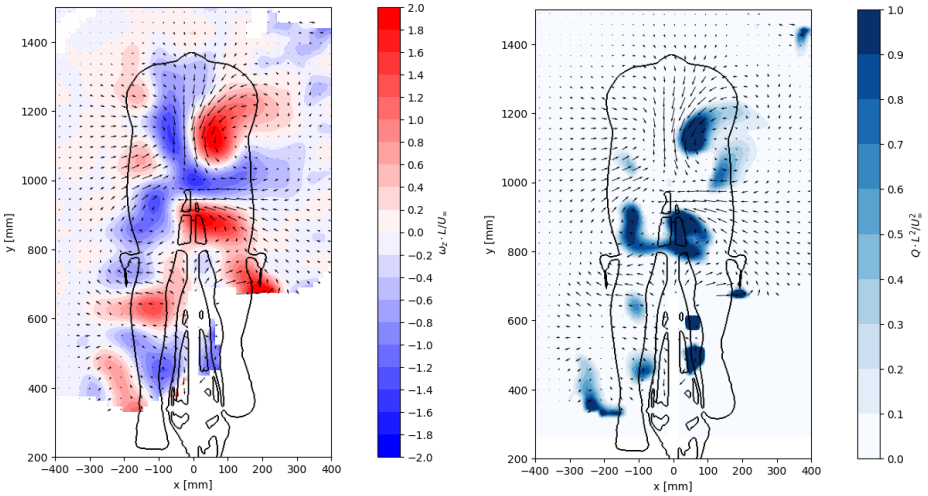

(a) Streamwise vorticity **(b)** Q-criterion

Figure 4.8: The streamwise vorticity and Q-criterion of the Symmetric GCM at $14\ m/s$

4.1.2. Comparison to the Asymmetric GCM

From the 3D volume, differences can be spotted in the Asymmetric and Symmetric GCM. To analyse the differences, the 2D flow field behind the saddle is compared.

The normalised streamwise velocity at the freestream velocity of $14\ m/s$ of the Asymmetric GCM shows a clear difference in the wake, see Figure 4.9. The Symmetric GCM has two part of the wake, the upper part and the lower part. For the Asymmetric GCM, the upper and lower parts are connected at the straight left leg. The Asymmetric GCM has a wake with lower velocity spanning over the entire left leg, with the lowest velocity at the calf. Furthermore, the Asymmetric GCM has a 'tilt' in the upper wake, with the wake being higher at the right side than the left. Similarly, the left leg has a lower velocity wake while the upper right leg does not. This shape is quite different from the Symmetric GCM, where the right shoulder has a slightly cleaner air region. Moreover, around the saddle/left hip, a region of low velocity is present at the Asymmetric GCM, while for the Symmetric GCM, the region is smaller and has higher velocity. For comparison, the contour at $w/U_\infty = 0.85$ of the Asymmetric and Symmetric GCMs is given in Figure 4.9c. The tilt in the Asymmetric GCM wake is clearly visible, and the Symmetrical GCM seems to have a slight tilt in the opposite direction. Comparing the wake of the left leg it can be seen that the width is the same for both GCMs.

The wake width of the Asymmetric GCM and Symmetric GCM is relatively the same; still, there is a 4.6% drag area difference. The differences are likely caused by the velocity in the wake of the Asymmetric GCM being much lower, as well as the straighter leg generating a bigger wake.

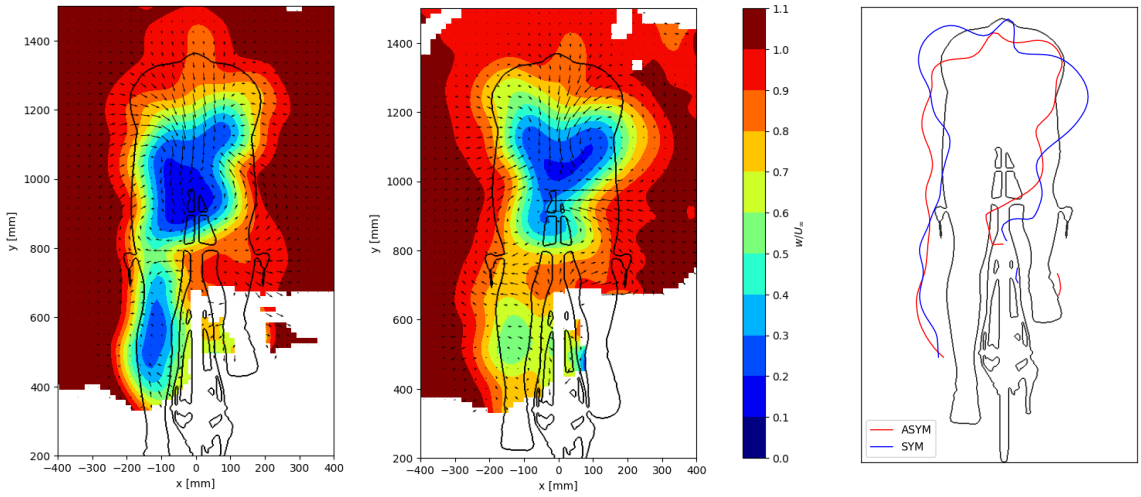

(a) Asymmetric **(b)** Symmetric **(c)** Contour $w/U_\infty = 0.85$

Figure 4.9: Comparison of the streamwise velocity flow field of the Asymmetric and Symmetric GCM at $14\ m/s$

The differences in the streamwise velocity wake can be explained by the lateral and vertical velocity. Both normalised lateral and vertical velocity flow fields of the GCMs are given in Figure 4.10.
The normalised velocity flow field shows clear differences between the two GCMs. The Symmetric GCM has inwash over the right hip, while the Asymmetric GCM has outwash. On the left side, the Symmetric GCM has a smaller and weaker inwash region. While it has a stronger inwash on the right side. Near the left leg, the airflow is outwashing, while for the Asymmetric GCM, a combination of in and outwash can be seen.
The Asymmetric GCM has a stronger, larger downwash and is positioned on the left side of the centre of the GCM's back. This is because the downwash over the back is pulled towards the straight leg. Comparing this to the Symmetric GCM, the downwash is smaller in area and weaker, which can be linked to the left leg 'pulling' less on the wake as it is positioned less straight.
The combination of stronger inwash and downwash over the body of the Asymmetric GCM results in the tilt in the upper wake. Comparing the wake shapes, it can be said that the Symmetric GCM has a more symmetrical upper wake.

From this, it can be concluded that the leg position has a strong effect on the wake of the GCM. The aerodynamic flow fields of the Asymmetric GCM have larger magnitudes in lateral and vertical velocities as well as lower velocity in the streamwise velocity, which is in line with the expectations based on prior experiments and the drag area difference.

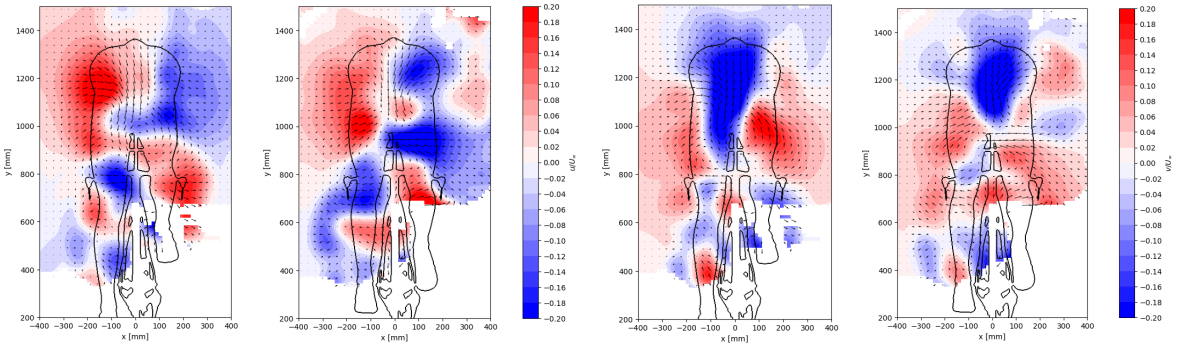

(a) Asymmetric - u/U_∞ **(b)** Symmetric - u/U_∞ **(c)** Asymmetric - v/U_∞ **(d)** Symmetric - v/U_∞

Figure 4.10: The normalised lateral and vertical velocity flow field of the Symmetric GCM and Asymmetric GCM at $14\ m/s$

As determined by the 3D vorticity flow field, the Asymmetric and Symmetric GCMs show differences in locations and strength of the vortices. Hence, the 2D planes will show the differences. The streamwise

vorticity of both GCMs is given in Figure 4.11a and 4.11b. A noticeable difference in the upper part of the vorticity field is the split of counter-clockwise (CCR) and clockwise rotation (CR) vortices. The upper left side of the Asymmetric GCM only shows CR vortices, and the right side only shows CCR vortices. Comparing this to the Symmetric GCM, which has CR vortices on both the left and right sides. Next to this, the CR vortices of the Symmetric GCM combine, while the Asymmetric GCM shows two distinct CR vortices. This is the opposite of the CCR vortices, where the Symmetric GCM shows two distinct vortices, which are combined for the Asymmetric case.

Besides the location and orientation of the vortices, the magnitude of the vorticity fields shows that the Symmetric GCM has weaker vortices. To give an insight into the strength, the Q-criterion has been visualised in Figure 4.11c and 4.11d. These flow fields show that the vortices of the Symmetric GCM area are weaker and positioned differently compared to the Asymmetric GCM. This is in line with the theory mentioned in chapter 2.

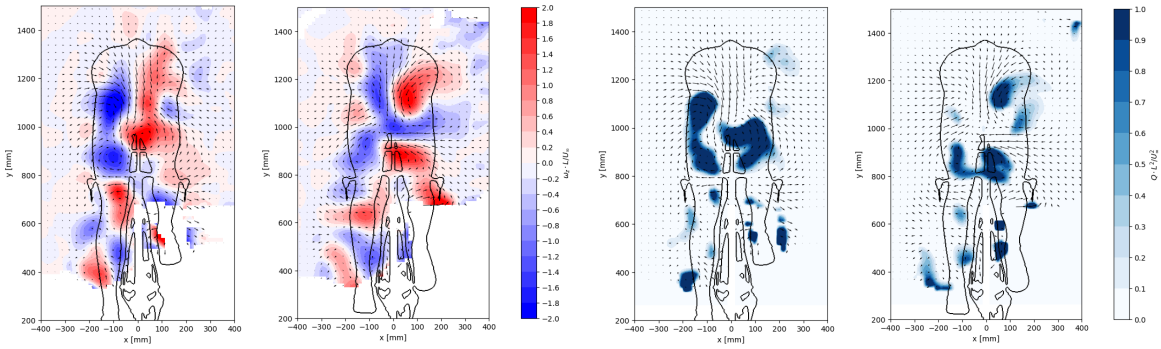

(a) Asymmetric - ω_z **(b)** Symmetric - ω_z **(c)** Asymmetric - Q **(d)** Symmetric - Q

Figure 4.11: Comparison of the streamwise vorticity and Q-criterion of the Asymmetric and Symmetric GCM at $14\ m/s$

4.1.2.1. Asymmetric GCM Compared to Prior Experiments

As mentioned in section 3.8, the aerodynamic loads of the Asymmetric GCM differ by approximately 2% from a prior experiment. It could be that there are differences in the flow field as well, hence it must be investigated.

The 3D wake of the crosswind experiment compared to the current experiment is shown Figure 4.12a and 4.12b. The 3D wake of the experiments shows a similar trend, with a difference being noticeable in the low velocity wake (indicated in blue). The wake has a similar shape throughout the 3D volume; note the measurement volume of the crosswind experiment is smaller.
Figure 4.12c and 4.12d show the 2D plane behind the saddle. The velocity in the wake of the crosswind experiment reaches lower values than in the current experiment. This is mainly near the saddle and the left leg.

The differences in the flow field can be caused by the setup of the experiment, as the location of the cameras and LEDs differ. This is the reason for the lack of data near the right leg of the current experiment. However, the differences in velocity values are likely caused by the post-processing. As the post-processing has multiple steps, pre-processing, STB, filter range and binning. Any one of the values can be linked to the difference in the flow field. Another possibility is the amount of particles in the airflow during the PIV measurements,

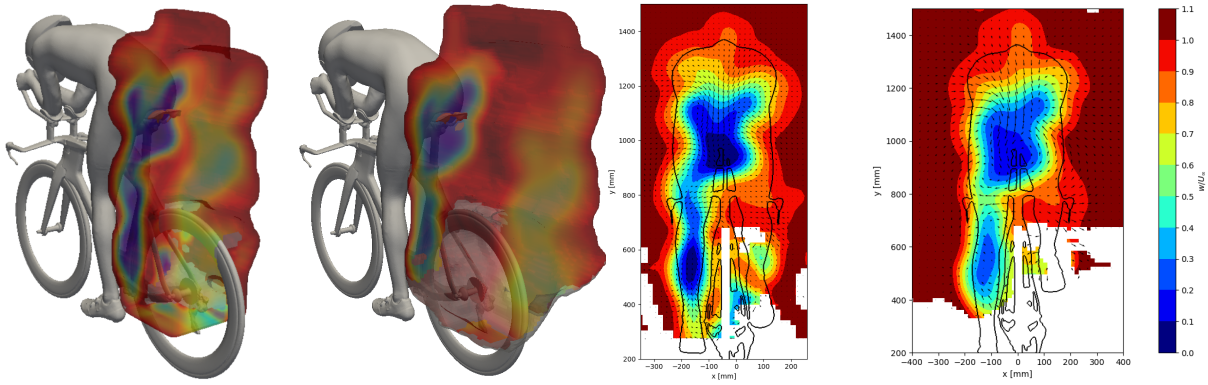

(a) Crosswind experiment
Data from Maleki Dastjerdi, 2025 [16]

(b) Current experiment

(c) Crosswind experiment
Data from Maleki Dastjerdi, 2025 [16]

(d) Current experiment

Figure 4.12: 3D and 2D wake of the Asymmetric GCM during different experiments

Furthermore, the vorticity of the Asymmetric GCM has been measured in two prior experiments, and is shown in Figure 4.13. The first analysis of the Asymmetric GCM is given by Figure 4.13a, including the names of the multiple vortices. This experiment measured the flow field from the shoulders up to the rear wheel, and thus shows the vortices stemming from the arms and upper body. The second experiment, the crosswind experiment, Figure 4.13b, has a shorter measurement volume and only shows the vortices behind the cyclist up to halfway the rear wheel.

Comparing both prior experiments to the results of the current Asymmetric GCM, Figure 4.13c, shows that the vortex structure is the same. With two clockwise rotating (CR) vortices on the left side and a counter-clockwise rotating (CCR) vortex on the right. The first experiment shows the structures more detailed, and seems to last shorter. Comparing the crosswind experiment to the current, the crosswind experiment shows stronger vortices, especially near the right upper high and near the lower legs. The vortices seem shorter; however, this is due to the measurement volume being smaller.

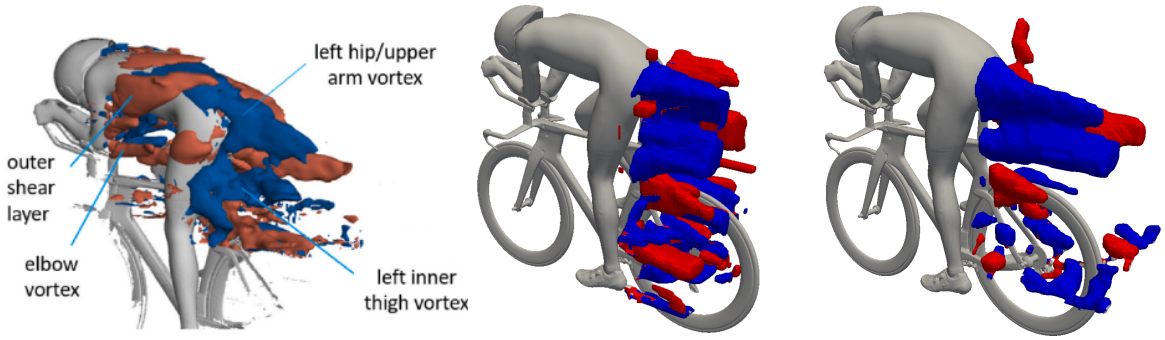

(a) First experiment
Taken from Terra, 2024 [25]

(b) Crosswind experiment
Data taken from Maleki Dastjerdi, 2025 [16]

(c) Current experiment

Figure 4.13: 3D streamwise vorticity of the Asymmetric GCM during different experiments

Similarly to the wake, the 2D vorticity field of the crosswind and current experiment is compared and shown in Figure 4.14. As seen, the vorticity in the crosswind experiment has much higher values than in the current experiment. This is similar to the streamwise wake different, where the magnitude of the crosswind experiment is higher.

The magnitude difference can be caused by the processing values, as mentioned before. Even though the difference in magnitude is large, the size and regions of the wake are relatively similar. For this reason, the aerodynamic flow field measurement of the asymmetric GCM of this experiment is deemed acceptable for comparisons.

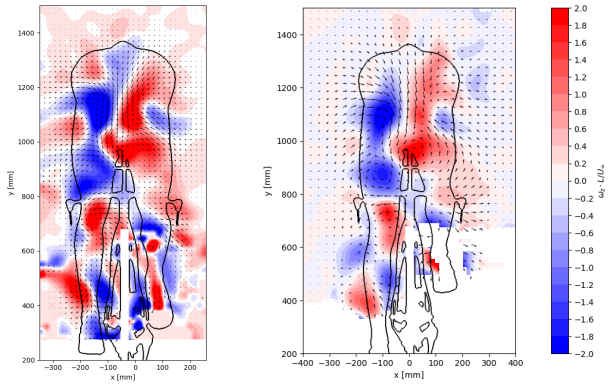

(a) Crosswind experiment Data taken from Maleki Dastjerdi, 2025 [16]

(b) Current experiment

Figure 4.14: 2D streamwise vorticity of the Asymmetric GCM during different experiments

4.1.3. Conclusion

The effect of altering the leg position leads to a drag area reduction. Furthermore, the leg position alters the flow field of the cyclist, with the symmetric leg position having higher velocities in the wake. The Asymmetric GCM has a greater downwash over the back and a larger inwash from the left side. While the Symmetric GCM shows an inwash airflow behind the right hip.

The vortices stemming from the hips and thighs of the cyclist are altered by the leg position. The symmetric GCM has clockwise rotating vortices from the upper and lower left hip that combine with the lower right hip and left inner thigh. The combining of vortices does not happen for the Asymmetric GCM. The 2D images show that the Symmetric GCM has a relatively symmetrical shape. Next to this, the left leg wake and the upper wake are not combined for the Symmetric GCM, while they are combined for the Asymmetric GCM. Furthermore, the Symmetric GCM has weaker vortices that dissipate earlier than the Asymmetric GCM.

4.2. Influence of the Reynolds Number Effect

The influence of the speed of the cyclist is investigated by measuring the drag area and the flow field. A cyclist does not ride at a constant velocity, but rather changes their velocity throughout their route. It becomes important to analyse the aerodynamics at multiple velocities to give a more detailed overview of what a cyclist experiences.

4.2.1. Aerodynamic Loads

The drag area, $C_D A$, for the Symmetric GCM is plotted in Figure 4.15 per velocity, this is the average of the 4 runs that have been performed. Similar to the Asymmetric GCM experiments, the drag area reduces as the air speed is increased, with a total decrease from $5\ m/s$ to $25\ m/s$ (more accurately between the actual velocities $4.7\ m/s$ and $22.6\ m/s$) of 11%. The reason for the drag area reduction is attributed to the critical Reynolds number. As mentioned in subsection 2.1.2, the flow is in a transition state around a bluff body at critical Reynolds numbers. This transition state, meaning to air flow goes from laminar to turbulent separation, triggers a reattachment after the flow has separated [1] [2] [27]. Due to the reduction, the wake width is reduced leads to less drag. In the case of the Symmetric GCM, the arms and legs of the cyclist are considered bluff bodies and thus have a critical condition. From the velocities tested during the experiment, as well as the atmospheric conditions, the Reynolds numbers can be calculated, which are within the critical Reynolds number range $10^5 < R_e < 5 \cdot 10^5$, see Appendix C, C.1. Based on the graph, it can be concluded that the drag crisis, the minimum drag area of the cyclist, happens at a higher velocity than the $25\ m/s$ (or actual velocity of $22.7\ m/s$).
Using the reference velocity, $14\ m/s$, it is measured that lower speeds (around $5\ m/s$) lead to a drag area increase of 6.3%. Increasing the velocity to $25\ m/s$ results in a reduction of 4.5% in drag area.

The uncertainty of the model and the experiment, mentioned in section 3.8; consecutive, non-consecutive, dismount-mount and hysteresis, are visualised in the form of error bars. As can be seen, the biggest uncertainty is present at $5\ m/s$, which ranges from -2% to 2%. In contrast, the errors of the other velocities are within a per cent, with an outline at $25\ m/s$ of 1.1%.

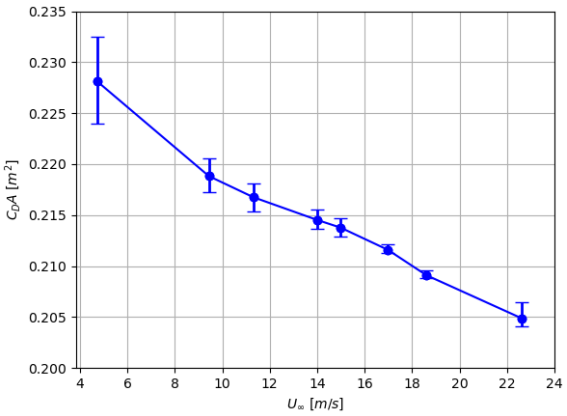

Figure 4.15: The Reynolds Number effect of the Symmetric GCM including uncertainties

Based on the experiment carried out on the crank angles of a cyclist, as mentioned in subsubsection 2.2.1.2, a variation of 15% was observed in the drag area between a symmetric leg position and an asymmetric position, [6]. From this, it is expected that the Symmetric GCM yields a lower drag area than the Asymmetric GCM. The results of the Reynolds number effect of the Symmetric and Asymmetric GCM of this experiment have been plotted in Figure 4.16a.
The Symmetric GCM has a lower drag area at each velocity, which bigger differences at lower velocities. The largest difference is 8.7%, with the smallest being 3.5%. Even though the difference between the Symmetric and Asymmetric GCM is signifiant it is not as large as in the crack angle study. As mentioned in subsubsection 2.2.1.1 and 2.2.1.3, cyclist posture and arm position have a substantial effect on drag area and wake-up. The cyclist in the crank angle experiment has a different upper body posture, as it is sitting higher, and a different arm position, being wider, than the GCM. This difference can be linked to the variation in drag area reducing between the experiments.

The total reduction seen in the Reynolds number curve for the Symmetric GCM is 11%, while that of the Asymmetric GCM is 15%. This shows the Asymmetric GCM is more affected by the variation than the symmetric leg position. This indicates that the leg has a substantial effect on the drag area.
Furthermore, the drag coefficient, C_D, is estimated for the Symmetric and Asymmetric GCM by dividing the drag area by the frontal area, see Figure 4.16b. Since the frontal area is the same for both GCM's, the offset between the two Reynolds number curves is equal to that of the drag area.

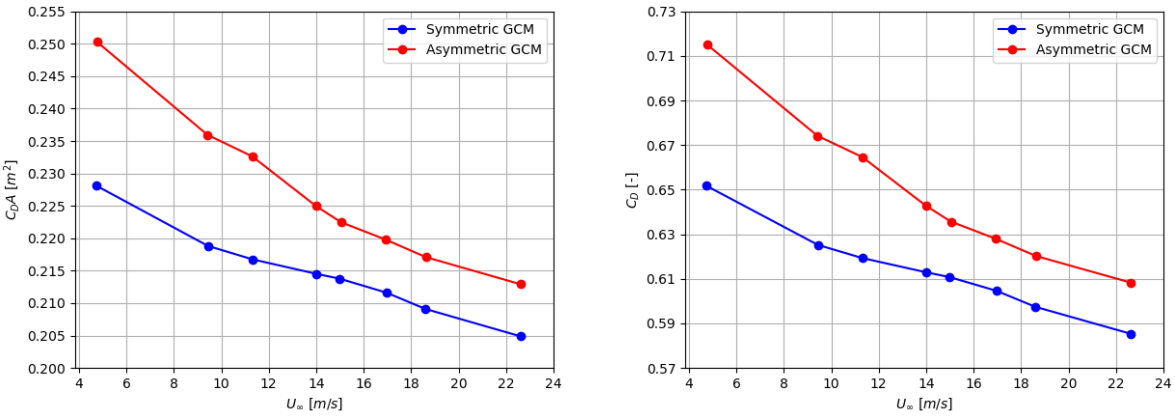

(a) Drag area, C_DA

(b) Drag Coefficient, C_D

Figure 4.16: Symmetric GCM compared to the Asymmetric GCM
Frontal area, A of both GCMs is $0.35\ m^2$

4.2.2. Aerodynamic Flow Field

To visualise the effect of the Reynolds number on the flow field of the Symmetric GCM, the normalised streamwise velocity, w/U_∞, is compared. In Figure 4.17, the velocity fields are given for the three velocities, 10, 14 and $18\ m/s$, or rather the actual velocities 9.7, 14 and $16.7\ m/s$. A noticeable difference in the figures is that $10\ m/s$ has more regions without any data, white areas. However, the white regions are outside of the GCM and thus pose no issues for the comparison.

The upper part of the wake shows the main differences caused by the Reynolds number variation. The shape of the upper part, near the head, shows an increase in a 'dip' when the velocity is increased. This can be linked to the increase in downwash over the back of the GCM when the velocity is raised. At $10\ m/s$ the downwash is 15% weaker than at $14\ m/s$, while at $18\ m/s$ the downwash is increased by 5% compared to the reference velocity. The dip is not only visible in the outer layer of the wake, but also at the core (dark blue region), which shows the strength of the downwash. This dip also makes the upper wake more symmetrical, meaning the higher the velocity, the more symmetrical the wake becomes. Next to this, the inwash from the right side of the GCM is increased both in magnitude and area when the velocity is raised. The opposite is true for the inwash from the left side of the GCM, where the velocity increase leads to a weaker inwash. The comparison of lateral and vertical velocity at the different Reynolds numbers are given in Appendix C, C.2.
The combination of less downwash and the inwash difference leads to the wake of the $10\ m/s$ case having a different shape, with the lower velocity area being mainly present behind the right side of the GCM. The inwash over the left and right hips leads to the compressing of the wake. This behaviour is unchanged when the velocity is raised.

The leg, more specifically, the left lower leg wake is altered due to the Reynolds number effect. The increase in velocity leads to the wake width being decreased. The more compressed wake also leads to a smaller region of low velocity ($w/U_\infty \approx 0.55$). This behaviour is in line with the critical Reynolds number theory, where the increase in velocity leads to the airflow staying attached longer and reducing the wake width. The lateral velocity flow fields show that the outwash behind the calf, the reason for the expanding wake, is not present at the $18\ m/s$ case.
At the $10\ m/s$, the right leg shows a small lower velocity area; however, the accuracy of the wake is undetermined since the rear wheel blocks most of the light and view of the cameras.

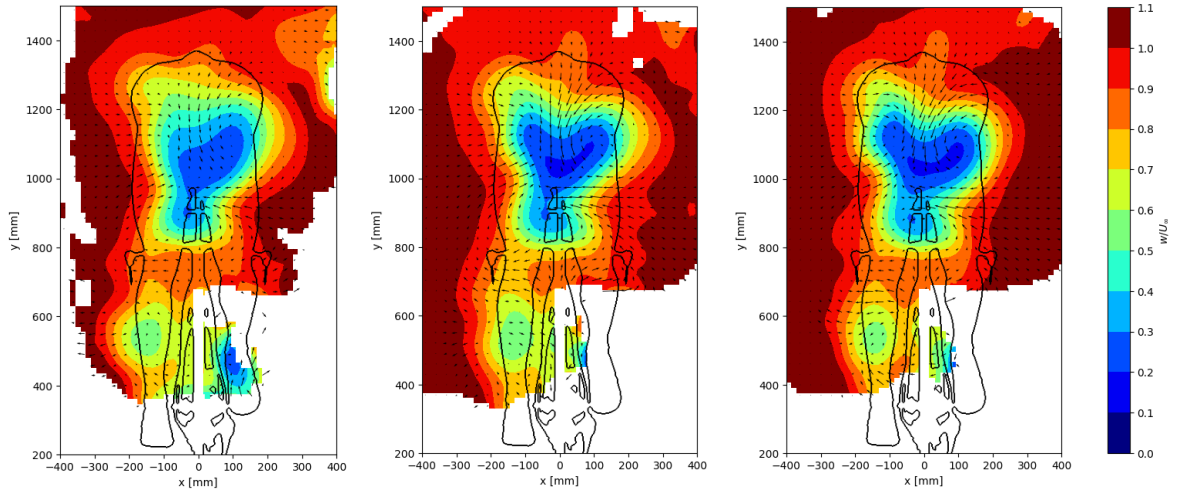

(a) $10\ m/s$ **(b)** $14\ m/s$ **(c)** $18\ m/s$

Figure 4.17: The normalised streamwise velocity flow field of the Symmetric GCM at different velocities

To visualise the effect of the Reynolds number on the wake width and shape, the contours of the wakes are drawn in Figure 4.18. The contours are taken from the normalised streamwise velocity, at $w/U_\infty = 0.85$, corresponding to the orange region in the above images.
As can be seen in the contours, the upper wake shows slight differences, mainly due to the dip in the

wake. The $18\ m/s$ case leads to a smaller upper contour, while $10\ m/s$ results in the highest. The region near the legs shows a more similar wake difference, and does not provide any extra information.

From the force balance measurement, it is calculated that the $10\ m/s$ case has a 2% higher drag area than the $14\ m/s$, next to this, $18\ m/s$ case has a 1.4% drag area reduction.
The small difference in drag area can be caused by the small differences in wake width (height), with $18\ m/s$ having a slightly smaller wake and thus a lower drag area. However, as the right leg wake is not visible due to the lack of data, no definite conclusion can be made on the overall wake.

Comparison of the drag area data with the flow fields reveals a theory that the leg wake has a greater influence on the drag area than the upper wake. This is based on the velocity in the upper wake, which should indicate that the $10\ m/s$ case has the lowest drag area; however, it is not.

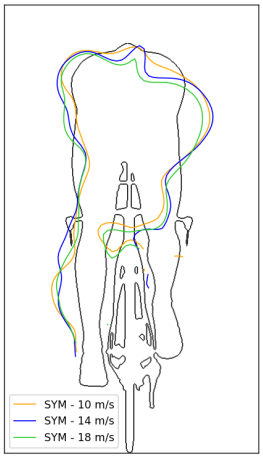

Figure 4.18: Comparison of the wake at $w/U_\infty = 0.85$ of the Symmetric GCM at different Velocities

The effect of the Reynolds number on the normalised streamwise vorticity is given in Figure 4.19. The influence of the velocity increase is relatively small, with the location of the vortices being unchanged. The strength of the vortices, however, is altered. The counter-clockwise rotating (CCR) vortex stemming from the right upper hip is stronger at $10\ m/s$ compared to $18\ m/s$. The multiple CR vortices in the upper wake are more spread out when the velocity is increased. The opposite is observed at the lower region of the vorticity, where an increase in velocity leads to a lower (absolute) magnitude.

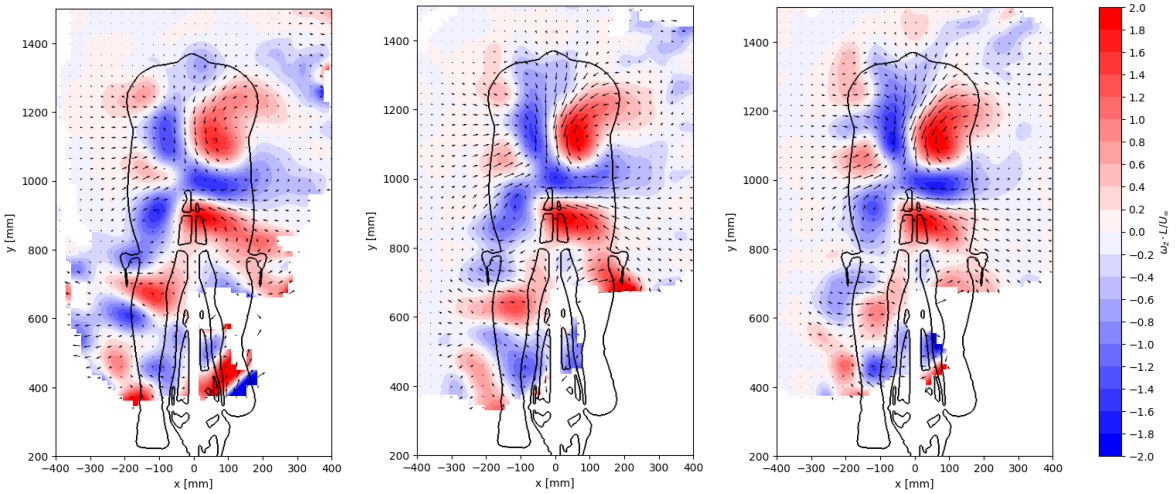

(a) $10\ m/s$ **(b)** $14\ m/s$ **(c)** $18\ m/s$

Figure 4.19: The normalised vorticity, ω_z of the Symmetric GCM at different velocities

As the strength of the vortices seems to be the main difference caused by the Reynolds number, the normalised Q-criterion is visualised, see Figure 4.20.
As stated before, the strength of the CCR vortices increases when the velocity is raised, while the CR vortices decrease in strength. The lower vortices are decreased in strength due to the Reynolds number increase.
The drag reduction caused by Reynolds number increase, is difficult to explain with the vorticity and Q-criterion flow fields. As the increase in the strength of vortices normally leads to an increase in the drag area, while here the opposite is observed. The right leg is missing vital information about the generation of vortices. Stronger vortices from the right leg at $10\ m/s$ compared to weaker ones at $18\ m/s$ could explain the Reynolds number effect.

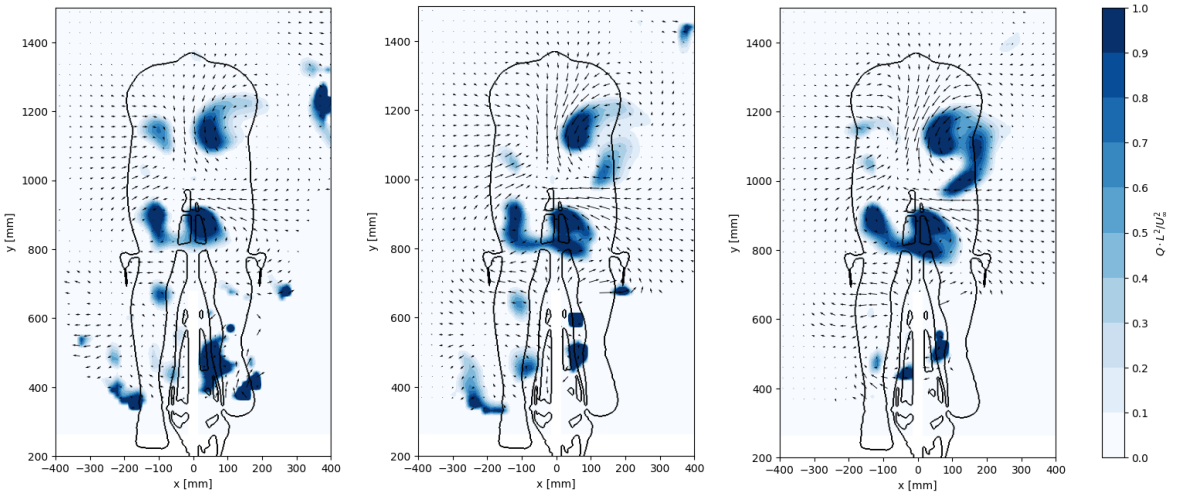

(a) $10\ m/s$ **(b)** $14\ m/s$ **(c)** $18\ m/s$

Figure 4.20: The Q-criteria of the Symmetric GCM at different velocities

4.2.2.1. Comparison to Asymmetric GCM

The Reynolds number effect is tested on the Asymmetric GCM to analyse whether the flow field, which has a similar behaviour. The normalised streamwise velocity is visualised in Figure 4.21 for the three velocities as well as the contour at $w/U_\infty = 0.85$.
The aerodynamic loads indicate that the $10\ m/s$ has a 4.9% higher drag area than the $14\ m/s$, while the Symmetric GCM only shows a 2% higher drag. For the $18\ m/s$ case, the drag area is lowered by 2.2% for the Asymmetric GCM, while the Symmetric GCM has a 1.4% reduction.

The Asymmetric GCM shows clear differences in the wake between velocities, with the $10\ m/s$ case showing a higher minimal velocity region, $w/U_\infty \approx 0.35$ in the upper part, compared to the $w/U_\infty \approx 0.15$ at $14\ m/s$ and $18\ m/s$. This is similar to the Symmetric GCM. Comparing the lateral and vertical velocities, Appendix C, C.2.1, the inwash from the upper left side of the GCM becomes connected with the outwash over the right hip when the velocity is increased. Next to this, the inwash behind the right upper body is stronger in magnitude and smaller in region at $10\ m/s$ compared to the $18\ m/s$ case. This is a similar behaviour to the Symmetric GCM. The downwash over the back of the GCM increases when the airflow is raised, with $10\ m/s$ having 16% less downwash than $14\ m/s$, and the $18\ m/s$ case shows a slight increase of 1% in downwash. Comparing this to Symmetric GCM, which showed a 16% reduction and a 5% increase, respectively.

The leg wake of the Asymmetric GCM shows a difference which is in line with the bluff body critical Reynolds number theorem; increasing the velocity leads to a wake width reduction. This behaviour is less visible in the Symmetric GCM, indicating that a less straight leg behaves less like a bluff body (or cylinder).

The contours, Figure 4.21d, are similar to the Symmetric GCM, with the $10\ m/s$ case having a larger wake at the upper part, near the head and shoulders. The head wake of the $18\ m/s$ looks bigger in the

contours; however, this is likely caused by the limit of the contour. The other parts of the contour show no differences caused by the Reynolds' number variation.

The flow fields of the Asymmetric GCM are in line with the theory that the wake caused by the legs has a greater influence on the drag of the cyclist than the wake generated by the body.

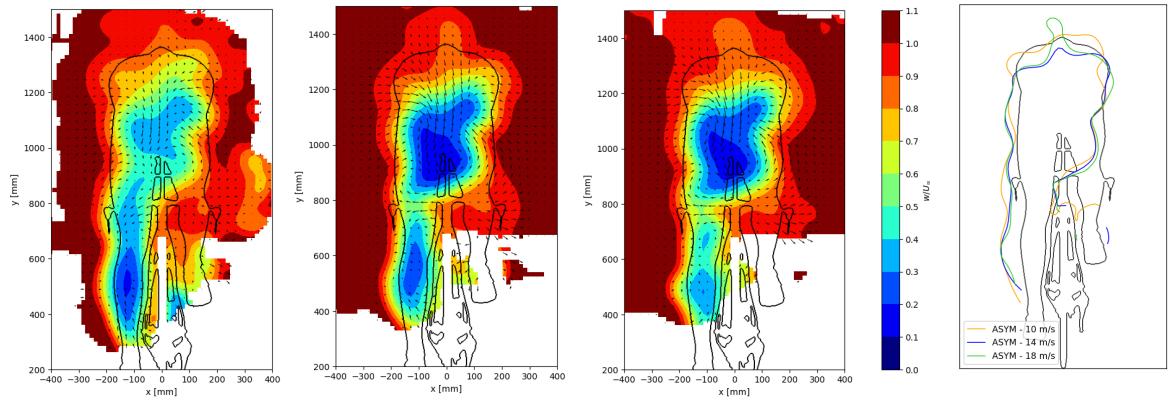

(a) $10\ m/s$ **(b)** $14\ m/s$ **(c)** $18\ m/s$ **(d)** Contour $w/U_\infty = 0.85$

Figure 4.21: The normalised streamwise velocity flow field of the Asymmetric GCM at different velocities

The vorticity of the Asymmetric GCM is compared at different velocities in Figure 4.22. It can be seen that the location of the vortices does not alter when the velocity is increased, which is similar to the Symmetric GCM. Likewise, the strength of the vortices is increased when the velocity is raised. As can be seen, at $10\ m/s$, the left upper and lower hip vortices are spread out over the region, while at $14\ m/s$ and $18\ m/s$, it shows two clearly stronger regions, the vortices. Based on the Q-criterion, Appendix C, C.2.1, it is clear that the strength of all the vortices in the upper wake is increased when the velocity is raised, while the lower vortices are weaker at higher velocities. This behaviour is similar for the Symmetric GCM.

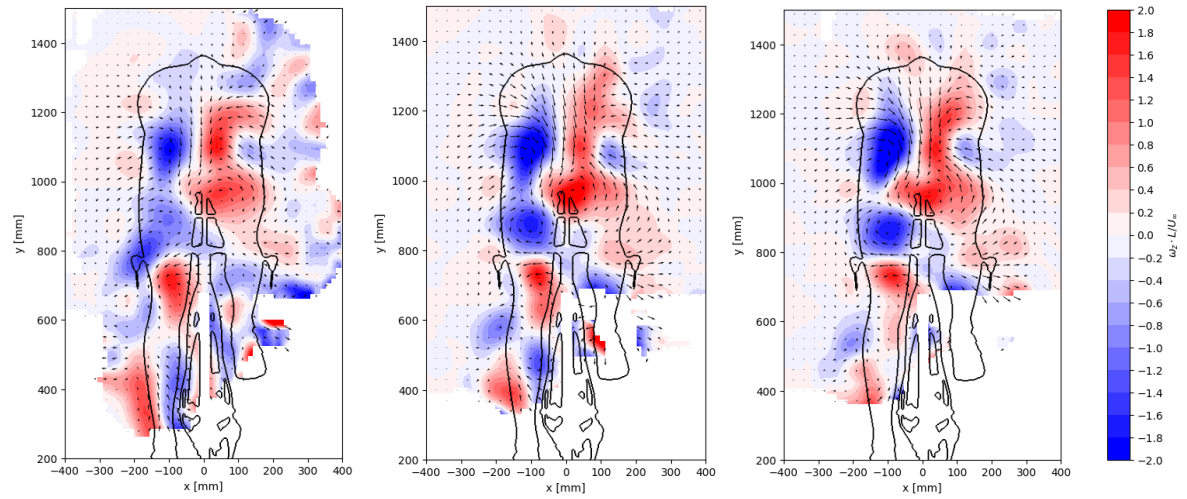

(a) $10\ m/s$ **(b)** $14\ m/s$ **(c)** $18\ m/s$

Figure 4.22: The normalised vorticity, ω_z of the Asymmetric GCM at different velocities

4.2.3. Conclusion

The effect of the Reynolds number variation on the drag area of the Symmetric GCM is apparent, and an increase in velocity leads to a drag area reduction. This effect is related to critical Reynolds number theory. The decreasing drag area trend of the Symmetric GCM, a total of 11% between $5\ m/s$ and $25\ m/s$, is similar to the Asymmetric GCM, which has a drag reduction of 15%.

The Reynolds number effect is visible in the aerodynamic flow field of the Symmetric GCM, where a higher velocity leads to a more symmetrical wake shape. Furthermore, the upper wake is slightly decreased at higher velocities, which explains the drag area reduction. The left leg wake has a similar behaviour, with wake width decreased. However, as the right leg cannot be analysed, a definite conclusion between the drag area and the wake cannot be made. Nevertheless, the theory is that the wake by the legs affects the drag area more than the wake by the body.
The Reynolds number variation also affects the vorticity, which shows that the upper vortices increase in strength as the velocity is increased, while the lower vortices become weaker.

Comparing the Symmetric to the Asymmetric GCM, the influence of the leg position can be seen. While the same behaviours are spotted, wake decreases at higher velocities and vortices become stronger; some slight differences can be noted. The left leg of the Asymmetric GCM is more affected by the Reynolds number variation. Based on the critical Reynolds number, it can be said that the straighter leg (asymmetric position) acts more as a bluff body or cylinder than the less straight leg of the symmetrical position.

4.3. Crosswind Effect

During the experiment, the cyclist was rotated to simulate crosswind rather than experiencing the airflow head-on. This is done as in the real world, the cyclist is more likely to experience a crosswind.

4.3.1. Aerodynamic Loads

The effect of the introduction of a crosswind of the Symmetric GCM is tested at angles ranging from $-20°$ to $20°$ at each velocity. In Figure 4.23, the Reynolds number effect at each crosswind angle is plotted. The negative angle, meaning the rotation leading to the straighter leg (left leg) being in the oncoming airflow, is given in Figure 4.23a, whereas the positive angle, bent leg in oncoming air is plotted in Figure 4.23b. The Reynolds number curve at $0°$, the blue line, is used as a reference to understand the behavioural changes. Comparing the negative and positive angles, a difference can be spotted, indicating that the difference in the lower leg position impacts the drag area of the GCM. A more detailed comparison, where the angles are split between the negative and positive value is given in Appendix D, D.1.

In both negative and positive angles, it can be seen that greater angles result in drag area reductions. The highest angles, $\pm 15°$ and $\pm 20°$ show a convergence in the Reynolds number curve, indicating that the minimum drag area is achieved, which falls in line with the critical condition theorem discussed in subsection 2.1.2. Furthermore, the highest negative angle $-20°$ has a higher drag area value than $-15°$ at lower velocities, while at higher velocities the opposite is observed. This is contrary to the positive angles, where $15°$ leads to the lowest drag area at higher velocities than $20°$.

Comparing the smallest angles, $\pm 2°$ and $\pm 4°$, to the reference, only small changes can be spotted, indicating that the rotation is not large enough. The angles $-2°$ and $-4°$ have a negligible and small reduction influence, respectively, while $2°$ and $4°$ shows a slight increase in drag area. Larger influence can be seen when comparing $-6°$ and $-8°$ to $6°$ and $8°$. The positive angles only show relatively small changes, with $6°$ resulting in a drag area increase and $8°$ leading to a small drag area reduction. The negative angles, however, lead to a bigger drag reduction with, on average, a reduction between $6°$ to its counterpart of 8.5%. The largest difference is seen between $-8°$ and its counterpart, with an average of 10.7%. For $-10°$ and $10°$, the difference is greater at lower velocities with a maximum difference of 11%, while at the higher velocities the difference is around 1%. The two largest angles are close to each others counter part with the difference around 3%. In almost all cases, the negative angles lead to a lower drag area then its counterparts.

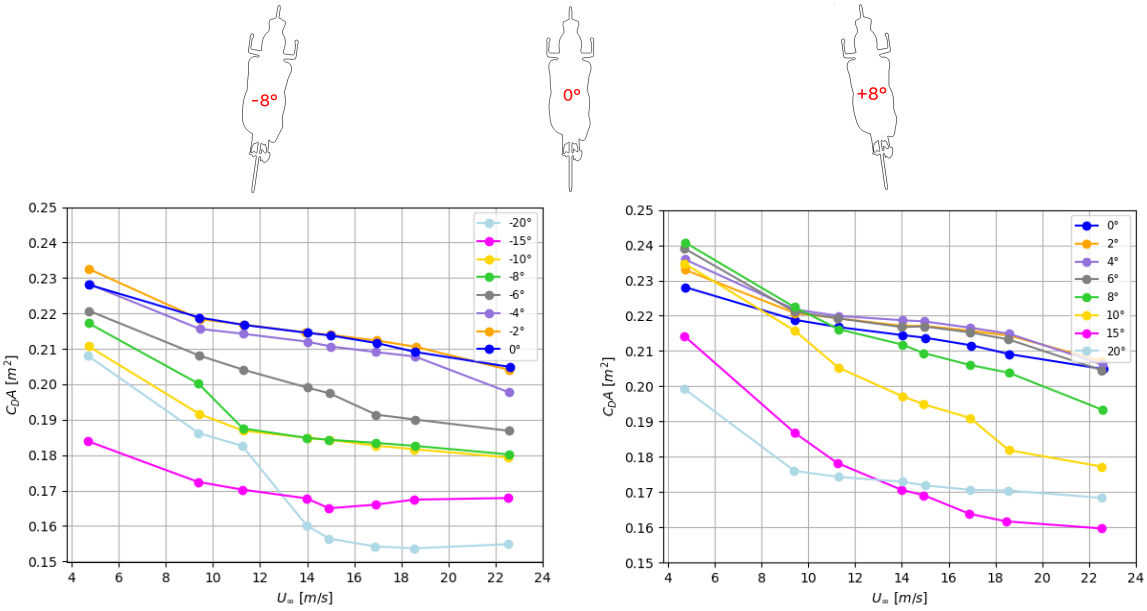

(a) Negative crosswind

(b) Positive crosswind

Figure 4.23: The effect crosswind has on the Symmetric GCM on the Reynolds number sweep

The difference in drag area between positive and negative crosswind angles can be linked to the lower leg position. The lower part of the bent leg is positioned close to the upper leg, meaning that at $0°$, the wake of the bent leg is concise. When the bent leg starts to rotate into the airflow, the bent leg wake becomes widened, leading to an increase in drag area at low positive angles. When the angle increases, the lower part of the leg reaches more oncoming airflow and reacts as a bluff body rather than in combination with the upper part of the leg.
For the negative angles, the straightest leg is in the oncoming airflow. The lower part and upper part are further away from each other and thus have less interaction than in the case of the bent leg. For this reason, the increase in crosswind angle has a more straightforward result.

A different way of displaying the effect crosswind has on the drag area of the Symmetric GCM is by plotting each velocity per crosswind angle, see Figure 4.24a. It is evident that, small positive angles lead to an increase in drag area, whereas lower negative angles lead to small decreases. Moreover, the drag area at $5\ m/s$ is substantially higher than at other velocities, which is linked to being in a sub-critical Reynolds condition, leading to a larger GCM wake. The velocities from $10\ m/s$ to $20\ m/s$ are relatively close to each other, with the increase in velocity leading to a drag area reduction at each crosswind angle. With negative angles being considerably closer than the positive angles, again showing that the lower leg position influences the drag area. Furthermore, $25\ m/s$ at low crosswind angles, between $-6°$ and $8°$, shows a step in the reduction of the drag area.

The crosswind-C_DA curves of all the velocities display a rather symmetric behaviour. With noticeable drag reductions as the crosswind increases. This is significantly different for the Asymmetrical GCM, see Figure 4.24b. In the Asymmetric GCM case, the drag area seems unaffected at high negative crosswind angles, meaning that altering the angle does not result in a drag area change. This is linked to the extended leg of the Asymmetric GCM being in the oncoming airflow at negative angles. The bent leg, positive angles, of the Asymmetric GCM, exhibit the same behaviour as the Symmetric GCM. Considering that the bent leg of the Asymmetric GCM is quite similar to the legs of the Symmetric GCM, it is logical that a decreasing drag area trend is seen in both the positive and negative crosswind angles of the Symmetric GCM.
Another difference in the crosswind effect of the Symmetric and Asymmetric GCM is the comparison between the positive and negative angles. The negative crosswind angle yields a lower drag area than its corresponding positive angle for the Symmetric GCM, in almost all cases. For example, at $-10°$ to $10°$ at $14\ m/s$, the $-10°$ case has a further drag area reduction of 6%. The Asymmetric GCM has the opposite behaviour, where the positive crosswind angles lead to a lower drag area than its

corresponding negative yaw angle. This happens in the cases where the crosswind is larger than $\pm 5°$. For example, $-10°$ to $10°$ at $14\ m/s$, the $-10°$ results in a further drag area reduction of 9%.

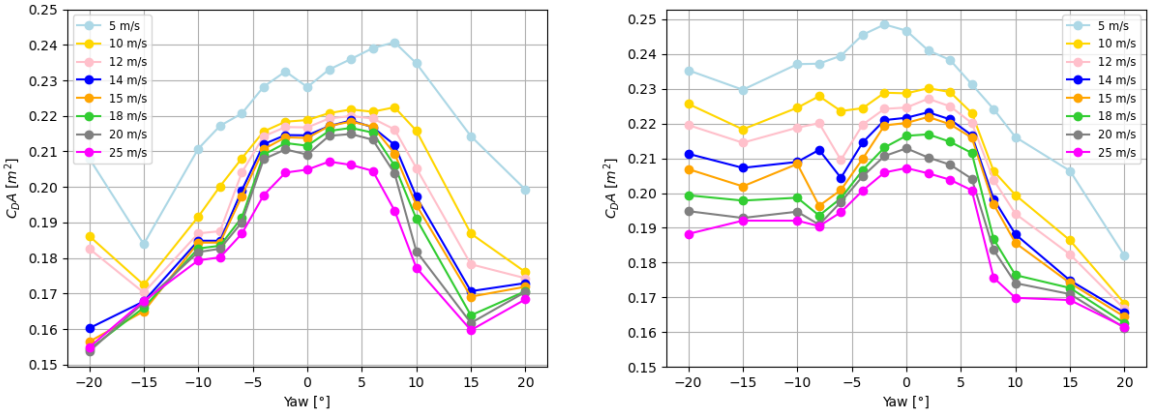

(a) Symmetric GCM

(b) Asymmetric GCM*

Figure 4.24: The effect of crosswind angles on the drag area of the Symmetric GCM and Asymmetric GCM at different velocities

* Data taken from Maleki Dastjerdi et al. 2025 [16]

4.3.2. Aerodynamic Flow Field

After all corrections mentioned in section 3.7 have been applied, the flow field can be investigated. Note, the rotation of the flow field leads to a reduction of data on the side pointed towards the airflow. The reduction is outside of the wake of the GCM; therefore, it does not interfere with the comparisons and conclusions.

The normalised streamwise velocity at $14\ m/s$ at the crosswind angle extremes, $-8°$ and $8°$ is shown in Figure 4.25 and compared to the flow field at $0°$.
The upper part of the wake of the Symmetric GCM has a tilting behaviour when placed at crosswind angles, and loses its symmetrical shape. The shoulder pointed into the oncoming airflow generates a higher wake, while the other shoulder generates a lower wake. Meaning, at $-8°$ the left shoulder is placed into the airflow and generates a higher (larger) wake. This behaviour is in line with the lateral and vertical velocity flow fields, see in Appendix D, D.2. At $-8°$, the lateral flow shows that most of the airflow is going from right to left, while at $8°$ the flow is mostly going from left to right. The compression visible behind the hips at $0°$, is moved with the lateral flow under the crosswind, i.e. the compression is moved towards the right at positive angles. This flow change is also visible in the direction of the downwash, where at $-8°$ the downwash has a tilt to the left (from right to left). Furthermore, the (maximum) magnitude of the downwash is reduced under crosswind angles. Next to this, the side pointed into the airflow experiences upwash, the other side experiences a downwash at $-8°$, while at $8°$ there is a slight upwash. The tilt in the downwash over the back of the GCM can be linked to the movement of the shoulder wake. The combination of the tilt and the crosswind shows an effect in the low velocity area. This region, $w/U_\infty \approx 0.15$, becomes larger under negative crosswind, while it is not present at the positive angle.

The left leg wake shows the effects of the crosswind. The left leg has a lower velocity ($w/U_\infty \approx 0.75$) near the knees, connecting the upper and lower parts of the wake. This wake is moved towards the right at a positive crosswind angle, as the right leg is pointed into the airflow. At $-8°$ the connection is not present, left leg pointed towards the airflow, due to the leg being straighter, the wake is able to recover faster.
The velocity in the wake of the calf is higher at negative crosswind compared to $0°$ and $8°$. Comparing the positive angle to the no crosswind condition, the velocity is slightly higher. This is caused at the right leg is blocking the airflow for the left, leading to the wake being more compressed. However, the full effect of crosswind on the legs cannot be analysed due the the missing data surrounding the right leg.

The aerodynamic loads indicate that the Symmetric GCM at $0°$ has the highest drag area, with $-8°$ having a drag area reduction of 14% and $8°$ having a reduction of 1.3%. Meaning that there is a 13% difference between $-8°$ and $8°$. Based on the aerodynamic flow fields of the streamwise velocity, the upper wake at $8°$ is generating less drag, while $8°$ is generating the most. However, this is the opposite as observed in the loads. From this, a conclusion can be drawn that the wake of the legs has a large influence of the drag area of the cyclist, as the theory mentioned in the Reynolds number effect. It might even be greater than the upper wake; however, due to the lack of data of the right leg, a definite conclusion cannot be made.

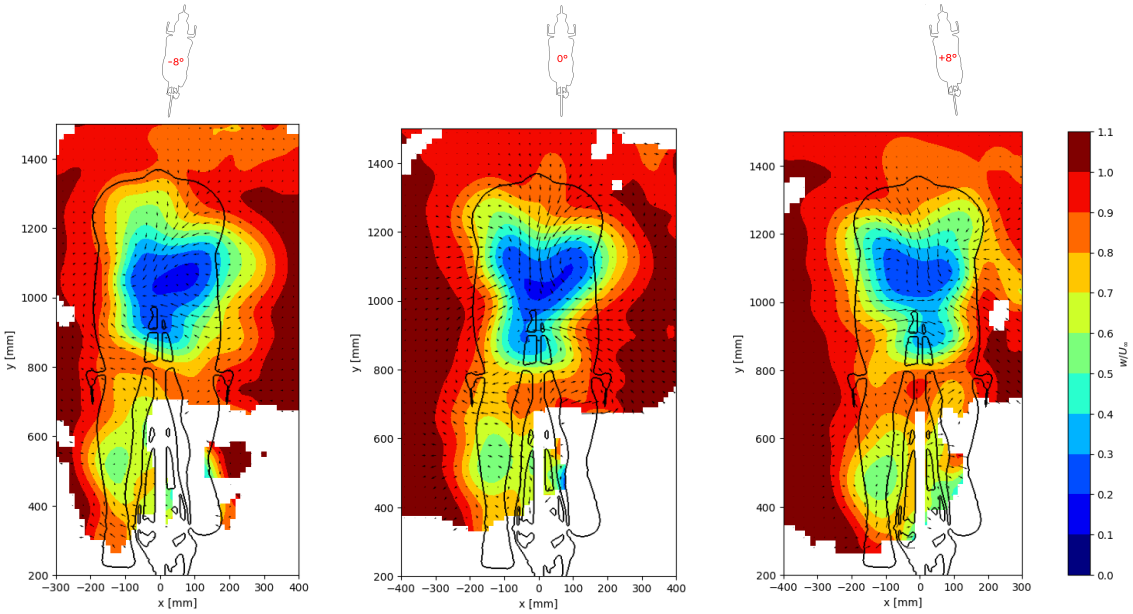

(a) $-8°$ **(b)** $0°$ **(c)** $+8°$

Figure 4.25: The velocity flow field of the Symmetric GCM at $-8°$, $0°$ and $8°$ crosswind angles at $14\ m/s$

The crosswind angles above, $-8°$ and $8°$, are at the ends of the crosswind range. In Figure 4.26, the angles in between are visualised. As can be seen, the flow field is different at each angle, but keep a similar trend. The drag area change for the angles $-6°$, $-4°$, $4°$ and $6°$ are -7.2%, -1.1%, 1.9% and 1.0%, respectively. This means that both negative angles lead to a drag reduction while the positive angles lead to a small increase compared to the $0°$ case.

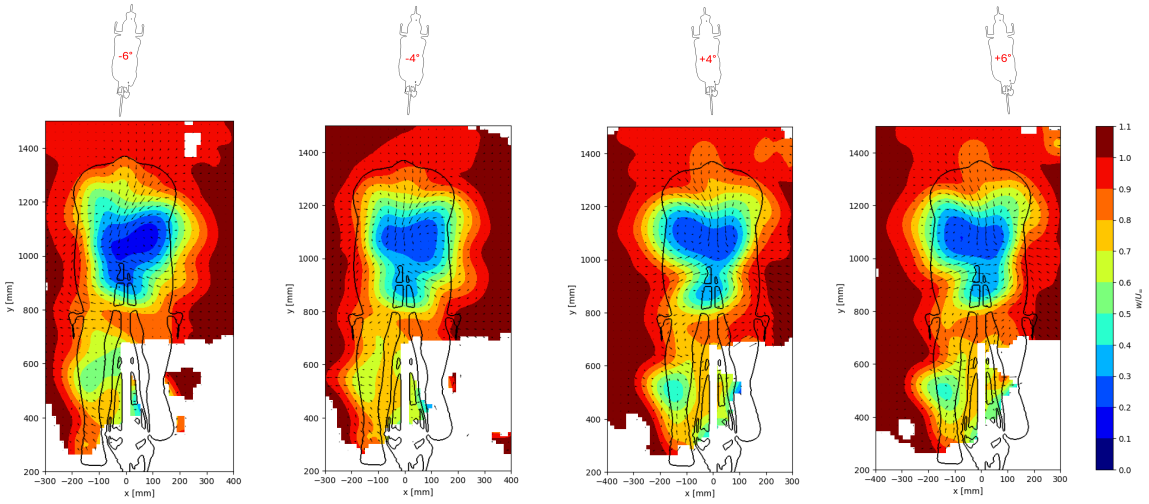

Figure 4.26: The velocity flow field of the Symmetric GCM at $-6°$, $-4°$, $4°$ and $6°$ crosswind angles at $14\ m/s$

As mentioned, due to the crosswind, the lateral and vertical velocity behaviour has changed, which is connected to the change in vorticity. The vorticity fields of the Symmetric GCM at $-8°$, $0°$ and $8°$ are given in Figure 4.27. As seen, the vortices have been altered when the cyclist experiences crosswind. The clockwise-rotating (CR) vortices (indicated in blue) in the upper region have increased in strength at negative crosswind, and are less combined than at $0°$. The two CCR vortices (red) remain unchanged in their position and maximum magnitude. When analysing the positive crosswind angle, $8°$, a distinct difference is spotted. The left lower hip vortex was a CR vortex at $0°$, as well as $-8°$, has become a CCR vortex, caused by the change in vertical velocity direction, where the upwash on the left side has lost its strength at $8°$. This CCR vortex combines with the right upper and lower hip vortices into one large CCR vortex. This behaviour was spotted with the CR vortices at $0°$ and $-8°$. Next to this, the two CCR on the right have decreased in size under the crosswind angle, this is as more freestream airflow can reach this area. The two CR vortices on the left at $8°$, have increased in magnitude compared to $0°$, yet are still weaker than at $-8°$. Moreover, the shape of the vortices has changed, and the position is altered, slightly moved to the right.
At $0°$, the inner thigh CCR vortex is combined with a CCR vortex stemming from the right knee; this vortex has changed directions, changes to a CR vortex, under both positive and negative crosswind angles.

The lower part of the vorticity flow field shows changes to the rotation of the airflow, as the negative angle strengthens the CR airflow while the positive angle strengthens the CCR flow.

Similar to the velocity flow fields, the connection between the drag area and the vorticity flow fields does not show a direct conclusion. The upper part of the vorticity is higher in (absolute) magnitudes for the $-8°$ case, while it shows the drag reduction of 14% compared to $0°$. Furthermore, as the vorticity has changed directions at the $8°$ case, the conclusion surrounding the upper part with respect to the drag area is inconclusive.
This indicates that the vorticity of the legs has a greater part in the drag of the GCM than the wake of the body.

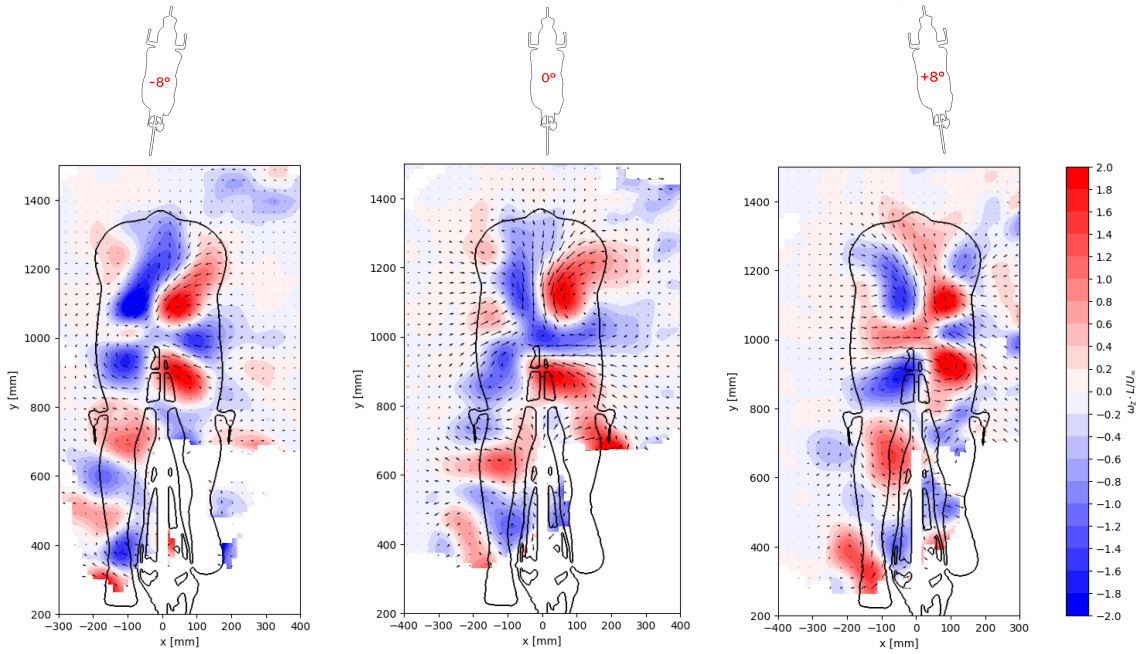

(a) $-8°$ **(b)** $0°$ **(c)** $+8°$

Figure 4.27: The vorticity flow field of the Symmetric GCM at $-8°$, $0°$ and $8°$ crosswind angles at $14\ m/s$

As discussed, the strength of the vortices has been changed, and for clarity has been visualised in Figure 4.28. The vortices at $-8°$ are stronger then at the other crosswind angles, and indicate that the right upper hip vortex its much larger than visualised in the vorticity flow fields. The $8°$ case shows four distinct vortices in the upper region, while that is less the case for the other angles.

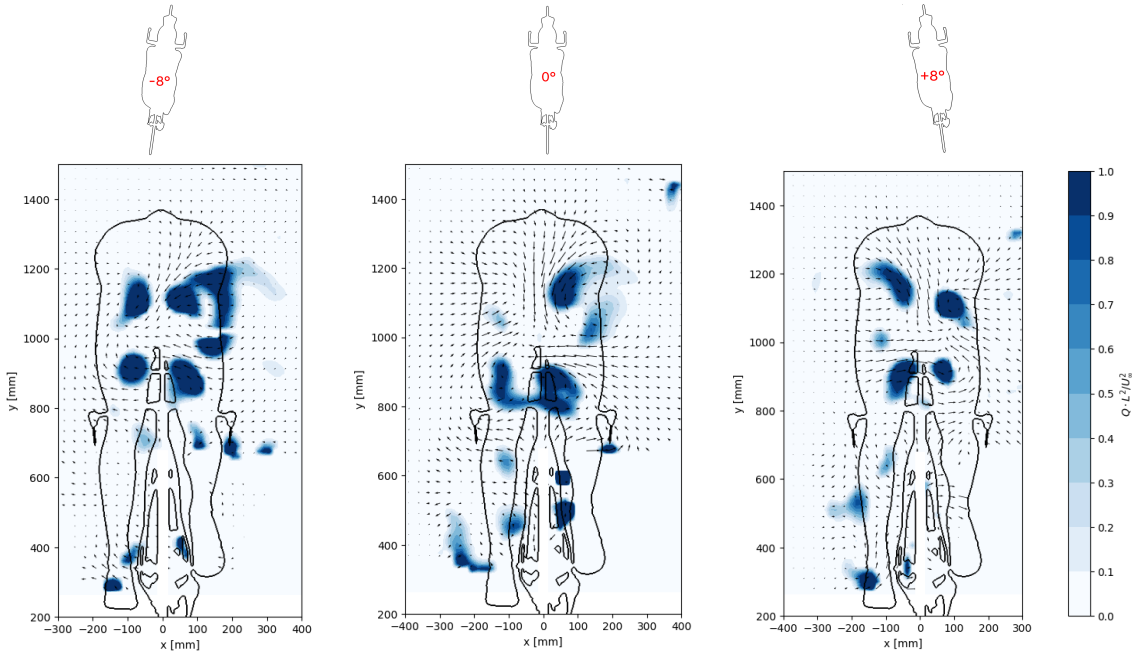

(a) $-8°$ **(b)** $0°$ **(c)** $+8°$

Figure 4.28: The Q-criterion of the Symmetric GCM at $-8°$, $0°$ and $8°$ crosswind angles at $14\ m/s$

The vorticity flow field and Q-criterion of the crosswind angles $\pm 4°$ and $\pm 6°$ are given in Appendix D, D.2. These are in line with the behaviours spotted in the $-8°$ and $8°$ cases.

4.3.2.1. Influence of Reynolds Number on the Crosswind Effect

The aerodynamic flow field is altered by the introduction of crosswind and Reynolds number. The combination of the two has been analysed by testing the angles $-8°$ and $8°$ at the velocities $10\ m/s$ and $18\ m/s$.

The cross-comparison can be seen in Figure 4.29. The $10\ m/s$ cases show differences in behaviours compared to the $14\ m/s$ cases. At $-8°$ at $10\ m/s$, the wake has become much smaller while keeping the wake tilt. However, investigating the standard deviation shows that the upper region, the area where the wake has been reduced, has a larger deviation, with the uncertainty of 40% up to 50%. As the uncertainty is high, the comparison between the $-8°$ and $0°$ case is inaccurate. The accuracy for the other cases are higher, and thus comparisons can be made.
The $10\ m/s,\ 8°$ case, shows the same behaviour as the $14\ m/s$ case, with a shift in the wake, a higher right shoulder wake.
The $18\ m/s$ cases have a very similar behaviour to the $14\ m/s$ case, with the shoulder wake increasing when pointed into the airflow. Furthermore, the lowest velocity region at $0°$ is increased at $8°$, as well as a movement in the wake behind the hips.

It was calculated that the step from $0°$ to $-8°$ at $14\ m/s$ leads to a drag reduction of 14% and the step to $8°$ (from $0°$) leads to a 1.3% decrease in drag area. For comparisons, at $10\ m/s$, the drag area is reduced by 8.5% at $-8°$ and increased by 1.6%. Similarly, at $18\ m/s$, the drag reduction is 13% and 2.6% respectively. This states that the $14\ m/s$ and $18\ m/s$ cases behave similarly. On the contrary, at $10\ m/s$, the positive crosswind results in an increase in drag area. The main difference in the flow fields of $0°$ and $8°$ at $10\ m/s$ is the left leg wake, which becomes larger under the crosswind angle.
As mentioned before, it is considered that the leg wake has a greater role in the drag area of the cyclist than the upper wake. The changes in the flow field of the $10\ m/s,\ 8°$ case supports this, as the increase in leg wake affects the drag more than the upper wake decrease.

Two things can be concluded from the aerodynamic flow fields surrounding the cross-comparison. First, the effect the crosswind has on the aerodynamic flow field is unaffected at different Reynolds numbers.

Meaning that the Reynolds effect and crosswind effect do not interfere with each other. Secondly, the leg wake has a predominant impact on the drag area.

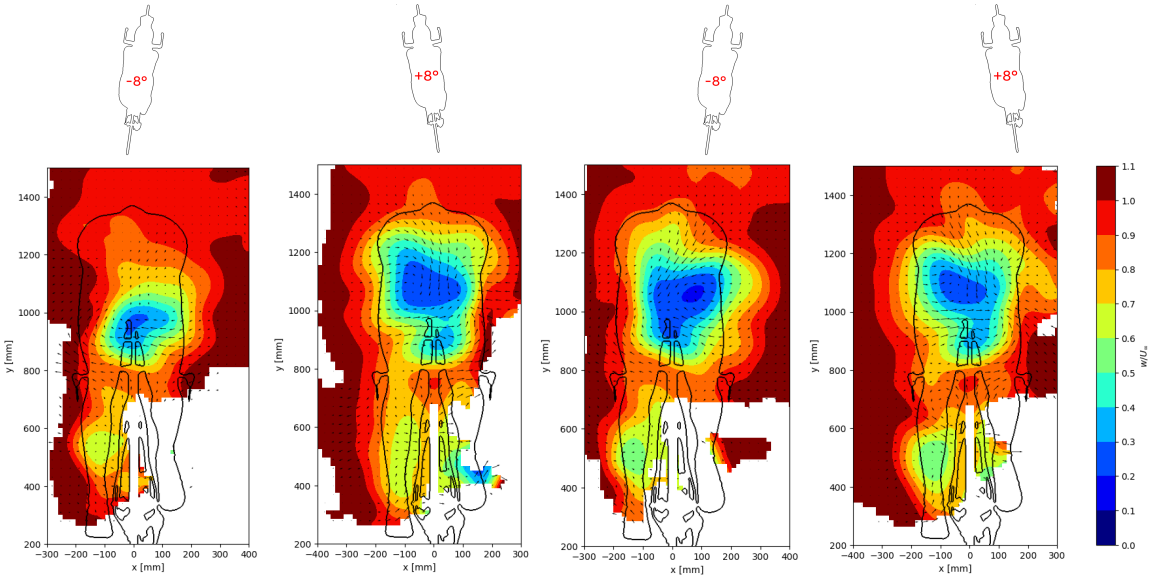

(a) $10\ m/s$ - $-8°$ **(b)** $10\ m/s$ - $+8°$ **(c)** $18\ m/s$ - $-8°$ **(d)** $18\ m/s$ - $+8°$

Figure 4.29: The velocity flow field of the Symmetric GCM at the velocities $10\ m/s$ and $18\ m/s$ and the crosswind angles $-8°$ and $8°$

The vorticity at the velocities $10\ m/s$ and $18\ m/s$ are given in Figure 4.30. The $8°$ vorticity fields demonstrate the same vorticity field as the $14\ m/s$ case, indicating that the velocity does not change the shift caused by the crosswind. They display that the left lower hip vortices turn into a CCR vortex while it has a clockwise rotation at $0°$. Next to this, the $18\ m/s,\ -8°$ case responds as the $14\ m/s$ case, with the two left CR vortices becoming stronger.
The $10\ m/s,\ -8°$ case is not taken into account due to the high uncertainty.

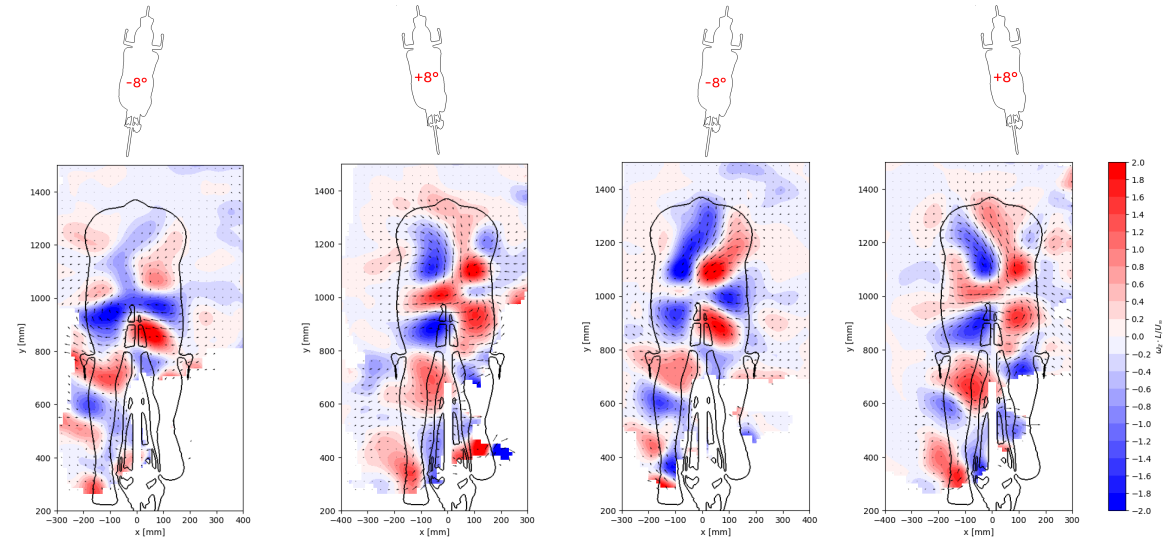

(a) $10\ m/s$ - $-8°$ **(b)** $10\ m/s$ - $+8°$ **(c)** $18\ m/s$ - $-8°$ **(d)** $18\ m/s$ - $+8°$

Figure 4.30: The vorticity flow field of the Symmetric GCM at the velocities $10\ m/s$ and $18\ m/s$ and the crosswind angles $-8°$ and $8°$

4.3.2.2. Comparison to Asymmetric GCM

To understand the behaviour caused by the crosswind effect, it has been tested on the Asymmetric GCM, and displayed in Figure 4.31.
The upper wake of the Asymmetric GCM at $-8°$ has a bigger effect than seen in the Symmetric case. This is caused by the strength of the inwash from the right side, see Appendix D, D.2.1. Due to this, the downwash is acting under a greater tilt than seen at the Symmetric GCM. This combination leads to the bigger effect seen in the upper wake. Looking into the $8°$ case, the inwash from both sides has been magnified in strength; due to this, the downwash does not have a tilt. This behaviour is different for the Symmetric GCM, where the downwash has a tilt to the left. Since the downwash and inwash stay at the same position at the $0°$ case, the upper wake is not tilted, but more rounded.

The left leg wake is more difficult to analyse as the $-8°$ case is missing data near the lower part of the legs. However, from the small part that is visible, it can be seen that the wake is larger and has a lower velocity. The left leg wake at $8°$ is smaller than the $0°$.

The Asymmetric GCM has a drag reduction of 4% at $-8°$, while a 11% reduction is seen in the $8°$ case. Comparing back to the Symmetric GCM, where the drag area is reduced by 14% and 1.3%, respectively. The main difference in the behaviours of the crosswind effect is spotted at the legs. Where the Symmetric GCM shows a small wake reduction at both crosswind angles, the Asymmetric GCM only shows the reduction at $8°$. This aligns with the theory that the leg wake has a significant influence on the drag area of the cyclists in both the symmetrical and asymmetric positions.
This comparison of the crosswind effect shows the importance of the leg position of the GCM.

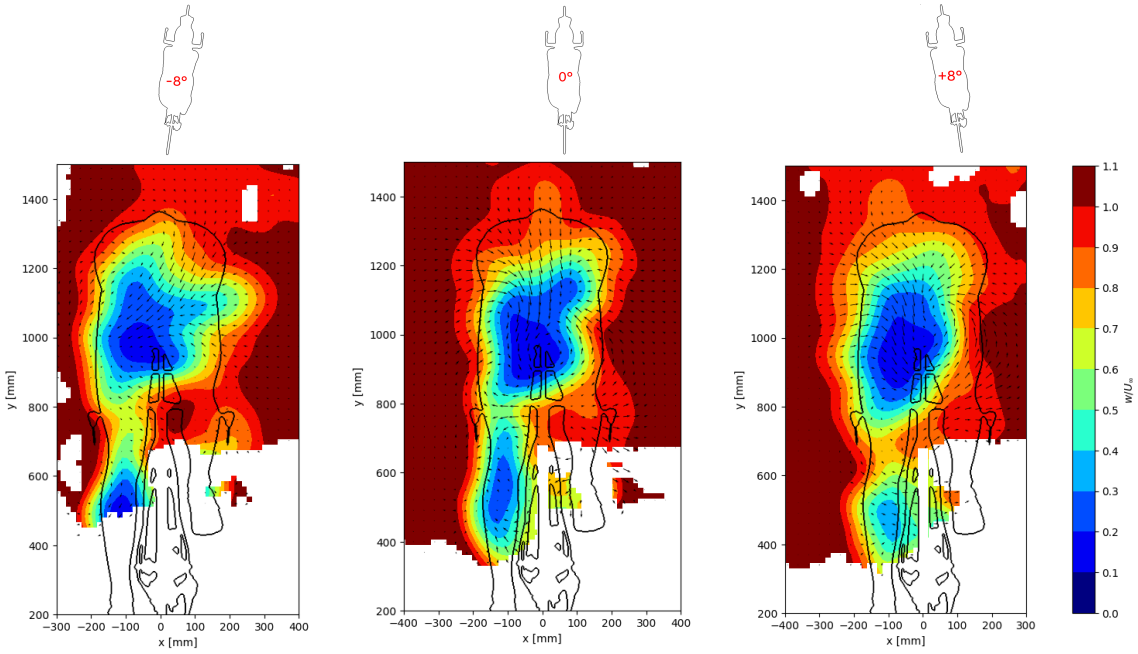

(a) $-8°$ **(b)** $0°$ **(c)** $+8°$

Figure 4.31: The velocity flow field of the Asymmetric GCM at $-8°$, $0°$ and $8°$ crosswind angles at $14\ m/s$

The vorticity flow field of the crosswind effect on the Asymmetric GCM is given in Figure 4.32. The changes to the vorticity flow field due to the crosswind of the Asymmetric GCM are the same as for the Symmetric GCM. At the $-8°$ case, the upper clockwise rotating vortices have increased in strength and moved into a tilted position. At $8°$, the CR vortices are moved towards the left, and two CCR vortices on the right side have combined, similarly to the Symmetric GCM.

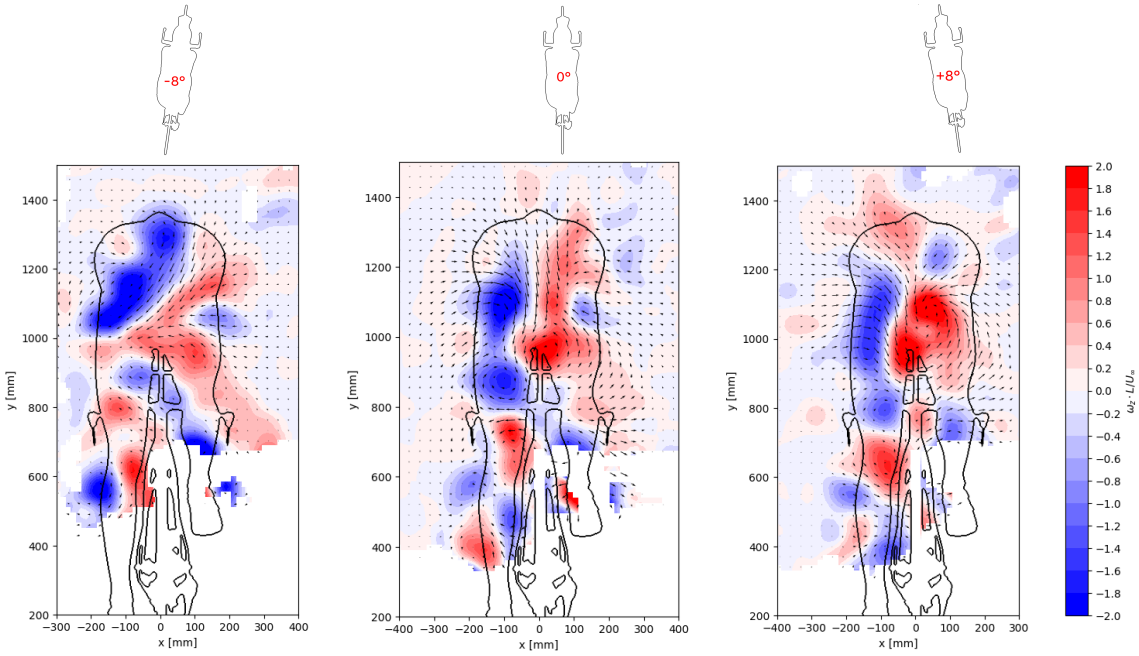

(a) $-8°$ **(b)** $0°$ **(c)** $+8°$

Figure 4.32: The vorticity flow field of the Asymmetric GCM at $-8°$, $0°$ and $8°$ crosswind angles at $14\ m/s$

The effect of crosswind on the Reynolds number has been tested on the Asymmetric GCM, and given in Appendix D, D.2.2. The velocity and vorticity flow field of the $10\ m/s$ and $18\ m/s$ case, shows the same behavioural changes caused by the crosswind effect as the $14\ m/s$ case.

4.3.3. Conclusion

The aerodynamics of the cyclist are altered when placed under a crosswind. Rotating the GCM with the straighter leg (left leg) into the oncoming airflow leads to a drag area reduction. When rotating the cyclist the other way, the bent leg (right leg) is into the airflow, small crosswind angles lead to a drag area increase, while large angles lead to a drag reduction. The crosswind effect is present at each Reynolds number, and the increase in Reynolds number leads to the peak drag area being moved closer to $0°$. The difference in drag area between the negative and positive crosswind areas is related to the leg position. The bent leg and straight leg have a difference response when placed into the oncoming airflow.
The difference in leg position becomes visible when compared to the Asymmetric GCM. The asymmetric bent leg has the same response as the symmetric bent leg. The asymmetric straight leg performs different, as a crosswind angle larger than $-8°$ leads to a converged value. The Symmetric GCM does not show this convergence as it reduces the drag area while the crosswind angle is increased.
The drag area response of the crosswind effect shows the importances of the leg position.

The aerodynamic flow field at the crosswind angles $-8°$ and $8°$ shows that at $14\ m/s$ the upper wake and lower wake are altered. For the upper wake, the minimal velocity in the wake is increased at $8°$. Next to this, the wake shows a shift at the shoulders, where the shoulder pointed towards the airflow has a larger (or higher) wake. At $8°$ the upper wake becomes less compressed and has a larger region of low velocity airflow. Next this, the vortices generated from the hips and thighs are altered. The clockwise rotating vortices from the upper and lower left hip are increased in strength when the airflow is coming from the left ($-8°$). Subsequently, when airflow comes from the right ($8°$), the CCR vortices stemming from the right upper hip and right inner thigh increase in strength. In this situation, the rotation of the vortex generated by the left lower hip is changed to a CCR vortex, and it combines with the upper right hip vortex and the vortex from the tights. From this, it can be concluded that crosswind alters the aerodynamics of body the GCM.
Consequently, the crosswind alters the legs' wakes, with the $8°$ case yielding a smaller left-leg wake and a smaller low-velocity region. The negative rotation, $-8°$, the left leg wake yields the smaller low

velocity region, with a more elongated wake. The vorticity from the legs has a similar behaviour as the upper wake, where a $-8°$ crosswind strengthens the CR vortices and the $8°$ crosswind strengthens the CCR vortices.

Combining the altered flow fields with the aerodynamic loads, it can be concluded that a negative rotation, rotating the straighter leg into the airflow, leads to a larger drag reduction, indicating that the position of the legs is of importance under crosswind. Demonstrating that the wake of the legs plays a greater part in the drag area of the cyclist than the upper body.

The effect of crosswind on the aerodynamic flow fields is tested at different Reynolds numbers to investigate the combination of crosswind and Reynolds number effect. It was seen that the crosswind effect at $18\ m/s$, results in the same behaviours in terms of wake and vorticity as at the reference velocity. Similarly, the $10\ m/s$ case is analysed, but due to the high uncertainty, it is not taken into account for the conclusions.

Furthermore, the crosswind effect is tested on the Asymmetric GCM to analyse whether the same behavioural changes are spotted. The crosswind effect on the upper wake resembles the behaviour of the Symmetric GCM, however, the changes are larger, with the $-8°$ case having a bigger tilt, while the $8°$ case leads to a more rounded wake. The biggest difference in behaviour is located in the legs. Where the $-8°$ case for the Symmetric GCM leads to the lowest drag area (of the three presented cases) and has a smaller wake than the $0°$ case, the Asymmetric case shows a larger leg wake (lower velocity) at $-8°$ than at $0°$. Unfortunately, not all of the left leg wakes have been visualised due to the lack of data, thus no definite conclusion can be drawn. The $8°$ crosswind on the Asymmetric GCM shows a smaller left leg wake in response to the drag area decrease. The Asymmetric GCM confirms the theory that the wake caused by the legs is more influential in the total drag area than the upper wake.

4.4. Passive Aerodynamic Devices

An attempt is made to reduce the drag area and wake of the Symmetric GCM by placing passive aerodynamic devices on the hips, arms or legs. The placement of the devices on the hips is dependent on the location of the hip separation, whereas the devices on the arms and legs have a predetermined position. To quantify the effect of said devices, they are compared to the configuration without any devices; bare configuration. For all devices, the aerodynamic loads are measured, and in case of a drag area reduction, PIV measurements are taken.

4.4.1. Devices on the Hips

Vortex generators are placed on the hips of the Symmetric GCM to try to reduce the drag area by lessening the wake width. The position of the vortex generator depends on the separation of the airflow around the hips. The separation line is visualised using oil flow visualisation, and is given in Figure 4.33. At $14\ m/s$, the front of the upper leg shows a clear attachment as seen by the streamlines. On the side of the cyclist's stomach shows some signs of attachment; however, the oil dots on the model indicate the oil was not properly applied, or the airflow is not attached. The oil demonstrates separation on the rearward part of the upper leg and the hip. This is because the oil flow has a downwards movement, due to gravity, and does not show any streamlines. The separation line on the hip is visible, whereas it is less clear on the leg. The separation lines from the two velocities are overlaid and placed on the CAD of the Symmetric GCM, Figure 4.33c, to show the movement. The movement is relatively small, but in line with expectations. The Reynolds number effect, section 4.2, showed that at higher velocities, the drag area is reduced; this was linked to the critical Reynolds number phenomenon. Based on this phenomenon, it would mean that the separation of a bluff body is postponed. In the CAD drawing, this can be seen as the separation line near the hip is more downstream/rearward for the $18\ m/s$ case. The upper leg separation line does not have a movement in location; however, at $18\ m/s$ it is more visible.

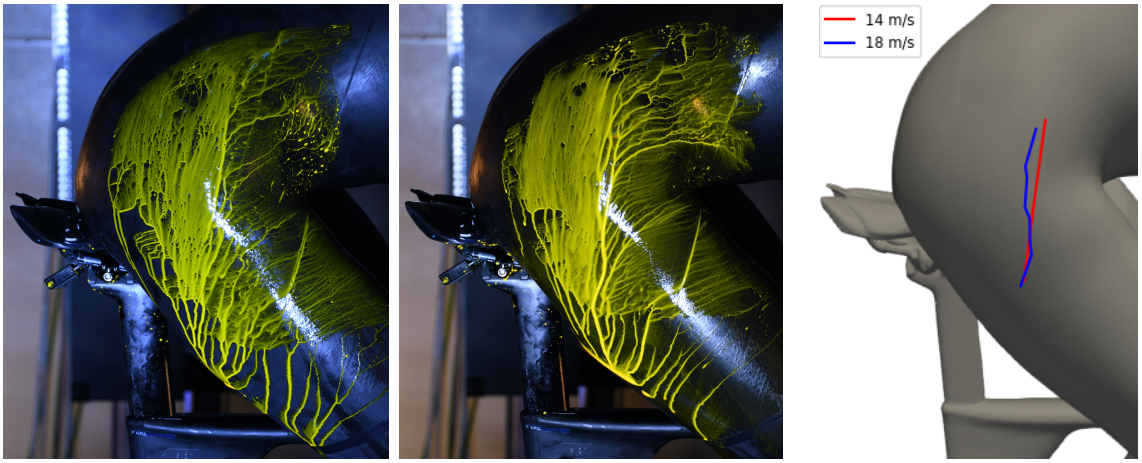

(a) $14\ m/s$ **(b)** $18\ m/s$ **(c)** Separation line in CAD*

Figure 4.33: Oil flow visualisation on the hip of the Symmetric GCM at $10\ m/s$ and $18\ m/s$
* Note, the accuracy in CAD of the locations is not 100%. This is only to show the placement relative to each other.

Based on the separation line at $14\ m/s$, the locations of the leading edge of the vortex generator strips is placed. The leading edge of the strip is placed $10 \cdot h$, (ten times the height of the VG) upstream of the separation line. As the oil has to be removed before any VGs can be placed, a marker was placed on the GCM at the separation. From this marker, the locations were determined by measuring the distance upstream of the marker. Figure 4.34 shows the placement of the VG strips on the GCM, as well as the relative placement on the CAD. Based on the CAD, Figure 4.34d, it can be seen that the VG - 1.0δ was not placed at its preferred location, as it has a slight tilt. As the measuring and placement were done by hand with only the marker as a reference, this was likely to occur. The placements of the VG 0.5δ and 1.5δ are at the right locations.

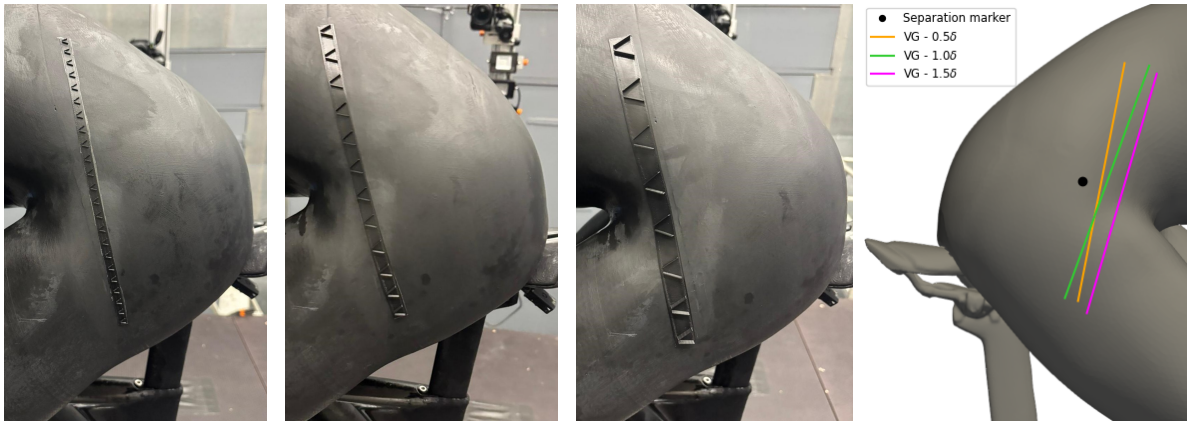

(a) VG-0.5δ on the model **(b)** VG-1.0δ on the model **(c)** VG-1.5δ on the model **(d)** VG leading edge location*

Figure 4.34: The vortex generator positions on the GCM
* Note, the accuracy of the locations is not 100%. This is only to show the placement relative to each other.

The drag area of the GCM with vortex generators are plotted against air speed in Figure 4.35. The VGs increase the drag area of the cyclist by 2% to 5%. The 0.5δ and 1.0δ have a very similar drag area, which is likely due to the placement of the 1.0δ on the GCM, since it is tilted. The biggest VG, VG-1.5δ, results in the highest drag area, which can be explained by more forward placement than the other strips.

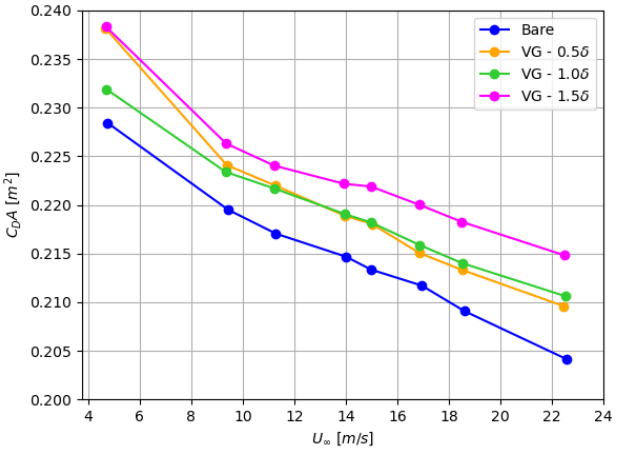

Figure 4.35: Effect of adding vortex generator strips on the hips of the Symmetric GCM

All VGs are placed upstream of the separation line; however, the drag area increase likely indicates that the strips are placed to upstream. For this reason, the VG-1.5δ is tested at two different downstream locations. The first position was on the separation marker itself, about $4\ cm$ rearward of the original position, whereas the second position was placed about $3\ cm$ behind the first but shows a curvature due to the rounding of the hip. In Figure 4.36a, the downstream placement of the two options is shown on the CAD. The downstream movement results in a decrease in the drag area of the GCM compared to the original location, as can be seen in Figure 4.36b. The second option, furthest downstream, still results in a higher drag area than the bare configuration.

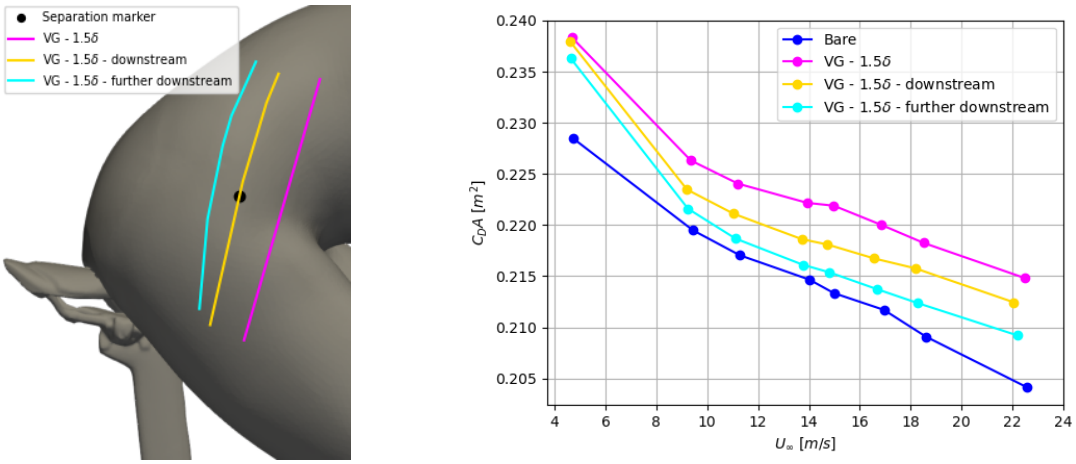

(a) VG leading edge location*

(b) Effect on drag area

Figure 4.36: Placement and effect of placing VG-1.5δ downstream on the hip of the Symmetric GCM
* Note, the accuracy of the locations is not 100%. This is only to show the placement relative to each other.

Based on the above-mentioned results, the vortex generators have a negative effect on the drag area. Perhaps an even further downstream placement can have a neutral to positive effect, which would indicate that the current placement lies in a fully attached region that is triggered into an earlier separation.

4.4.2. Devices on the Arms

On the upper arms of the Symmetric GCM, zigzag strips are placed to try to reduce the drag area. The zigzag strip triggers the transition of laminar airflow when placed on the surface of a bluff body. As the arms are assumed to be in laminar airflow, the prediction is that the zigzag strip reduces the drag area.

In Figure 4.37, the drag area of the zigzag strip and the bare configuration are plotted against air speed. It can be seen that the zigzag strip leads to a reduction in drag area at each velocity. At lower velocities,

the reduction is around 5%, while at the highest velocity, the reduction is lower than 2%. This falls in line with the experiment on bluff bodies, where the zigzag strip converges as the velocity increases, and thus shows a greater effectiveness at lower velocities [28]. In the case of the arms, the effectiveness become lower, but a convergence has not been reached yet, meaning the drag area is still Reynolds number dependent.

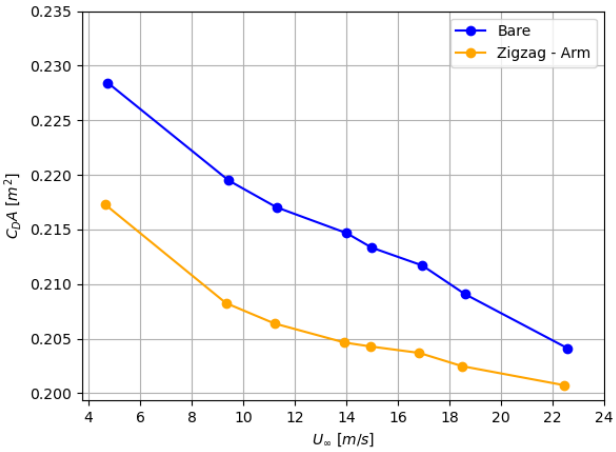

Figure 4.37: Effect of adding a zigzag strip to the upper arms of the Symmetric GCM

The effect of the zigzag strip on the arms is tested at different crosswind angles, $-8°$ and $8°$, and plotted in Figure 4.38. At $-8°$, the zigzag strip does not seem to influence the drag area, except at $10\ m/s$, which is likely an error in the measurements rather than an actual effect of the zigzag strip. On the contrary, at $8°$ the zigzag strip reduces the drag area at almost all velocities. On average, between $10\ m/s$ and $20\ m/s$, the drag area is reduced by 4.5%, which is a similar reduction to that at $0°$.

The reason for the difference in effectiveness at negative and positive crosswind angles is presumably the position of the legs. The forward leg, the straightest, is turned towards the oncoming air flow at negative angles, while the bent leg is turned away. Based on the two crosswind graphs, it can be gathered that a change in the wake of the arms has little to no effect on the wake of the straightest leg. This means that the wake caused by the straightest leg/hip of the cyclist is more predominant in the total wake and drag area than the influence of the arm wake.

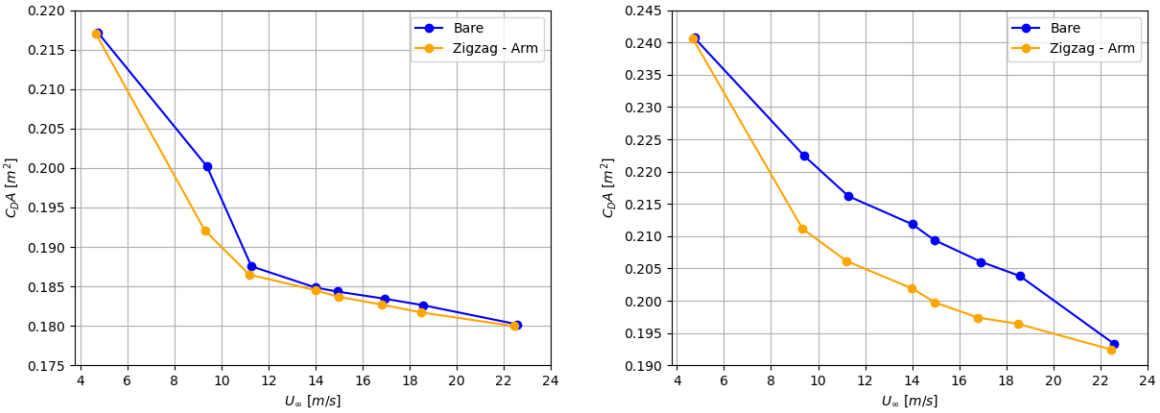

(a) Crosswind $-8°$

(b) Crosswind $8°$

Figure 4.38: Effect of adding a zigzag strip to the upper arms of the Symmetric GCM at crosswind angles

4.4.2.1. Aerodynamic Flow Field

A drag area reduction of 4.7% is seen when zigzag strips are placed on the arms of the Symmetric GCM. The zigzag strip is predicted to trigger a transition and alter the wake of the arms. The wake of the arms affects the airflow the body experiences, and thus alters the wake of the body. To understand the intersection of the arm wake with the body wake, the flow field behind the saddle is analysed, and visualised in Figure 4.39. Note, the effect on the arm wake has not been measured, and only the effect of the wake change on the cyclist's body is visualised, which gives an indirect view of the zigzag effect.

Small changes are seen in the upper wake of the body. The addition of the zigzag device leads to a slightly smaller wake, seen in the contour, which is in line with the expectation due to the drag reduction. Next to this, the velocity within the upper wake has been lowered and less compressed. The comparison in lateral velocity, Appendix E, E.1, shows that the inwash from the right side has been reduced in area and the magnitude has been lowered. In connection with this, the inwash from the left side of the GCM is increased in size, however, also reduced in magnitude. Although the strength has lessened, the wake of the GCM is smaller. It is likely that less 'strength' is required due to the wake behind smaller, rather than needing the strength of the lateral velocity to make the wake smaller. The vertical velocity flow fields show no changes in the upper wake, which is as expected since the downwash over the back should not be affected by the arms.
The flow field of the upper wake does not show the reason for the drag reduction. It may be that the pressure in front of the body, caused by the wakes of the arms, is altered, and the pressure difference is a result of the drag area reduction. However, this is difficult to visualise.

The lower part of the legs shows a difference in the wake. It could be that the airflow change from the wake of the arms is altering the wake for the upper left leg, which in turn can alter the wake of the lower left leg. However, it is also likely that the differences are caused by the uncertainty.

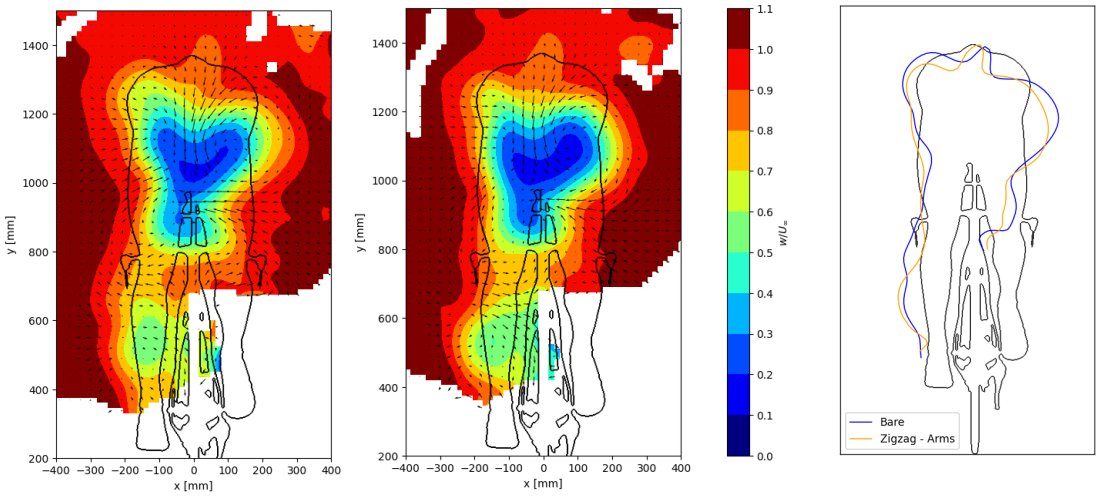

(a) Bare configuration **(b)** Zigzag on arms **(c)** Contour at $w/U_\infty \approx 0.85$

Figure 4.39: The effect of zigzag strips on the arms of the Symmetric GCM on the velocity flow field at $14\ m/s$

The vortices stemming from the hips are altered by the flow control devices on the arms. Figure 4.40 shows that the left lower hip vortex has been reduced in strength. Due to this, the combined CR vortex has been altered, with the left upper hip vortex being increased in strength and moved towards the left. Similarly, the right lower hip vortex is moved towards the right. Furthermore, the counter-clockwise rotating vortex stemming from the right upper hip has become larger and stronger. The other CCR vortex is generated by the inner thighs; this vortex is more compressed and centred due to the addition of the zigzag strips. The inner thigh vortex is altered as the airflow reaches the body (belly of the cyclist), which has been changed due to the device.

The vorticity surrounding the legs shows differences due to the flow control devices. However, as mentioned before, it is difficult to say with certainty whether it has been caused by the zigzag strip.

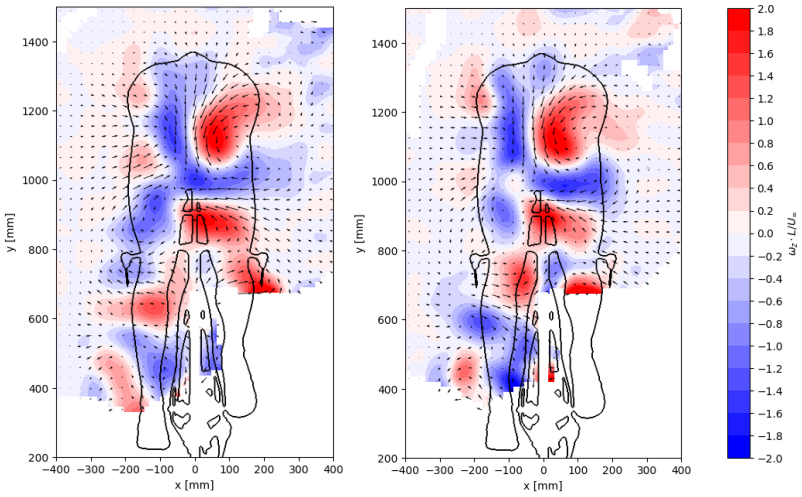

(a) Bare configuration **(b)** Zigzag on arms

Figure 4.40: The effect of zigzag strips on the arms of the Symmetric GCM on the vorticity flow field at $14\ m/s$

4.4.2.1.1. Reynolds Number Effect

To understand the difference the velocity has caused on the drag area, the flow field is visualised at $18\ m/s$. At this velocity, the drag reduction is less than the reference velocity, around 3.8%.

The flow field is given in Figure 4.41 and shows a different response than the reference velocity. The velocity in the upper wake is increased by the addition of the flow control devices, while it was lowered at the $14\ m/s$ case. However, the lateral velocity changes are as the reference velocity case, with the inwash from the right side being reduced in size and the inwash from the left side being larger.
The wake size of the GCM is not changed by the addition of the flow control devices, a difference from the $14\ m/s$ case.

Due to the differences in the behaviours of the addition of the zigzag strip on the arms at $14\ m/s$ and $18\ m/s$. The reason for the drag area reduction cannot been tied to a flow field change.

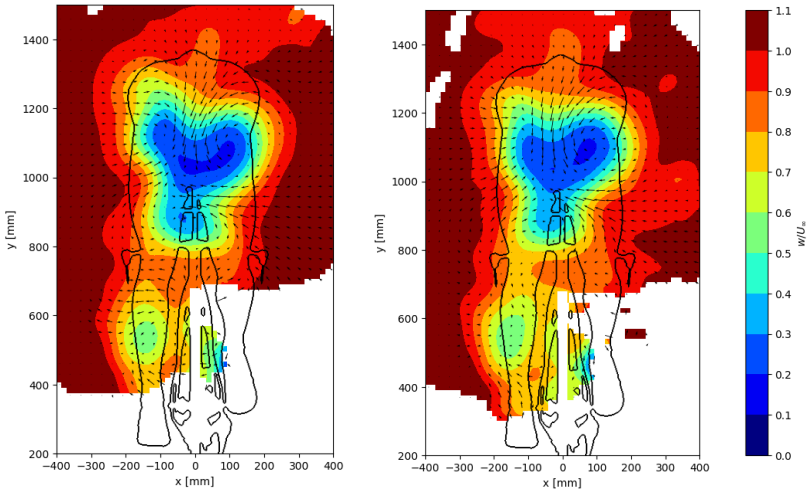

(a) Bare configuration **(b)** Zigzag on the arms

Figure 4.41: The effect of zigzag strips on the arms of the Symmetric GCM on the velocity flow field at $18\ m/s$

The vorticity flow field at $18\ m/s$, Figure 4.42, shows similar and dissimilar behaviours at $14\ m/s$. A similar change is the reduction of the left lower hip vortex, causing the combined vortex to change. The dissimilar change can be seen in the two CCR vortices, both of which have reduced in strength and size, which is the opposite as seen in the $14\ m/s$ case.

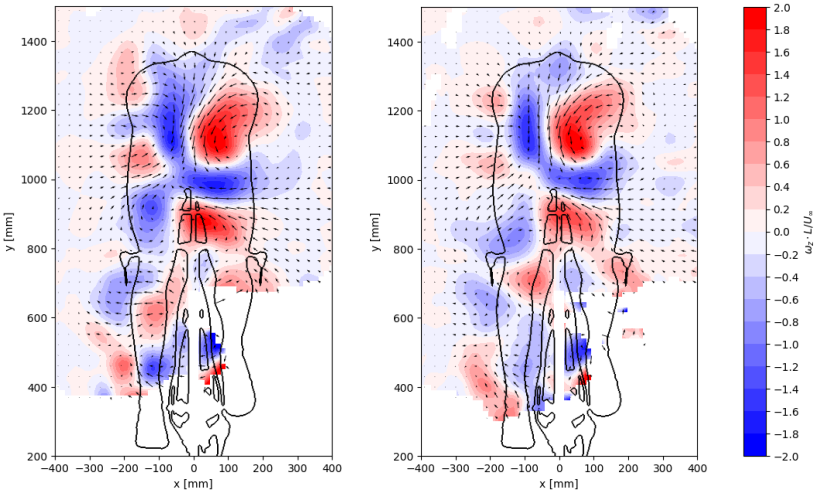

(a) Bare configuration **(b)** Zigzag on the arms

Figure 4.42: The effect of zigzag strips on the arms of the Symmetric GCM on the vorticity flow field at $18\ m/s$

4.4.2.1.2. Crosswind Effect

The aerodynamic loads indicate that at a crosswind of $8°$, the drag area is reduced by 4.7%. For this reason, the flow fields have been visualised, see Figure 4.43.

Unfortunately, the standard deviation of the zigzag strip on the arms at $8°$ shows a standard deviation of 40% in the region of the upper wake. This deviation is the reason for the large velocity difference in the upper wake.
The deviation difference between the two cases is too high to deem the comparison accurate, and thus will not be taken into account.

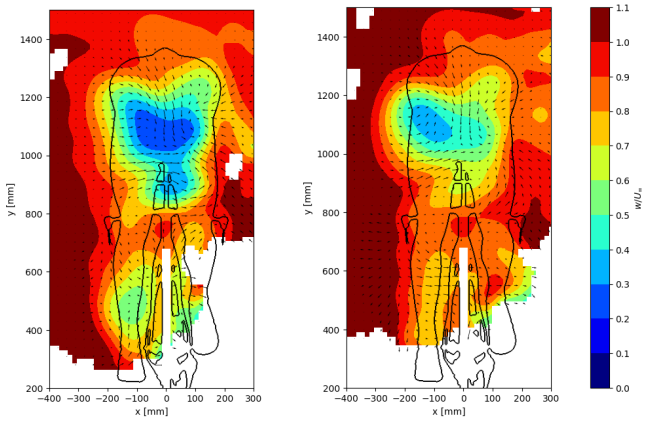

(a) Bare - w/U_∞ **(b)** Zigzag arms - w/U_∞

Figure 4.43: The effect of zigzag strips on the arms of the Symmetric GCM on the velocity flow field at $14\ m/s$ at $8°$

4.4.2.1.2.1. Reynolds Number Effect on the Crosswind Effect

The Reynolds number effect and the crosswind effect have been combined by testing at $18\ m/s$ at $8°$. The standard deviation of this case is lower near the upper part of the wake, and thus can be taken into account for the comparison. The wake behind the hips and legs, however, is deemed to have a higher uncertainty.

The zigzag strip results in a larger low velocity region in the upper wake, which is a similar change as seen in $14\ m/s - 0°$ case, but opposite of $18\ m/s - 0°$. Hence, it is challenging to determine whether the upper wake is accurate.

The vorticity flow fields show that the left lower hip vortex is reduced in strength, similar to the other cases. Nevertheless, the other vortices show different behaviours.

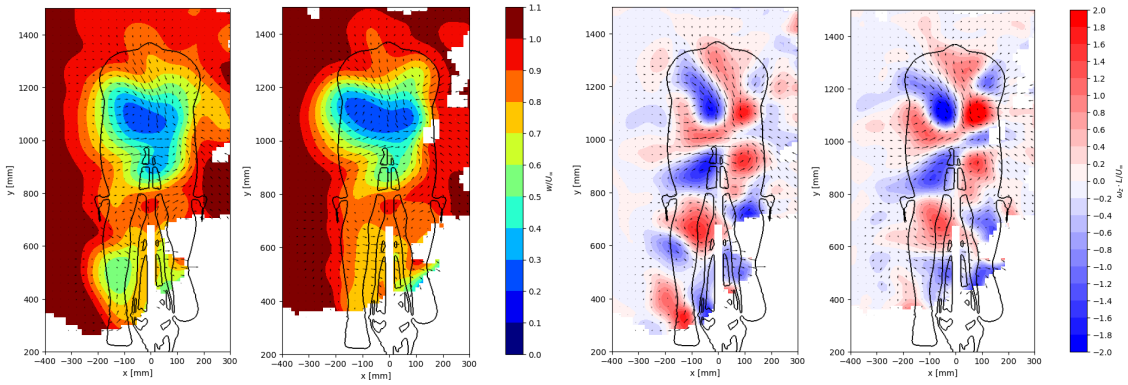

(a) Bare - w/U_∞ **(b)** Zigzag arms - w/U_∞ **(c)** Bare - ω_z/U_∞ **(d)** Zigzag arms - ω_z/U_∞

Figure 4.44: The effect of zigzag strips on the arms of the Symmetric GCM on the velocity flow field at $18\ m/s$ at $8°$

4.4.2.2. Uncertainty

As mentioned multiple times, the aerodynamic flow fields of the zigzag devices on the arms have a higher standard deviation, see Figure 4.45.
As can be seen, at $0°$ the deviation is in line with the standard deviation given in section 3.8. Hence, the data can be used for comparison and to analyse the effect of the zigzag strip on the arms. Looking into the standard deviation of the case $18\ m/s$-$8°$, the standard deviation is higher than the deviation seen in section 3.8, however, it is in line with the bare $18\ m/s$-$8°$ case. It seems that the $8°$ cases have higher standard deviations, which can be linked to the lower ratio between active tracks and total particles in the STB. Next to this, the total amount of particles is much higher for the crosswind cases. Since lower ratios lead to less accurate flow fields. The bare configuration and the zigzag on the arm cases at $18\ m/s$-$8°$ have a similar amount of total particles. Therefore, the direct comparison is possible.

The $14\ m/s$-$8°$ case shows a great standard deviation of approximately 45%. This deviation is deemed too large for comparisons and analysis. The total amount of particles is approximately doubled compared to the bare configuration. It can be said that there are too many particles in the STB, which leads to inaccuracies.

Although the no crosswind cases have an acceptable standard deviation, the behaviours do not align with each other, as different changes are visible. This begs the question of whether the flow field is accurate enough for the comparisons.

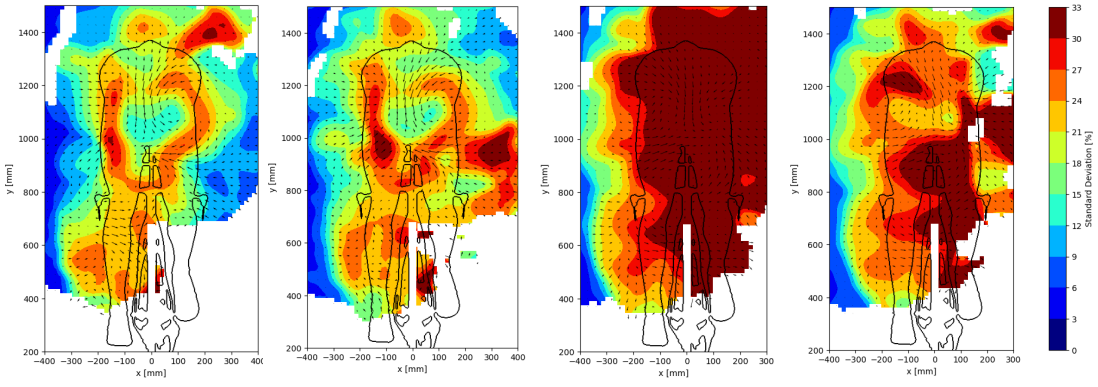

(a) $14\ m/s$ - $0°$ - Arms **(b)** $18\ m/s$ - $0°$ - Arms **(c)** $14\ m/s$ - $8°$ - Arms **(d)** $18\ m/s$ - $8°$ - Arms

Figure 4.45: The uncertainty in the flow field of the zigzag strips on the arms of the Symmetric GCM

4.4.3. Devices on the Legs

The effect of zigzag strips on the legs of the Symmetric GCM is investigated to understand whether drag reduction is possible. The zigzag strips are tested in two different positions, the lower part and the upper part of the leg.

The drag area of both positions is plotted against the wind speed and compared to the bare configuration in Figure 4.46. The zigzag strips on the upper part of the legs lead to an increase in drag area of at least 2% rather that the preferred drag area reduction. This can have multiple different reasons; the boundary layer around the upper legs is already in transition or turbulent, causing the zigzag strip to not work, as it only operates in laminar airflow. Another reason would be that the zigzag strip is located upstream, causing an earlier separation, generating a larger wake and thus increasing the drag area.

The zigzag strip on the lower part of the legs results in a drag reduction, where the entire $C_D A$ curve is lowered by 3%, except at $5\ m/s$, which is likely due to uncertainties rather than due to the zigzag strip itself. The effectiveness of the devices on the lower legs suggests that the airflow surrounding the lower legs is laminar. This shows a difference in airflow structure between the lower and upper legs, as the upper legs are linked to be in transition or turbulence. The effectiveness is linked to the triggering of the transition on the legs, the attachment of the airflow and the wake reduction that accompanies it. An interesting difference is spotted in the usefulness of the zigzag strips in comparison with the devices on the arms. The arms show a reduction in effectiveness at higher velocities, while the devices on the lower legs keep their effectiveness. As the devices on the lower legs have not reached a convergence, it can be said that the velocity of the minimal drag area is much higher than $25\ m/s$.

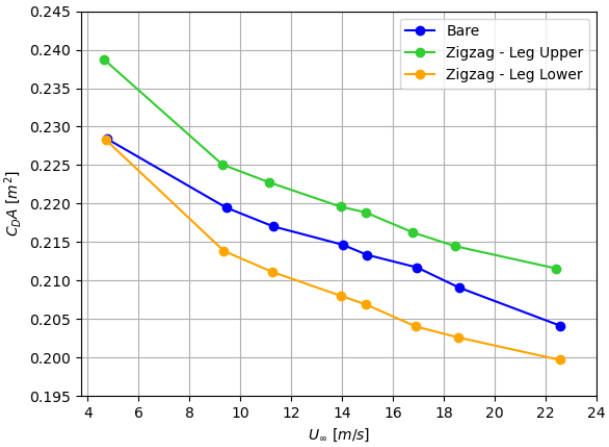

Figure 4.46: Effect of adding a zigzag strip to the upper and lower legs of the Symmetric GCM

Since the zigzag strips on the lower legs lead to a reduction in drag area, their effectiveness in crosswind was examined by placing the GCM at the angles $-8°$ and $8°$. In Figure 4.47, the crosswind results of the zigzag strips on the lower legs are plotted. At $-8°$, the effectiveness is relatively small, within 1% t, except for outliers of 2% at $5\ m/s$ and $10\ m/s$. This shows a similar behaviour as the zigzag strips on the arms, where the rotation of the straightest leg into the oncoming air is less prone to changes in the drag area.
The positive rotation, $8°$, yields a drag reduction across all velocities, with the freestream velocities lower than $15\ m/s$ leading to a reduction of approximately 1.5%. Higher velocities (than the $15\ m/s$) result in a higher reduction of around 4% to 7%. This change in behaviour is linked to the Reynolds number effect, as the wake reduction caused by the higher velocities is combined with the wake reduction of the devices.

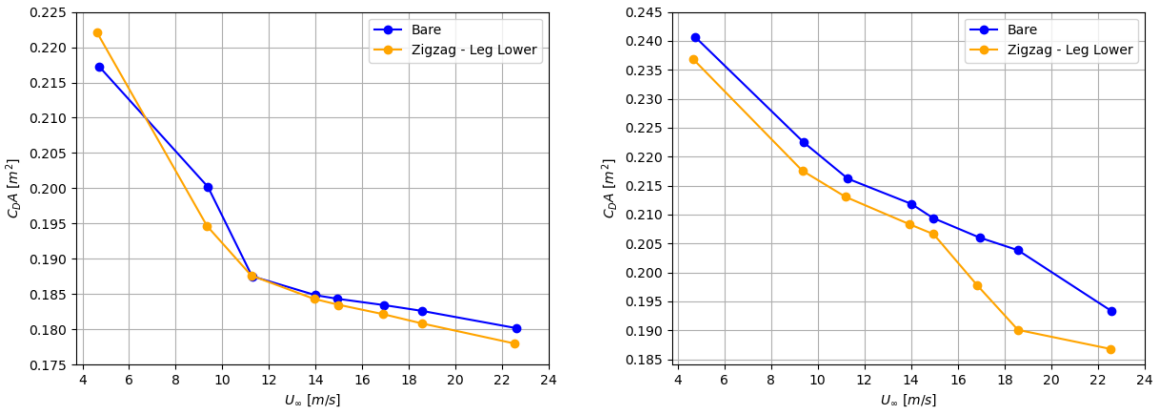

(a) Crosswind -8° **(b)** Crosswind 8°

Figure 4.47: Effect of adding a zigzag strip to the lower legs of the Symmetric GCM at crosswind angles

4.4.3.1. Aerodynamic Flow Field

The addition of a zigzag strip on the lower legs results in a drag reduction of 3% at the reference velocity. The effectiveness of the devices is based on the theory that the device triggers transition, keeps the airflow attached longer and yields a smaller wake.

To analyse whether the devices causes a smaller wake, the velocity flow field is visualised in Figure 4.48 and compared to the bare configuration (the Symmetric GCM without any flow control devices).
It is clear that the left lower leg wake is reduced in size. Next to this, the velocity deficit is resolved since the lowest velocity in the leg wake is increased from $w/U_\infty \approx 0.55$ to $w/U_\infty \approx 0.65$. From this, it can be concluded that the airflow has stayed attached longer, resulting in a smaller wake.
Analysing the lateral and vertical velocities field around the lower leg, see Appendix E, E.2, the effects are visible. The airflow behind the left knee has an outwashing motion, and behind the calf, an inwashing motion. The placement of the device caused the airflow behind the knee to turn into an inwash airflow, which is combined with the inwash behind the calf. The prior expanding motion of the leg wake has turned into a contracting wake motion with an expanding freestream velocity. Due to the change from outwash to inwash behind the knee, the left upper leg airflow, as well as the left hip airflow are altered. As the outwash is no longer present behind the knees, the inwash behind the hips is able to connect with the outwash behind the right knee, pushing the inwash over the right hip to the right. The vertical velocity field shows an upwash behind the left heel, creating the compression of the lower leg wake. Moreover, the upwash on the side of the left upper leg and knee has become more neutral.
The standard deviation of the $14\ m/s$ case with zigzag strips on the legs shows a much higher uncertainty than the bare configuration in the upper wake. Therefore, the changes in the upper wake are not taken into account for the effect caused by the flow control devices.

The changes caused by the flow control devices are not visible for the right leg due to the lack of data; however, it can be assumed that they have a similar but smaller change.

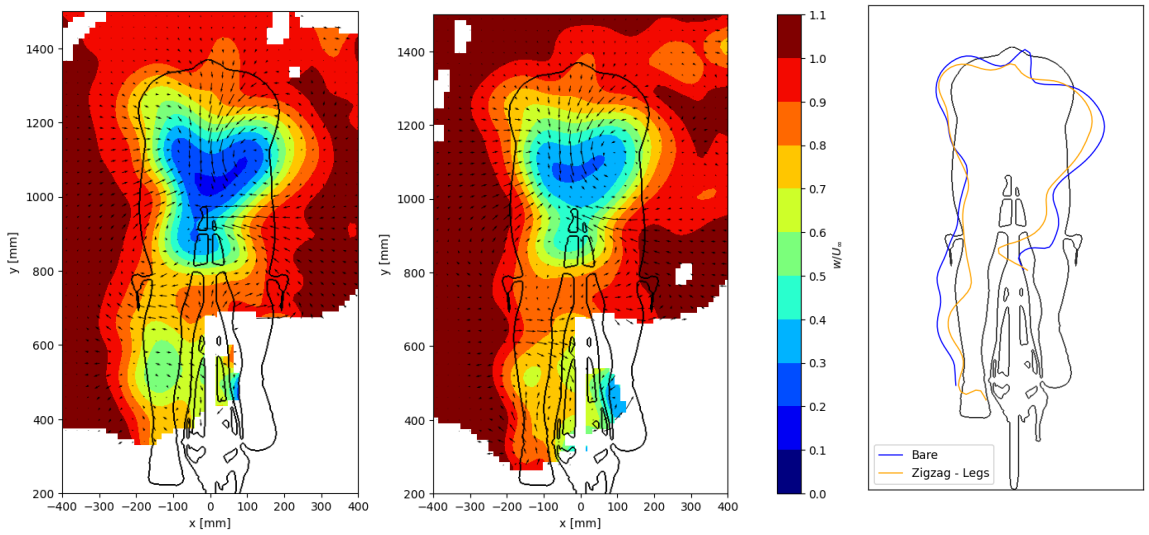

(a) Bare configuration **(b)** Zigzag on lower legs **(c)** Contour at $w/U_\infty \approx 0.85$

Figure 4.48: The effect of zigzag strips on the lower legs of the Symmetric GCM on the velocity flow field at $14\ m/s$

The velocity fields show numerous changes caused by the addition of the zigzag strip on the lower part of the legs. Based on this, the vorticity flow field has been altered too, see Figure 4.49. The main differences around the left leg are the counter-clockwise vortex stemming from the calf and the clockwise rotating airflow near the heel and between the left leg and rear wheel. The CR vortices from the heel and between the legs and wheel, became stronger, linked to the compressed motion of the wake, and have spread upwards. A CR vortex is generated from the left calf, previously a CCR vortex. Due to this, the original calf vortex has weakened in strength and moved upwards. The comparison of the strength of the vortices can be seen in Appendix E, E.2.

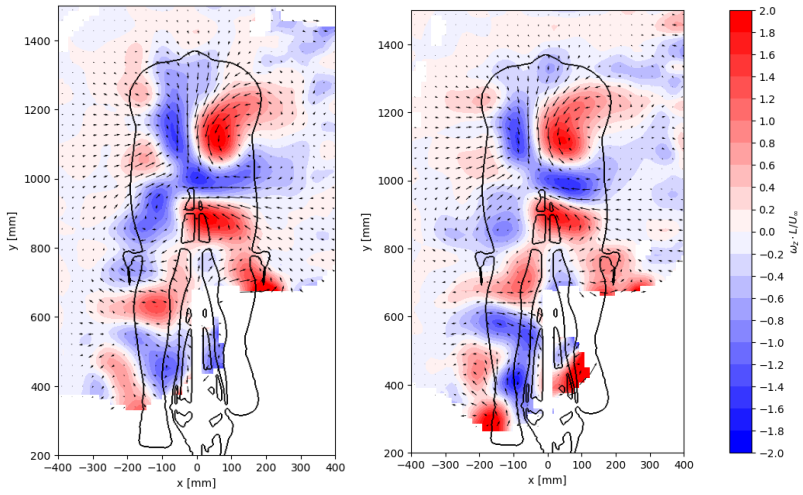

(a) Bare configuration **(b)** Zigzag on lower legs

Figure 4.49: The effect of zigzag strips on the lower legs of the Symmetric GCM on the vorticity flow field at $14\ m/s$

4.4.3.1.1. Reynolds Number Effect

The addition of the zigzag strip on the lower part of the legs leads to a drag area reduction at all velocities. To analyse whether the behaviour changes are the same at different velocities, PIV measurements have been performed at $18\ m/s$. The loads indicate that at $18\ m/s$, the drag area reduction is 3.6%, which is slightly higher than at $14\ m/s$.

Figure 4.50 displays the velocity flow field of the zigzag strips and the bare configuration at $18\ m/s$. The wake behind the left lower leg has become smaller due to the addition of the devices. Next to this, the velocity in the wake is increased. This is the exact same behaviour that was spotted at the $14\ m/s$ case, indicating that the zigzag strip is triggering transition and keeping the airflow attached longer. The wake connecting the lower leg wake to the upper wake has a different behaviour than previously, as the velocity has decreased, which is caused by the changes in lateral and vertical velocity, see Appendix E, E.2.1. The $18\ m/s$ case with the zigzag strip shows an outwashing airflow behind the upper left leg, while this was not present at the $14\ m/s$ case.

The velocity fields show that the upper wake is not influenced by the devices on the legs, which is more in line with expectations. In this case, the standard deviation is similar to that of the bare configuration. For this, it can be concluded that the changes in the upper part of the wake are caused by uncertainties and not the flow control devices.

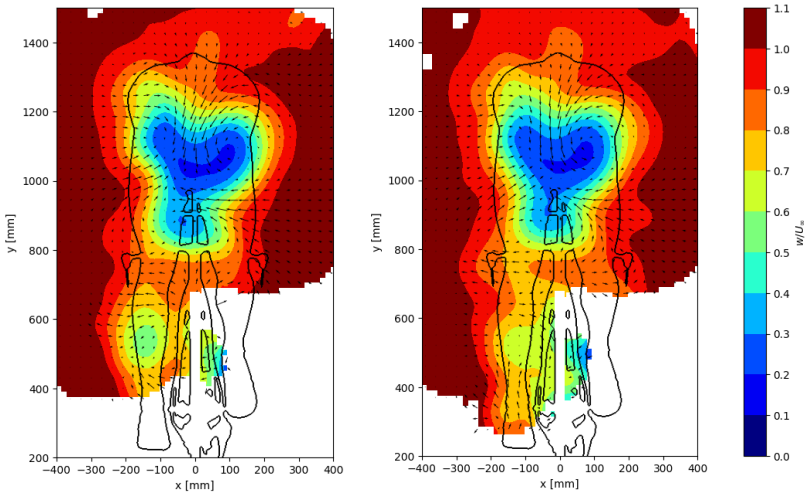

(a) Bare configuration **(b)** Zigzag on the lower legs

Figure 4.50: The effect of zigzag strips on the lower legs of the Symmetric GCM on the velocity flow field at $18\ m/s$

The vorticity flow field, Figure 4.51, shows the same alterations as the $14\ m/s$ case. With the CCR calf vortex being moved upwards, and the CR vortex becoming stronger. Furthermore, the CR airflow is present between the left lower leg and the rear wheel, similarly to $14\ m/s$. A difference is that in the $18\ m/s$ case, the CCR calf vortex has become stronger when the devices were added, while at $14\ m/s$ it was weakened.
The left lower hip vortex has moved to the left and has become larger due to the devices. This behaviour is different from the $14\ m/s$ case as it shows a weakening.

The differences in the vorticity flow fields of the $14\ m/s$ and $18\ m/s$ are mainly caused by the high uncertainty of the $14\ m/s$ case. Smaller changes in the behaviour, magnitude in vortices and placements are likely caused by the Reynolds number shift. This is based on the loads when the devices cause a larger drag area reduction at $18\ m/s$

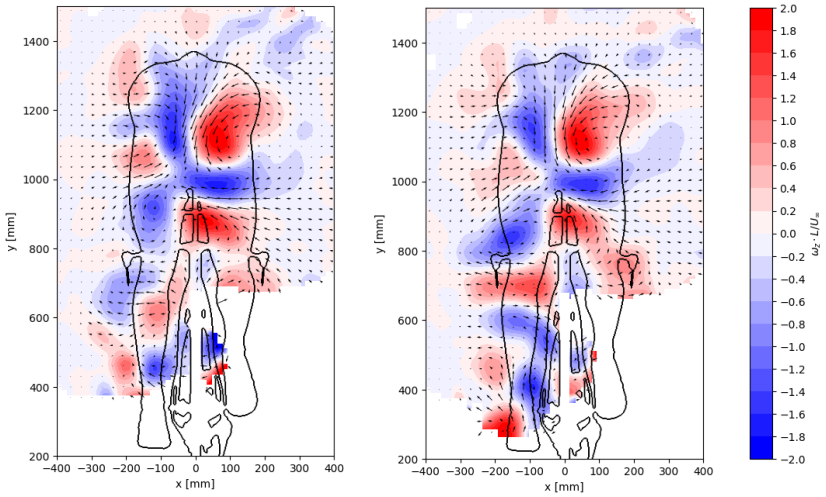

(a) Bare configuration **(b)** Zigzag on the lower legs

Figure 4.51: The effect of zigzag strips on the lower legs of the Symmetric GCM on the vorticity flow field at $18\ m/s$

4.4.3.1.2. Crosswind Effect

Additionally, the effectiveness of the zigzag strip was tested under crosswind angles. It was seen that at $8°$ the drag area was reduced by 1.7% at the reference velocity. The flow fields are displayed in Figure 4.52.

Similarly, the wake of the left lower leg has been reduced by the zigzag strip, and the velocity in the wake is increased. Also in this case, the upper wake has not been affected by the devices.
The vorticity flow field shows a similar behaviour; however, the magnitude of the vortices is lower under the crosswind. This is caused by the right leg and the rear wheel altering the airflow before it reaches the left leg.

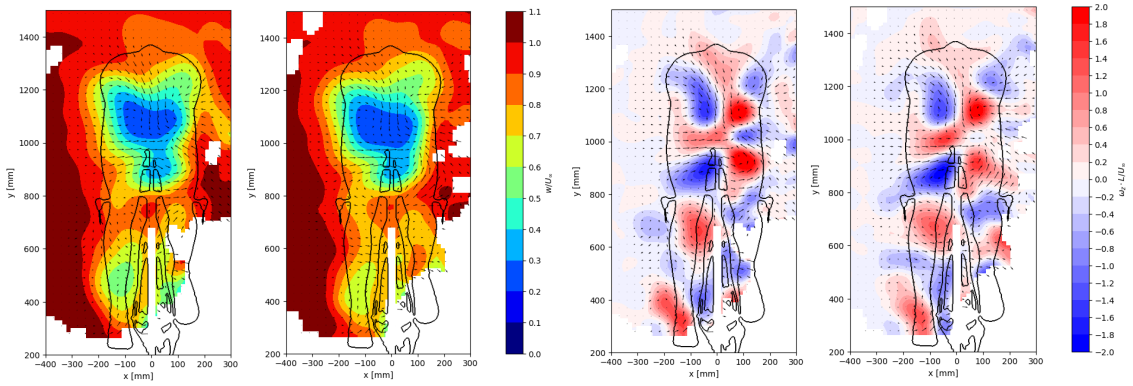

(a) Bare - w/U_∞ **(b)** Zigzag legs - w/U_∞ **(c)** Bare - ω_z/U_∞ **(d)** Zigzag legs - ω_z/U_∞

Figure 4.52: The effect of zigzag strips on the lower legs of the Symmetric GCM on the velocity flow field at $14\ m/s$ at $8°$

4.4.3.1.2.1. Reynolds Number Effect on the Crosswind Effect

The crosswind effect has been combined with the Reynolds effect for the zigzag strip, which is examined at $18\ m/s$ at $8°$.

The flow fields are displayed in Figure 4.53, as can be seen, the changes in the flow field caused by the devices are the same. The left leg wake has been reduced, and the velocity in the wake has been increased. Furthermore, the vortices are changed in a similar way to the changes in the crosswind of $14\ m/s$.

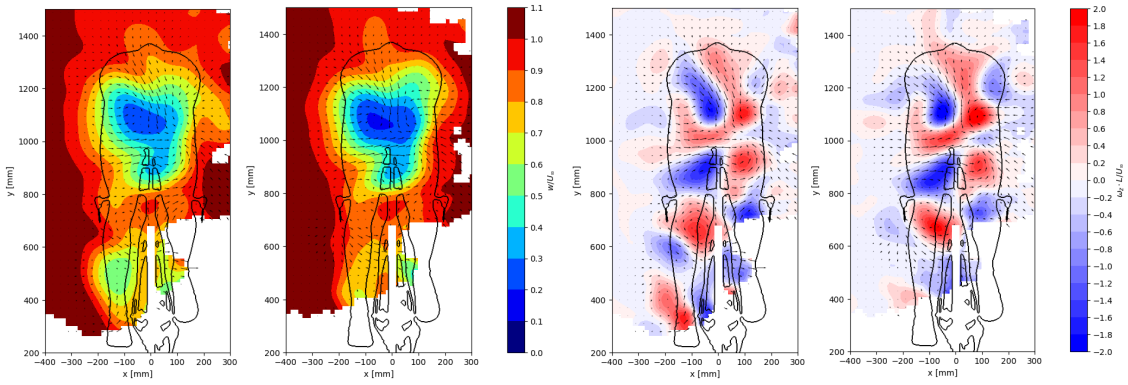

(a) Bare - w/U_∞ **(b)** Zigzag legs - w/U_∞ **(c)** Bare - ω_z/U_∞ **(d)** Zigzag legs - ω_z/U_∞

Figure 4.53: The effect of zigzag strips on the lower legs of the Symmetric GCM on the velocity flow field at $18\ m/s$ at $8°$

4.4.4. Conclusion

The flow control devices have been placed on four different locations, the hips, upper arms, upper legs and lower legs. For the hips, three vortex generators are used to try to delay the separation and are placed at different locations on the Symmetric GCM's hips. All combinations of VGs and placements result in an increase in the drag area, thus leading to an undesired effect. The reason for the drag area is that the VGs likely trigger an earlier separation, causing a larger wake.
The devices placed on the upper arms and lower legs, the zigzag strips, do have the desired effect as they lower the drag area. While, the upper legs result in a drag area increase. The zigzag strips are effective at all Reynolds numbers, meaning that it follows the same Reynolds effect trend as the bare configuration. The drag area reduction is caused by the triggering of the transition of the laminar airflow. Due to this, the airflow stays attached to the limb longer, as explained with the critical Reynolds number theorem.
Besides this, the devices were tested on two crosswind angles, $-8°$ and $8°$, to analyse the effectiveness in crosswind. In both cases, the devices do not work under $-8°$ winds, while they have a desired effect at $8°$. This change in effectiveness can be linked to the leg position, since the straighter leg is placed in the airflow, which does not respond to the devices and shows a higher drag area compared to the bent leg.

The zigzag strips on the arms of the Symmetric GCM result in interesting flow fields. The effect of the strips is difficult to match to the drag area reduction since the changes are different for different cases, for example, comparing $14\ m/s$ to $18\ m/s$, and as they are not as expected.

The aerodynamic flow fields show that adding the zigzag strip on the legs leads to a wake reduction. The wake is reduced in size, and the velocity within the wake has increased. This shows that the zigzag strip triggers a transition and causes the airflow to stay attached longer.
The behavioural changes in the aerodynamics caused by the devices are similar at different Reynolds numbers, showing that the freestream velocity does not alter the effectiveness. Next to this, the flow field at $8°$ shows the same effects, a left leg wake reduction.

5

Conclusion

The goal of this thesis was to research and report the aerodynamic sensitivity of the Symmetric Generic Cyclist Model and to compare the sensitivity to the Asymmetric GCM. The sensitivity is analysed in four different categories: the influence of the leg position, the influence of the Reynolds number effect, the influence of the crosswind effect and the influence of the addition of passive flow control devices. The sensitivity was tested based on the aerodynamic load, drag area, and the visualisation of the flow field.

The wind tunnel experiment shows that the Symmetric GCM has a 4.6% drag area reduction compared to the Asymmetric GCM at the reference velocity of $14\ m/s$. This shows the effect that legs have on the aerodynamics of the cyclist. The drag area difference can be explained by the flow field characteristics, the wake and the vorticity. The wake of the Symmetric GCM shows that the velocity within the wake is higher and has a more symmetric shape. The main difference in the wake is near the left leg of the cyclist; the right leg was not measured due to the lack of data. The Asymmetric GCM yields a larger leg wake with lower velocities. Besides the wake changes caused by the leg position, the vorticity has been altered too. The Symmetric GCM shows two major counter-clockwise rotating (CCR) vortices stemming from the right upper hip and inner thighs. Moreover, it shows that the four clockwise rotating (CR) vortices, generated by the left upper and lower hip as well as the left inner thigh and the right lower hip, are combined into one large vortex. The leg position caused the vortices to move positions, and the strengths have been altered. The Asymmetric GCM shows that the right upper hip vortex has reduced in strength and is combined with the CCR vortex of the inner thigh. Next to this, the CR vortices are not combined in the Asymmetric case, as it only has the left upper and lower hip vortex. The vortices stemming from the legs are more difficult to compare, as the bicycle generates vortices too. Furthermore, the vortices of the Asymmetric GCM last longer than the Symmetric GCM, which is in line with the drag area reduction seen with the Symmetric GCM. The comparison between the Symmetric and Asymmetric GCM indicates that the leg position alters the aerodynamics of the cyclist, with the symmetric position leading to a lower drag area.

The influence of the Reynolds number variation has been tested by altering the velocity. The aerodynamic loads indicate that the increase in velocity leads to a reduction in aerodynamic drag area. A total decrease of 11% is seen when comparing the drag area of the velocities $5\ m/s$ to $25\ m/s$. The drag reduction is linked to the critical Reynolds number theorem, which explains that the increase in velocity triggers a transition state in the airflow. This state caused the airflow to stay attached longer to the body, leading to a reduced wake width behind. The velocity fields of the $10\ m/s$, $14\ m/s$, and $18\ m/s$ cases displays the changes in the wake caused by the Reynolds number effect. The upper wake becomes more symmetric at higher velocities, and the velocity within the wake becomes lower. Consequently, the wake width of the upper part is lessened when the velocity is increased. The wake behind the legs shows an opposite behaviour, with the velocity increase leading to a more compressed wake with a smaller low velocity region. This behaviour can be explained by the critical Reynolds number theorem. Besides the changes in the wake, the vortices are affected too. The vortices stemming from the body are increased in strength as the velocity is raised, while the leg vortices are weakened. Regardless of the lower velocity in the upper wake and the strengthened vortices when the Reynolds number is raised, the drag area is reduced. This can be linked to the theory that the leg wake has a greater effect on the aerodynamics.

The Asymmetric GCM shows the same behavioural changes as the Symmetric GCM in the flow field. The upper wake width is reduced while the velocity within the wake is lowered. A difference between the two, is that the effect is larger for the Asymmetric GCM, which is linked to the leg position. Similarly, the leg wake is reduced, in a larger effect, due to the Reynolds number variation. This behaviour supports the theorem that the leg wake has a great influence.

By examining the crosswind effect on the Symmetric GCM, it shows that the angle of incoming airflow alters the aerodynamics of the cyclist. Placing the straighter leg into the airflow leads to a drag area reduction at all values, while the bent leg only shows a reduction at larger angles. The difference in behaviour shows that the small difference in the lower leg position has an effect on the drag area, with the drag area being lower when the leg is straighter. This behaviour is different for the Asymmetric GCM; in this case, the extended leg (placed into the airflow) converges after a certain angle, while the bent leg keeps a decreasing motion. This shows that the difference between the Symmetric straight legs and Asymmetric straight legs has a large influence on the drag area at crosswind.
The aerodynamic flow field shows the effect of the crosswind on the Symmetric GCM, where both the upper and lower parts of the wake are influenced. The crosswinds lead to a shift in the shoulder wake, with the incoming shoulder having a larger wake. Next to this, the velocity within the wake is changed, with the velocity being lowered when the straighter leg is placed into the airflow. The straighter leg pointed into the airflow leads to a smaller wake with a smaller low-velocity region, while the opposite is present when the bent leg is placed into the airflow.
The Asymmetric GCM shows a greater effect on the crosswind presence, yet the behaviour in the upper wake is similar. The lower leg, however, shows a different effect, which is a line with the difference in drag area, as the symmetric GCM has a lower drag area. The extended leg has a larger wake with lower velocities when placed into the airflow.
Correspondingly, the leg wake shows a great influence on the overall drag area of both the Symmetric and Asymmetric GCM.

Lastly, the influence of adding flow control devices to the Symmetric GCM to reduce the drag area is analysed. Vortex generators (VG) are placed near the separation line of the hips. Three different VG types at different locations have been tested, and the aerodynamic loads indicate that they raise the drag area rather than reduce it. The VGs likely trigger the separation earlier, causing the wake to increase.
A second type of flow control device, zigzag strips, is investigated on the arms and legs of the Symmetric GCM. The placement of the strip on the arms leads to a drag area reduction of 4.5%. The reduction becomes less effective at larger velocities, ineffective under negative crosswind angles and less effective at positive crosswind angles. The flow fields of the wake and vortices show different changes based on the velocity and crosswind angle tested. With $14\ m/s$ shows a worse wake, while $18\ m/s$ shows an improvement in the wake. From this, it is difficult to connect the drag area reduction to a specific change in the flow field. Furthermore, the uncertainty is larger at crosswinds, leading the flow field not to be deemed accurate enough for comparisons.
The zigzag strip is placed on the upper and lower parts of the legs. The aerodynamic loads show that the upper leg zigzag strip leads to a drag increase, which can be explained by the airflow over the upper legs not being laminar. The lower legs, however, result in a drag reduction as the airflow is laminar. The drag area is reduced by 3% at each velocity; similarly, a small reduction is seen at positive crosswind angle, but ineffective at the negative crosswind angle. The flow field of the zigzag strip on the lower legs shows a wake compression and an increase in the wake velocity. This shows that the zigzag strip triggers a transition, causing the airflow to stay attached longer. The effect on the leg wake is spotted at different Reynolds numbers as well as during crosswind.
From this, it can be concluded that altering the aerodynamics by zigzag strips on the arms and lower legs can lead to drag reduction.

This research shows the sensitivity of the Symmetric GCM, and it can be concluded that the position of the leg is of importance for the drag area and flow field. Furthermore, it is theorised that the wake caused by the legs has a greater influence on the overall drag area than the wake generated by the body. However, this cannot be said with certainty as the right leg wake has not been visualised.

5.1. Discussion

This research shows the relevance of analysing the aerodynamics of the cyclist at a symmetrical leg position and the comparison to the asymmetric position. The conclusion of the thesis can be used in further experiments of the Generic Cyclist Model, and can be applied in different experiments using different cyclist models. Similarly, the conclusion in this report has not been found in different papers and decreased the knowledge gap in the cyclist aerodynamics.

Regardless, the conclusion in this thesis must be taken with caution, as there are multiple uncertainties in the experiment. For instance, the uncertainty is within the experimental setup and the measurement techniques. The tests with the Asymmetric GCM show that there are differences in the experiments, both in the aerodynamic loads and in the flow field. Thus, there is an error within the measurements that could have influenced the conclusions slightly. Furthermore, the repeatability of the Symmetric GCM indicates multiple errors that happened during the load measurement, which can alter the conclusion. The experimental setup causes a lack of data near the lower part of the legs and the right leg. Due to this, no definite answer on the influence the categories have on the legs can be given. Next to this, the setup, combined with the post-processing, leads to the uncertainties in the flow fields. Some cases have much larger standard deviations, causing the results to be incorrect and comparisons to be deemed inaccurate.

6

Recommendations

This chapter states the recommendations for any further work with the Generic Cyclist Model. During the experiment, multiple decisions were made that have led to uncertainty or issues later on. Furthermore, the post-processing of the PIV data has introduced uncertainties that can be changed.

Recommendations for the aerodynamic load measurements

- The aerodynamic loads have been measured at velocities that differ from the actual input velocity, which leads to comparisons being more difficult to make, as it introduces errors. For this reason, it is recommended to ensure that the actual velocity is as planned. For example, measure at exactly $10\ m/s$ or $25\ m/s$.
- The Reynolds number-Crosswind correction has been performed at the angles: $10°$, $15°$ and $20°$. Based on the results, it was noted that the correction has a notable effect on the drag area measured. Meaning that the non-corrected crosswind results have errors which can alter the conclusions. Next to this, it was noted that due to the correction, the results measured at smaller angles, for example $\pm 8°$, are likely to have this error too. Thus, the Reynolds number-Crosswind correction affects the data at all crosswind angles. Hence, it is recommended to perform the Reynolds number-Crosswind correction at all crosswind angle tests during the experiment.

Recommendations for the PIV measurements

- During the PIV measurements, images are taken every millisecond. During the post-processing, it was seen that after every 25 images, the photo is brighter. Due to this, the pre-processing filter is not able to remove the background in the photo, causing issues during the Shake-The-Box (STB). The STB detects more particles in these brighter images, as indicated by the peaks in the statistics. The reason for the brighter images is a flickering light in the wind tunnel. Thus, it would be recommended to turn this light off during the measurements.
- A conclusion of the research is that the leg wake has a larger effect on the drag area of the cyclist. However, due to the lack of data on the right leg, no definite conclusion can be given. For this reason, it is important that the full leg wake is visualised during the experiment. It is recommended to change the experimental setup to allow for two LED's and two cameras on each side of the cyclist, rather than all on the left side.
- The placement of the seeder in the wind tunnel causes limitations with the reachability of the particles. Therefore, for the experiment with the GCM in the TU Delft OJF, it would be recommended to increase the height of the fake floor to allow more particles near the legs.
- In connection with the above-mentioned recommendation, further changes to the seeder can be made. At low velocity, the particles do not expand as well as at other velocities, leading to a lack of data surrounding the GCM. Thus, it would be recommended to change the seeder such that the particles are able to reach more parts of the wake.
- The reflection of the wheels and hips influences the post-processing. It is recommended to try to reduce the reflections, which can be done by adding more non-reflective paint on the wheels and

GCM. Note that the paint added must be smooth in order not to influence the aerodynamics of the GCM.

- It would be recommended to extend the PIV volume in the streamwise direction. This would allow for the flow field closer to the GCM to be visualised. Preferably, the volume is extended in front of the legs to understand and analyse the intersection of the wake of the arms and bike with the body and upper legs. The extension of the flow field would also allow for the crosswind rotation correction to not lose any extra data.

Recommendations for the flow control devices

- The oil flow visualisations that were used to determine the separation line were not optimal. The thin liquid 'paint' is affected too much by gravity, with interference with the visualisation of the separation line. Therefore, it is recommended to find a better way to visualise the separation line. This can be done by using a different oil flow 'paint' that is less subject to gravity.
- The placement of the vortex generators leads to a drag area increase, and it is likely that a different position can have a more beneficial effect. Therefore, if vortex generators are experimented with in the future, it would be recommended to test more downstream locations.
- The effect of the zigzag strips on the arms on the aerodynamic flow fields was difficult to determine as the PIV volume is further downstream and the body interferes with the airflow. To better understand the effect of the zigzag strip, it would be recommended to have a second PIV volume behind the arms.

Recommendations for the post-processing

- The parameters in the filters of the post-processing of the PIV data have significant effects on the flow fields. It would be recommended, if time allows, to have an extensive study on the effects of the parameters on the flow fields to find the most optimal ones. Based on the comparisons between the flow fields of the Asymmetric GCM during the current experiment and a prior experiment, differences were found in the velocity of the wake. This difference was likely caused by the post-processing parameters; however, the exact parameter and the corresponding value could not be identified. Due to this, there are uncertainties in the flow fields of all the cases.

References

[1] Achenbach, E. “Distribution of local pressure and skin friction around a circular cylinder in cross-flow up to Re = 5:10^6”. In: *Journal of Fluid Mechanics* 34 (1968), pp. 625–639.

[2] Achenbach, E. “Experiments on the flow past spheres at very high Reynolds numbers”. In: *Journal of Fluid Mechanics* 54 (1972), pp. 565–575.

[3] Barlow, J.B., Rae, W.H., and Pope, A. *Low-speed wind tunnel testing*. John wiley & sons, 1999. ISBN: 978-0-471-55774-6.

[4] Brown, C., Burton, D., Crouch, T.N and Thompson, M.C. “The influence of turbulence on cycling aerodynamics”. In: *Journal of Wind Engineering and Industrial Aerodynamics* 242 (2023), p. 105575. ISSN: 0167-6105. DOI: 10.1016/j.jweia.2023.105575.

[5] Brownlie, L.W., Aihara, Y., Carbo, J., Harber, E., Henry, R., Ilcheva, I. and Ostafichuk, P. “The Use of Vortex Generators to Reduce the Aerodynamic Drag of Athletic Apparel”. In: *Procedia Engineering* 147 (2016), pp. 20–25. DOI: 10.1016/j.proeng.2016.06.183.

[6] Crouch, T.N., Burton, D., Brown, N.A.T., Thompson, M.C. and Sheridan, J. “Flow topology in the wake of a cyclist and its effect on aerodynamic drag”. In: *Journal of Fluid Mechanics* 748 (2014), pp. 5–35. DOI: 10.1017/jfm.2013.678.

[7] Crouch, T.N., Burton, D., LaBry, Z.A. and Blair, K.B. “Riding against the wind: a review of competition cycling aerodynamics”. In: *Sports Engineering* 20 (2017), pp. 81–110. DOI: 10.1007/s12283-017-0234-1.

[8] Defraeye, T., Blocken, B., Koninckx, E., Hespel, P. and Carmeliet, J. “Aerodynamic study of different cyclist positions: CFD analysis and fullscale wind-tunnel tests”. In: *Journal of Biomechanics* 43.7 (2010), pp. 1262–1268. DOI: 10.1016/j.jbiomech.2010.01.025.

[9] Deval, P. “Cylinder Drag Reduction Using Discrete Surface Roughness”. In: (2023). URL: https://repository.tudelft.nl/file/File_34d09226-7654-4206-ad0a-86c808b680d0?preview=1.

[10] Gibertini, G. and Grassi, D. “Cycling Aerodynamics”. In: *CISM International Centre for Mechanical Sciences, Courses and Lectures* (June 2009), pp. 23–47. DOI: 10.1007/978-3-211-89297-8_3.

[11] Giljarhus, K.E.T, Stave, D.A. and Oggiano, L. “Investigation of influence of adjustments in cylist arm position on aerodynamic drag using computational fluid dynamics”. In: *Proceedings* 49 (2020), p. 159. DOI: 10.3390/proceedings2020049159.

[12] Kyle, C.R. and Burke, E. “Improving the racing bicycle”. In: *Mechanical Engineering* 106.9 (1964), pp. 34–35. URL: https://www.scopus.com/inward/record.uri?eid=2-s2.0-0021495040&partnerID=40&md5=a7998dcf0dce86b5a80f8178a71254cc.

[13] Lignarolo, L.E.M., Ragni, D., Krishnaswami, C., Chen, Q. Simão Ferreira, C.J. and van Bussel, G.J.W. “Experimental analysis of the wake of a horizontal-axis wind-turbine model”. In: *Renewable Energy* 70 (2014), pp. 31–46. ISSN: 0960-1481. DOI: 10.1016/j.renene.2014.01.020.

[14] Lin, J.C. “Review of research on low-profile vortex generators to control boundary-layer separation”. In: *Progress in Aerospace Sciences* 38.4 (2002), pp. 389–420. DOI: 10.1016/S0376-0421(02)00010-6.

[15] Maddocks, P. and Walker, A.D. “Effect of arm position on the aerodynamic drag of an individual time trial position”. In: *Sports Engineering* 28 (Mar. 2025). DOI: 10.1007/s12283-025-00495-7.

[16] Maleki Dastjerdi, S., Arbelo Romero, J., Terra, W. and Sciacchitano, A. “Influence of cross-wind angle and Reynolds Number of the aerodynamics of the generic cyclist model”. In: *21th International Symposium on Flow Visualization* (2025).

[17] Malizia, F. and Blocken, B. “Bicycle aerodynamics: History, state-of-the-art and future perspectives”. In: *Journal of Wind Engineering and Industrial Aerodynamics* 200 (2020), p. 104134. DOI: https://doi.org/10.1016/j.jweia.2020.104134.

[18] Martin, J., Davidson, C. and Pardyjak, E. “Understanding Sprint-Cycling Performance: The Integration of Muscle Power, Resistance, and Modeling”. In: *International journal of sports physiology and performance* 2 (Apr. 2007), pp. 5–21. DOI: 10.1123/ijspp.2.1.5.

[19] Martin, J.C., Milliken, D.L., Cobb, J.E., McFadden, J.L. and Coggan, A.R. “Validation of a Mathematical Model for Road Cycling Power”. In: *Journal of Applied Biomechanics* (Aug. 1998), pp. 276–291. DOI: 10.1123/jab.14.3.276.

[20] Rooij, R.P.J.O.M. and Timmer, W. “Roughness Sensitivity Considerations for Thick Rotor Blade Airfoils”. In: *Journal of Solar Energy Engineering-transactions of The Asme - J SOL ENERGY ENG* 125 (Jan. 2003). DOI: 10.1115/1.1624614.

[21] Scarano, F. “Experimental Aerodynamics”. In: *AE4-180 Flow Measurement Techniques* (Feb. 2013).

[22] Schanz, D., Gesemann, S. and Schröder, A. “Shake-The-Box: Lagrangian particle tracking at high particle image densities”. In: *Experiments in Fluids* 57 (2016). DOI: 10.1007/s00348-016-2157-1.

[23] Sutherland, W. “LII. The viscosity of gases and molecular force”. In: *Philosophical Magazine* 5.36 (1893), pp. 507–531. DOI: 10.1080/14786449308620508.

[24] Delft University of Technology. *Open Jet Facility*. URL: https://www.tudelft.nl/lr/organisatie/afdelingen/flow-physics-and-technology/facilities/low-speed-wind-tunnels/open-jet-facility.

[25] Terra, W., Brown, C., Vloemans, S., van der Waals, M., Sciacchitano, A., Burton, D., Thompson, M.C. and Huysmans, T. “A Generic Cyclist Model for aerodynamic investigation: Design, geometry & first aerodynamic analysis of a male time-trial and sprint model”. In: *Journal of Wind Engineering & Industial Aerodynamics* 252 (Sept. 2024), p. 105829. DOI: 10.1016/j.jweia.2024.105829.

[26] Terra, W., Sciacchitano, A. and Scarano, F. “A Novel Approach for Skin Suit Aerodynamic Optimization Using Local Momentum Deficit”. In: *Proceedings of the 12th Conference of the International Sports Engineering Association* 2.6 (2018). DOI: 10.3390/proceedings2060222.

[27] Terra, W., Sciacchitano, A. and Scarano, F. “Cyclist Reynolds number effects and drag crisis distribution”. In: *Journal of Wind Engineering & Industial Aerodynamics* 200 (May 2020), p. 104143. DOI: 10.1016/j.jweia.2020.104143.

[28] Timmer, N. and Veldhuis, L. “The Impact of Skinsuit Zigzag Tape Turbulators on Speed Skating Performance”. In: *Applied Sciences* 11 (2021). DOI: 10.3390/app11030988.

A

Test Plan

The test plan during the experiment is given below, stating the GCM configuration and at which velocities and yaw angles it was tested per run. Besides this, it also indicates whether flow control devices were used and if PIV measurements were performed.

Run	Velocity	Yaw	GCM	Flow Control	PIV / Flow Vis	Note
1	0-5-10-12-14-15-18-20-25-0	0°	ASYM	-	-	Fake floor at -2.4cm
2	0-5-10-12-14-15-18-20-25-0	0°	ASYM	-	-	Fake floor at 0cm
3	0-5-10-12-14-15-18-20-25-0	0°	ASYM	-	-	Fake floor at 14.5cm
4	0-5-10-12-14-15-18-20-25-0	0°	ASYM	-	-	Fake floor at -2.3cm
5	0-5-10-12-14-15-18-20-25-0	0°	ASYM	-	-	Fake floor at 0cm - seeding changed
6	0-5-10-12-14-15-18-20-25-0	0°	ASYM	-	-	As RUN 5 with tape
7	0-5-10-12-14-15-18-20-25-0	0°	ASYM	-	-	As RUN -6° with visor added
8	0-5-10-12-14-15-18-20-25-0	0°	ASYM	-	-	As RUN 7 with a shielding plate
9	0-5-10-12-14-15-18-20-25-0	0°	ASYM	-	-	As RUN -8° with seeder air
10	0-5-10-12-14-15-18-20-25-0	0°	ASYM	-	-	As RUN -8° with helium bubbles
11	0-5-10-12-14-15-18-20-25-0	0°	ASYM	-	-	As RUN -8° remounted cyclist
12	0-5-10-12-14-15-18-20-25-0	0°	ASYM	-	-	As RUN 11 with the seeder off
13	10	0°	ASYM	-	PIV	GCM ASYM 10 0
	14	0°	ASYM	-	PIV	GCM ASYM 14 0
	15	0°	ASYM	-	PIV	GCM ASYM 15 0
	14	0°	ASYM	-	PIV	Repeat of 14 m/s
	18	0°	ASYM	-	PIV	GCM ASYM 18 0
14	10	-8°	ASYM	-	PIV	GCM ASYM 10 -8°
	14	-8°	ASYM	-	PIV	GCM ASYM 14 -8°
	15	-8°	ASYM	-	PIV	GCM ASYM 15 -8°
	18	-8°	ASYM	-	PIV	GCM ASYM 18 -8°
15	0-5-10-12-14-15-18-20-25-0	-8°	ASYM	-	-	
16	0-5-10-12-14-15-18-20-25-0	8°	ASYM	-	-	
17	10	8°	ASYM	-	PIV	GCM ASYM 10 8°
	14	8°	ASYM	-	PIV	GCM ASYM 14 8°
	15	8°	ASYM	-	PIV	GCM ASYM 15 8°
	18	8°	ASYM	-	PIV	GCM ASYM 18 8°
18	10	-8°	ASYM	-	PIV	Repeat of 10°m/s -8° yaw
19	0-5-10-12-14-15-18-20-25-0	0°		-	-	Disassembled
20	0-5-10-12-14-15-18-20-25-0	-8°		-	-	Disassembled
21	0-5-10-12-14-15-18-20-25-0	8°		-	-	Disassembled
22	0-5-10-12-14-15-18-20-25-0	8°	ASYM	-	-	
23	0-25-20-18-15-14-12-10-5-0	8°	ASYM	-	-	Opposite velocity for hysteresis
24	0-5-10-12-14-15-18-20-25-0	8°	ASYM	-	-	Seeder turned on with helium bubbles
25	0-5-10-12-14-15-18-20-25-0	0°	ASYM	-	-	Seeder turned on with helium bubbles
26	0-5-10-12-14-15-18-20-25-0	0°	ASYM	-	-	(seeder turned on air)
27	0-25-20-18-15-14-12-10-5-0	0°	ASYM	-	-	Opposite velocity for hysteresis
28	0-5-10-12-14-15-18-20-25-0	-8°	ASYM	-	-	Seeder turned on with helium bubbles
29	0-5-10-12-14-15-18-20-25-0	-8°	ASYM	-	-	(seeder turned on air)
30	0-25-20-18-15-14-12-10-5-0	-8°	ASYM	-	-	Opposite velocity for hysteresis
31	0-5-10-12-14-15-18-20-25-0	-8°	ASYM	-	-	Paint removed from GCM
32	0-5-10-12-14-15-18-20-25-0	0°	ASYM	-	-	No paint
33	0-5-10-12-14-15-18-20-25-0	8°	ASYM	-	-	No paint
34	0-5-10-12-14-15-18-20-25-0	0°	SYM	-	-	Rotation table failed during the run
35	0-5-10-12-14-15-18-20-25-0	0°	SYM	-	-	

36	0-5-10-12-14-15-18-20-25-0	-2°	SYM	-	-	
37	0-5-10-12-14-15-18-20-25-0	-4°	SYM	-	-	
38	0-5-10-12-14-15-18-20-25-0	-6°	SYM	-	-	
39	0-5-10-12-14-15-18-20-25-0	-8°	SYM	-	-	
40	0-5-10-12-14-15-18-20-25-0	-10°	SYM	-	-	
41	0-5-10-12-14-15-18-20-25-0	-15°	SYM	-	-	Tape on right arm was loose
42	0-5-10-12-14-15-18-20-25-0	-20°	SYM	-	-	
43	0-5-10-12-14-15-18-20-25-0	2°	SYM	-	-	
44	0-5-10-12-14-15-18-20-25-0	4°	SYM	-	-	
45	0-5-10-12-14-15-18-20-25-0	6°	SYM	-	-	
46	0-5-10-12-14-15-18-20-25-0	8°	SYM	-	-	
47	0-5-10-12-14-15-18-20-25-0	10°	SYM	-	-	
48	0-5-10-12-14-15-18-20-25-0	15°	SYM	-	-	
49	0-5-10-12-14-15-18-20-25-0	20°	SYM	-	-	
50	10	0°	SYM	-	PIV	GCM SYM 10 0
	14	0°	SYM	-	PIV	GCM SYM 14 0
	18	0°	SYM	-	PIV	GCM SYM 18 0
51	0-5-10-12-14-15-18-20-25-0	0°	SYM	-	-	Repeat of RUN 35
52	0-25-20-18-15-14-12-10-5-0	0°	SYM	-	-	Opposite velocity for hysteresis
53	10	-8°	SYM	-	PIV	GCM SYM 10 -8°
	14	-8°	SYM	-	PIV	GCM SYM 14 -8°
	18	-8°	SYM	-	PIV	GCM SYM 18 -8°
54	14	-6°	SYM	-	PIV	GCM SYM 14 -6°
55	0-5-10-12-14-15-18-20-25-0	-8°	SYM	-	-	Repeat of RUN 39
56	14	-4°	SYM	-	PIV	GCM SYM 14 -4°
57	14	4	SYM	-	PIV	GCM SYM 14 4°
58	14	6°	SYM	-	PIV	GCM SYM 14 6°
59	10	8°	SYM	-	PIV	GCM SYM 10 8°
	14	8°	SYM	-	PIV	GCM SYM 14 8°
	18	8°	SYM	-	PIV	GCM SYM 18 8°
60	0-5-10-12-14-15-18-20-25-0	0°		-	-	Disassembled
61	0-5-10-12-14-15-18-20-25-0	-2°		-	-	Disassembled
62	0-5-10-12-14-15-18-20-25-0	-4°		-	-	Disassembled
63	0-5-10-12-14-15-18-20-25-0	-6°		-	-	Disassembled
64	0-5-10-12-14-15-18-20-25-0	-8°		-	-	Disassembled
65	0-5-10-12-14-15-18-20-25-0	-10°		-	-	Disassembled
66	0-5-10-12-14-15-18-20-25-0	-15°		-	-	Disassembled
67	0-5-10-12-14-15-18-20-25-0	-20°		-	-	Disassembled
68	0-5-10-12-14-15-18-20-25-0	2°		-	-	Disassembled
69	0-5-10-12-14-15-18-20-25-0	4		-	-	Disassembled
70	0-5-10-12-14-15-18-20-25-0	6°		-	-	Disassembled
71	0-5-10-12-14-15-18-20-25-0	8°		-	-	Disassembled
72	0-5-10-12-14-15-18-20-25-0	10°		-	-	Disassembled
73	0-5-10-12-14-15-18-20-25-0	15°		-	-	Disassembled
74	0-5-10-12-14-15-18-20-25-0	20°		-	-	Disassembled
75	0-5-10-12-14-15-18-20-25-0	0°	SYM	-	-	
	14	0°	SYM	-	FlowVis	
	18	0°	SYM	-	FlowVis	
76	0-5-10-12-14-15-18-20-25-0	0°	SYM	VG 1.3mm	-	
77	0-5-10-12-14-15-18-20-25-0	-8°	SYM	VG 1.3mm	-	
78	0-5-10-12-14-15-18-20-25-0	8°	SYM	VG 1.3mm	-	
79	0-5-10-12-14-15-18-20-25-0	0°	SYM	-	-	
80	0-5-10-12-14-15-18-20-25-0	0°	SYM	VG 2.5mm	-	
81	0-5-10-12-14-15-18-20-25-0	-8°	SYM	VG 2.5mm	-	
82	0-5-10-12-14-15-18-20-25-0	8°	SYM	VG 2.5mm	-	
83	0-5-10-12-14-15-18-20-25-0	0°	SYM	VG 3.8mm	-	
84	0-5-10-12-14-15-18-20-25-0	-8°	SYM	VG 3.8mm	-	
85	0-5-10-12-14-15-18-20-25-0	8°	SYM	VG 3.8mm	-	
86	0-5-10-12-14-15-18-20-25-0	0°	SYM	Zigzag arms		
87	0-5-10-12-14-15-18-20-25-0	-8°	SYM	Zigzag arms		
88	0-5-10-12-14-15-18-20-25-0	8°	SYM	Zigzag arms		
89	0-5-10-12-14-15-18-20-25-0	10°	SYM	-	-	Reynolds-yaw corrections
90	0-5-10-12-14-15-18-20-25-0	15°	SYM	-	-	Reynolds-yaw corrections
91	0-5-10-12-14-15-18-20-25-0	20°	SYM	-	-	Reynolds-yaw corrections
92	0-5-10-12-14-15-18-20-25-0	-10°	SYM	-	-	Reynolds-yaw corrections
93	0-5-10-12-14-15-18-20-25-0	-15°	SYM	-	-	Reynolds-yaw corrections
94	0-5-10-12-14-15-18-20-25-0	-20°	SYM	-	-	Reynolds-yaw corrections
95	0-5-10-12-14-15-18-20-25-0	0°	SYM	Zigzag upper leg	-	
96	0-5-10-12-14-15-18-20-25-0	0°	SYM	Zigzag lower leg		
97	0-5-10-12-14-15-18-20-25-0	-8°	SYM	Zigzag lower leg		
98	0-5-10-12-14-15-18-20-25-0	8°	SYM	Zigzag lower leg		

99	14	0°	SYM	Zigzag lower leg	PIV	GCM SYM 14 0° zigzagLeg
	18	0°	SYM	Zigzag lower leg	PIV	GCM SYM 18 0° zigzagLeg
100	14	8°	SYM	Zigzag lower leg	PIV	GCM SYM 14 8° zigzagLeg
	18	8°	SYM	Zigzag lower leg	PIV	GCM SYM 18 8° zigzagLeg
101	14	0°	SYM	Zigzag arms	PIV	GCM SYM 14 0° zigzagArm
	18	0°	SYM	Zigzag arms	PIV	GCM SYM 18 0° zigzagArm
102	14	8°	SYM	Zigzag arms	PIV	GCM SYM 14 8° zigzagArm
	18	8°	SYM	Zigzag	PIV	GCM SYM 18 8° zigzagArm
103	0-5-10-12-14-15-18-20-25-0	0°	SYM	VG 3.8mm #2	-	
104	0-5-10-12-14-15-18-20-25-0	0°	SYM	VG 3.8mm #3	-	

B

Detailed Corrections and Uncertainty Results

This appendix entails a more detailed presentation of the crosswind correction and the uncertainty or error during the experiment.

B.1. Crosswind correction

The Reynolds number - Crosswind correction is performed at the highest three angles, both positive and negative. The velocity required for each of the angles is given in Table B.1. The difference in drag area caused by the correction is given in Table B.2 for each angle at each velocity.

Table B.1: The airflow velocity required for the Reynolds number - Crosswind correction for the highest crosswind angles

	Input Velocity $[m/s]$							
Crosswind	5	10	12	14	15	18	20	25
$0°$ *	4.7	9.4	11.3	14.0	15.0	16.9	18.6	22.6
$\pm 10°$	4.8	9.6	11.5	14.2	15.2	17.2	18.9	23.0
$\pm 15°$	4.9	9.7	11.7	14.5	15.5	17.5	19.3	23.4
$\pm 20°$	5.0	10.0	12.0	14.9	16.0	18.0	19.8	24.1

*The airflow velocity of the reference run

Table B.2: The difference due to Reynolds number - Crosswind correction

	Input Velocity $[m/s]$							
Crosswind	5	10	12	14	15	18	20	25
$-20°$	2.0%	0.1%	-2.1%	-2.0%	-1.1%	-0.8%	0.2%	-1.1%
$-15°$	2.7%	-0.8%	-0.8%	-1.1%	0.6%	-0.4%	-1.4%	-0.9%
$-10°$	3.0%	1.5%	1.8%	1.6%	1.3%	1.1%	0.4%	0.6%
$10°$	2.3%	1.0%	1.5%	0.9%	0.9%	-1.9%	1.5%	1.9%
$15°$	1.2%	0.8%	1.2%	1.5%	1.0%	0.8%	0.8%	1.7%
$20°$	0.3%	1.6%	3.4%	1.6%	1.5%	1.4%	1.0%	-1.1%

The difference in Reynolds number sweep due to the corrections is plotted in Figure B.1 for both negative and positive angles. Note, the velocity in the plots is the input velocity, not the actual velocity in the wind tunnel, which is done to show the difference more clearly.

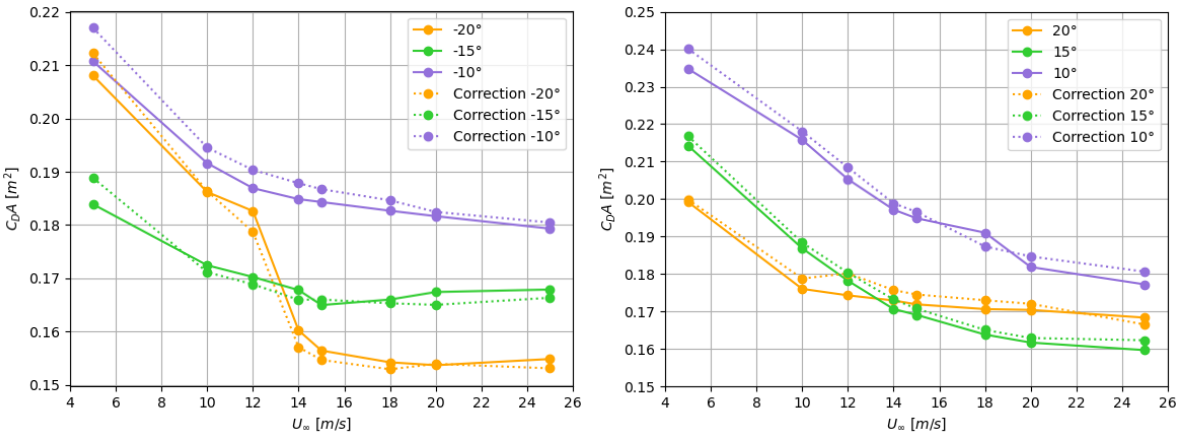

(a) Negative crosswind angles

(b) Positive crosswind angles

Figure B.1: The influence of the Reynolds number - Crosswind corrections on the Symmetric GCM at the highest negative and positive crosswind angles

The crosswind-C_DA curve at each velocity for the data with and without the Reynolds number - Crosswind corrections is plotted in Figure B.2.

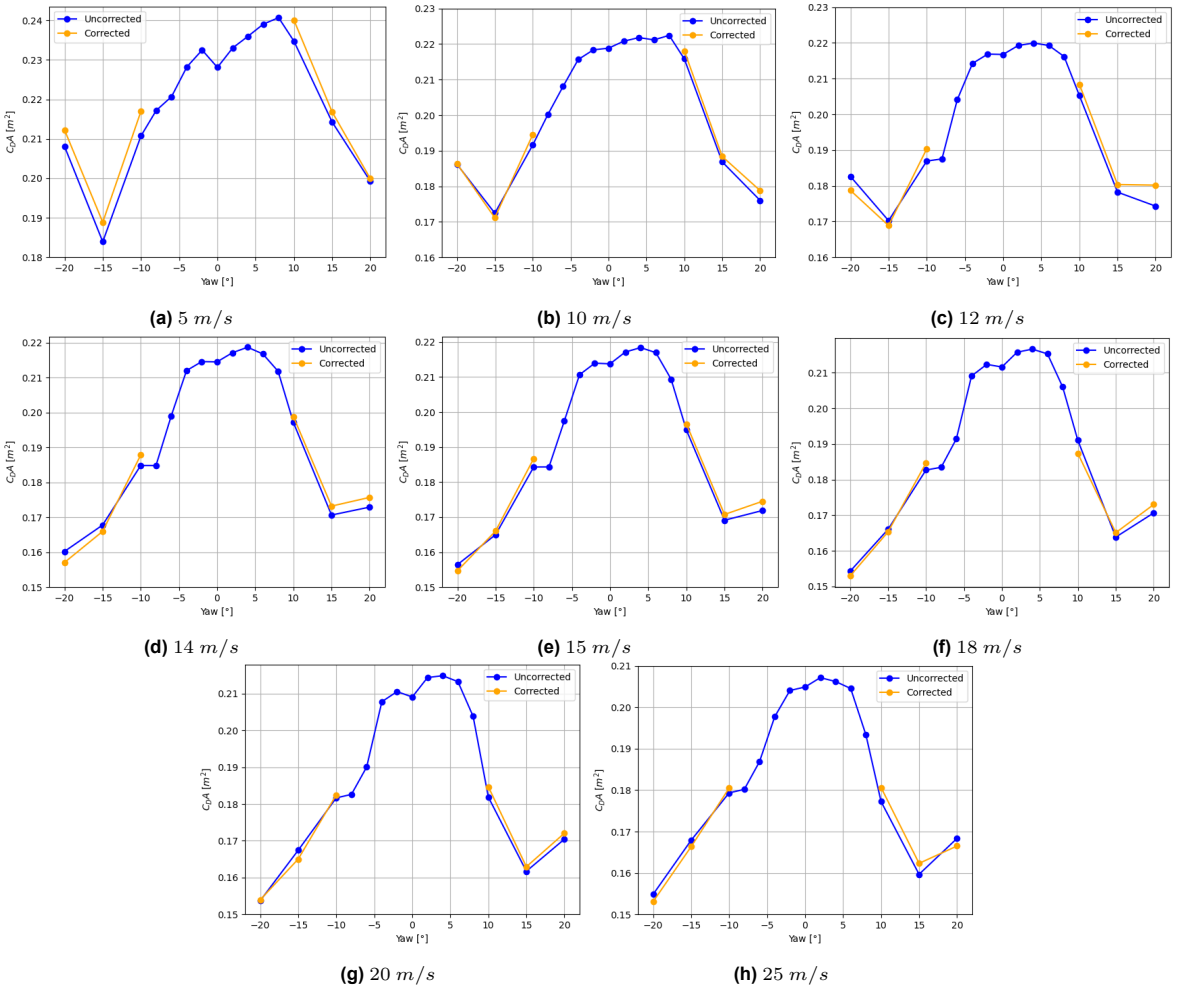

(a) $5\ m/s$ **(b)** $10\ m/s$ **(c)** $12\ m/s$

(d) $14\ m/s$ **(e)** $15\ m/s$ **(f)** $18\ m/s$

(g) $20\ m/s$ **(h)** $25\ m/s$

Figure B.2: The influence of the Reynolds number - Crosswind correction at each velocity for the Symmetric GCM

B.2. Velocity uncertainty

The actual velocity in the wind tunnel is lower than the velocity input into the OJF's system due to blockages in the meshes. The velocities of all the tests in the experiment have been measured and the difference or accuracy of the actual velocity compared to the input velocity has been calculated. Figure B.3 visualised the velocity accuracy of all the tests in the form of a boxplot.

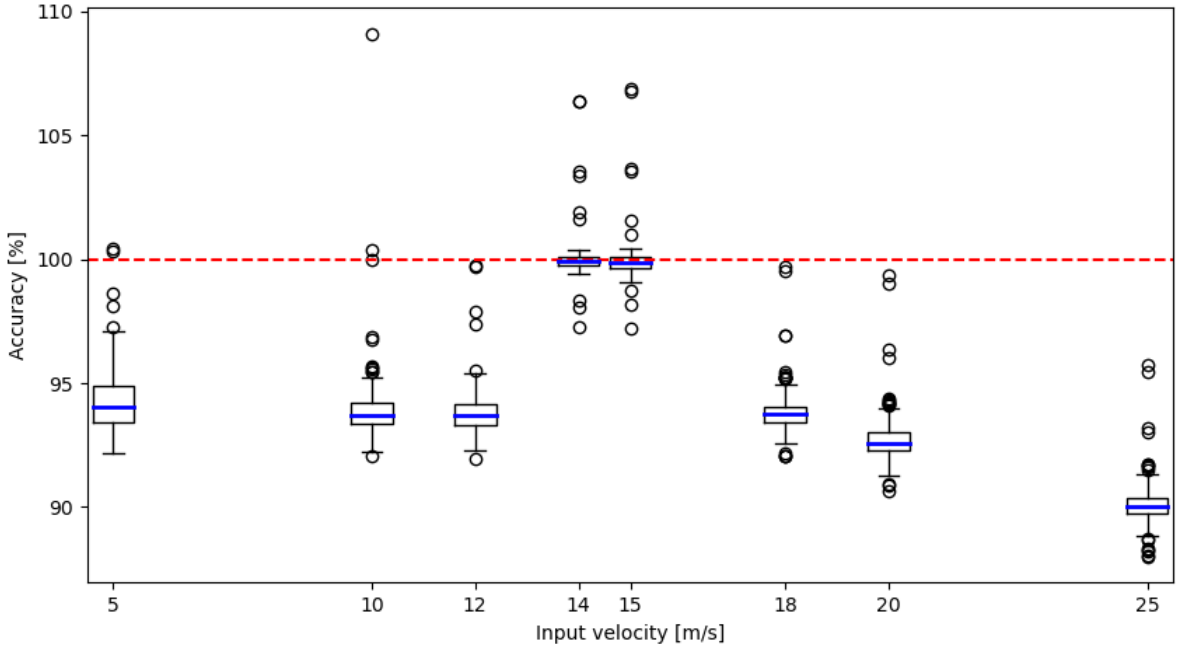

Figure B.3: Boxplot of the accuracy of the tested velocities

B.3. Difference between experiments of the Asymmetric GCM

The Asymmetric GCM has been tested four times prior, of which three times in the TU Delft OJF and once at Monash University in Australia. The drag area results per velocity has been plotted in Figure B.4.

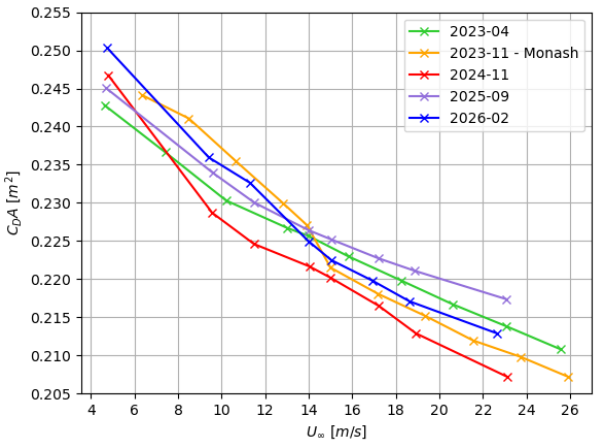

Figure B.4: Comparison of the drag area of the Asymmetric GCM between different experiments

B.4. Influence of the height of the fake floor

The fake floor can be elevated such that a distance is created with the nozzle exit. As the prior cross-wind experiment was performed at a height of $-2\ cm$, which is not preferred due to boundary-layer interactions. The first analysis of the Asymmetric GCM was performed at a height of $15\ cm$, thus this was tested as well. Both results are plotted in Figure B.5. The difference in drag area is noted down in Table B.3.

The fake floor height of $15\ cm$ leads to a higher drag area of approximately 4.5%. As no test runs were performed with the disassembled configuration at this height, the drag area increase can be linked to this. Meaning, that the fake floor itself leads to a higher drag area on the balance at higher heights, and it is not influenced by the GCM itself.

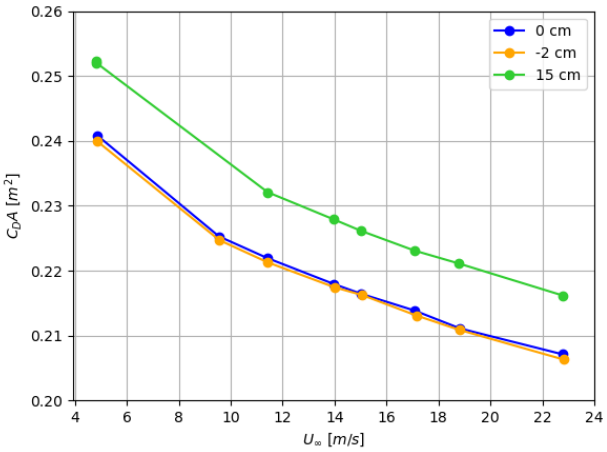

Figure B.5: Influence of the height of the fake floor above the nozzle exit on the drag area of the Asymmetric GCM

Table B.3: Difference between different fake floor heights compared to having the floor flush

	Input Velocity $[m/s]$							
Configuration	5	10	12	14	15	18	20	25
Floor at $-2\ cm$	-0.4%	-0.2%	-0.3%	-0.2%	-0.1%	-0.3%	-0.1%	-0.4%
Floor at $15\ cm$	4.7%	-*	4.6%	4.6%	4.5%	4.3%	4.7%	4.4%

* No measurement was performed at $10\ m/s$

B.5. Influence of the PIV seeder

The influence of the three PIV seeder configurations is plotted in Figure B.6. The error corresponding to the two configurations, seeder off and seeder on with HFSB, to the seeder turned on with air is giving Table B.4.

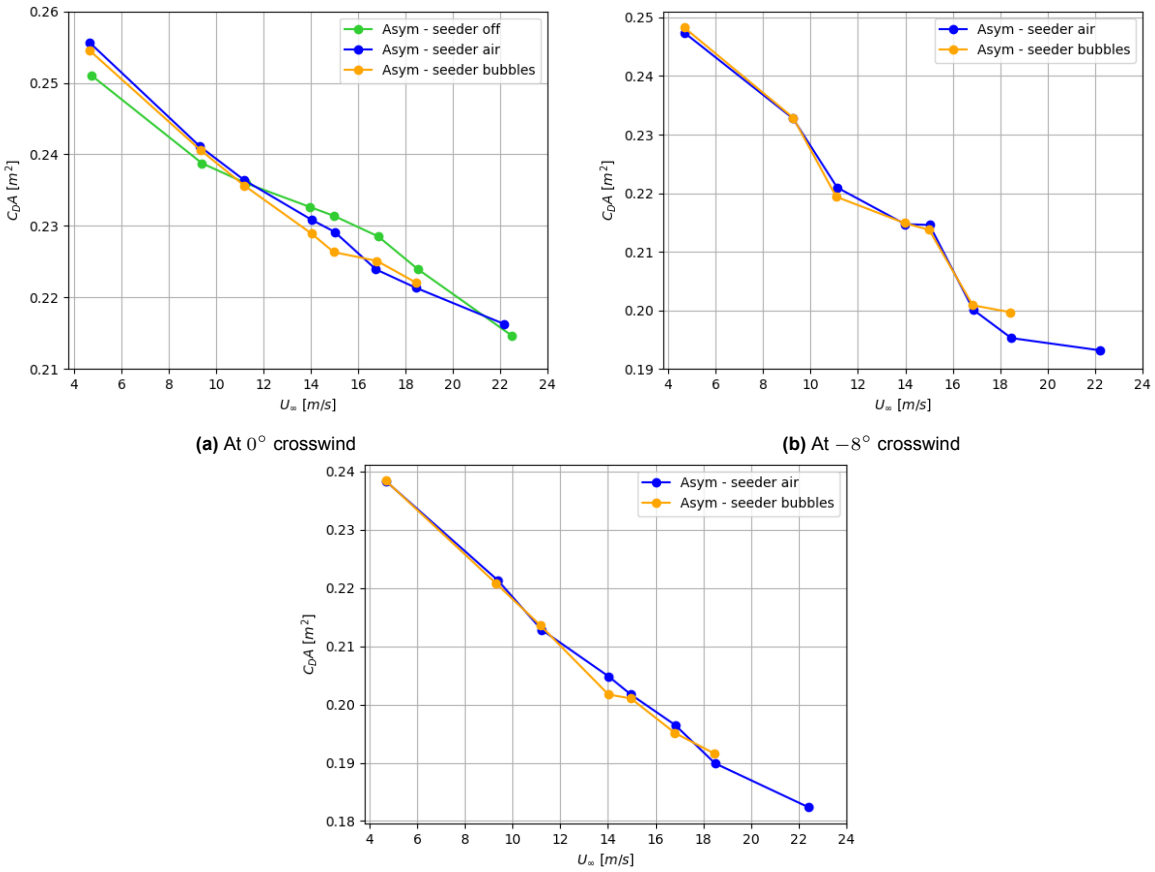

(a) At 0° crosswind

(b) At -8° crosswind

(c) At 8° crosswind

Figure B.6: Difference between the three options of the PIV seeder: turned off, turned on with air and turned on with HFSB. Comparing at different Reynolds numbers and crosswind angles for the Asymmetric GCM

Table B.4: Difference between the options of the PIV seeder compared to the seeder turned on with air for the Asymmetric GCM

	Input Velocity $[m/s]$							
Configuration	5	10	12	14	15	18	20	25
Seeder Off	-1.8%	-1.0%	-0.2%	0.8%	1.0%	2.1%	1.2%	-0.8%
Seeder on with HFSB	-0.4%	-0.2%	-0.3%	-0.8%	-1.2%	0.5%	0.3%	-*
Seeder on with HFSB - -8°	0.3%	0.1%	-0.7%	0.1%	-0.4%	0.4%	2.3%	-*
Seeder on with HFSB - 8°	0.0%	-0.2%	0.3%	-1.5%	-0.3%	-0.7%	0.9%	-*

* No measurements were performed with the HFSB at $25\ m/s$

B.6. Repeatability

The four repeatability cases for the Symmetric GCM: consecutive, non-consecutive, dismount-mount and hysteresis, are plotted in Figure B.7.

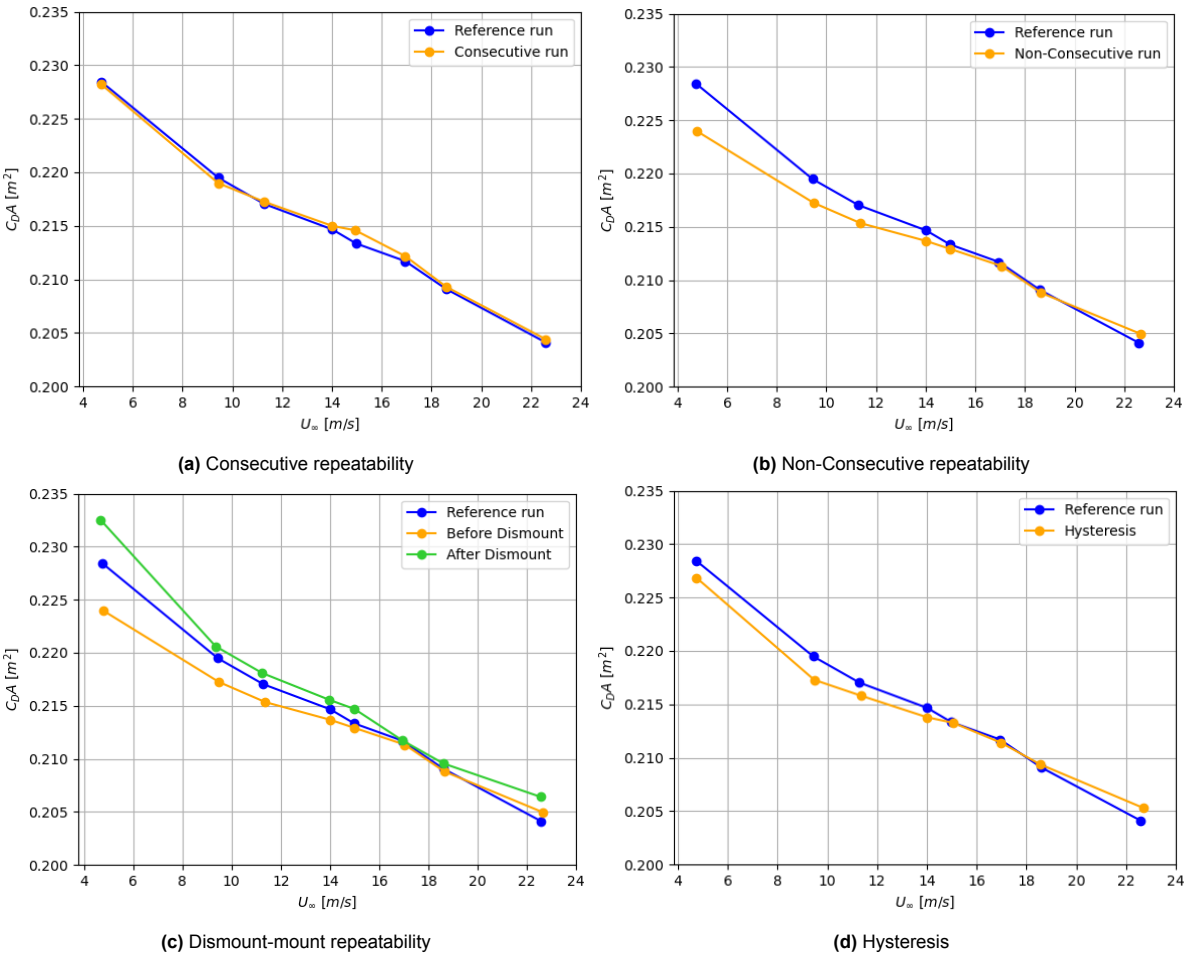

(a) Consecutive repeatability

(b) Non-Consecutive repeatability

(c) Dismount-mount repeatability

(d) Hysteresis

Figure B.7: Repeatability of the Symmetric GCM for the consecutive, non-consecutive, dismount-mount and hysteresis cases at 0° crosswind

B.7. Streamwise velocity standard Deviation

The standard deviation in the streamwise velocity in some of the conditions can be found in Figure B.8. As can be seen, some conditions have higher standard deviations than others. Especially the cases at $10\ m/s$, or at crosswind angle $8°$. When looking at the flow control devices, the zigzag strip on the legs leads to a higher deviation than the bare configuration, while the zigzag strip on the arms has a similar deviation to the bare configuration.

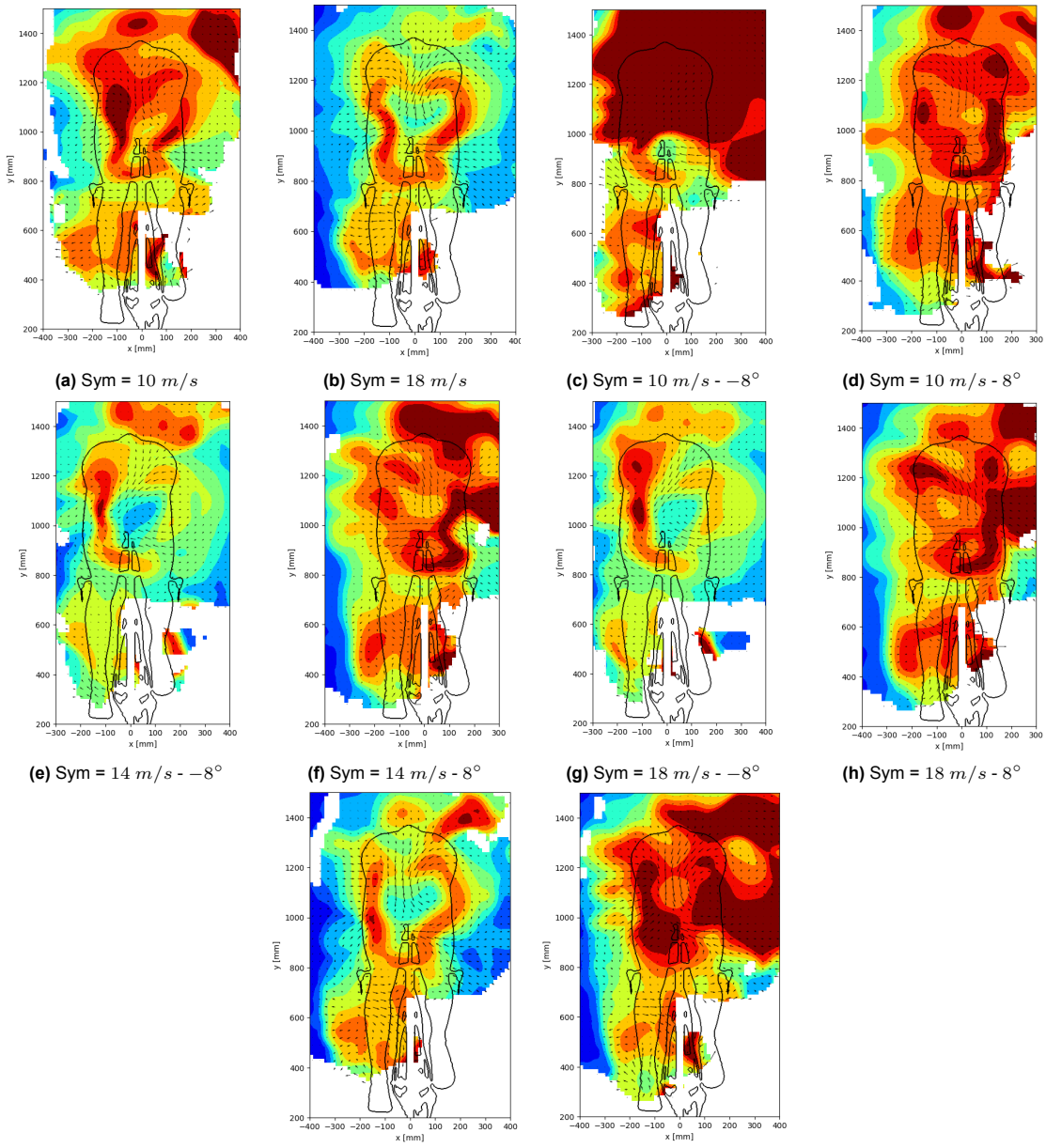

(a) Sym = $10\ m/s$ **(b)** Sym = $18\ m/s$ **(c)** Sym = $10\ m/s$ - $-8°$ **(d)** Sym = $10\ m/s$ - $8°$

(e) Sym = $14\ m/s$ - $-8°$ **(f)** Sym = $14\ m/s$ - $8°$ **(g)** Sym = $18\ m/s$ - $-8°$ **(h)** Sym = $18\ m/s$ - $8°$

(i) Sym = $14\ m/s$ - ZZ arms **(j)** Sym = $14\ m/s$ - ZZ legs

Figure B.8: Streamwise velocity standard deviation in different conditions of the Symmetric GCM

C

Detailed Results - Effect of Reynolds Number variation

This appendix gives extra details of the Reynolds number effect on the aerodynamic loads and flow fields of the Asymmetric and Symmetric GCM.

C.1. Aerodynamic Loads

The drag area of the Reynolds number effect against the Reynolds number instead of the velocity is plotted in Figure C.1. The values of the Reynolds number are used for the critical Reynolds number theory.

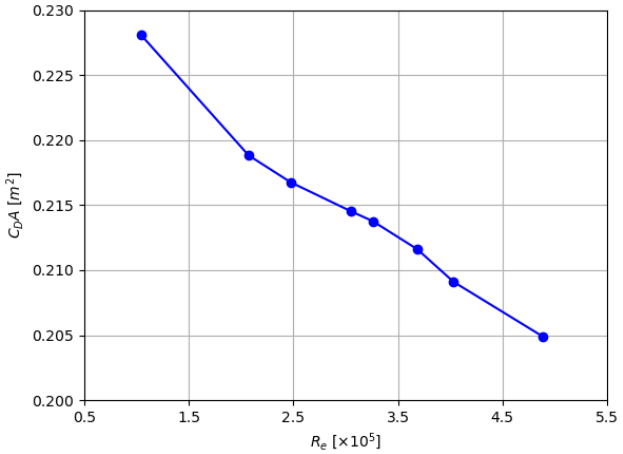

Figure C.1: Reynolds number effect on the drag area of the Symmetric GCM

C.2. Aerodynamic Flow Field

The lateral and vertical normalised velocity flow field of the Symmetric GCM at the velocities $10\ m/s$, $14\ m/s$ and $18\ m/s$ is visualised in Figure C.2.

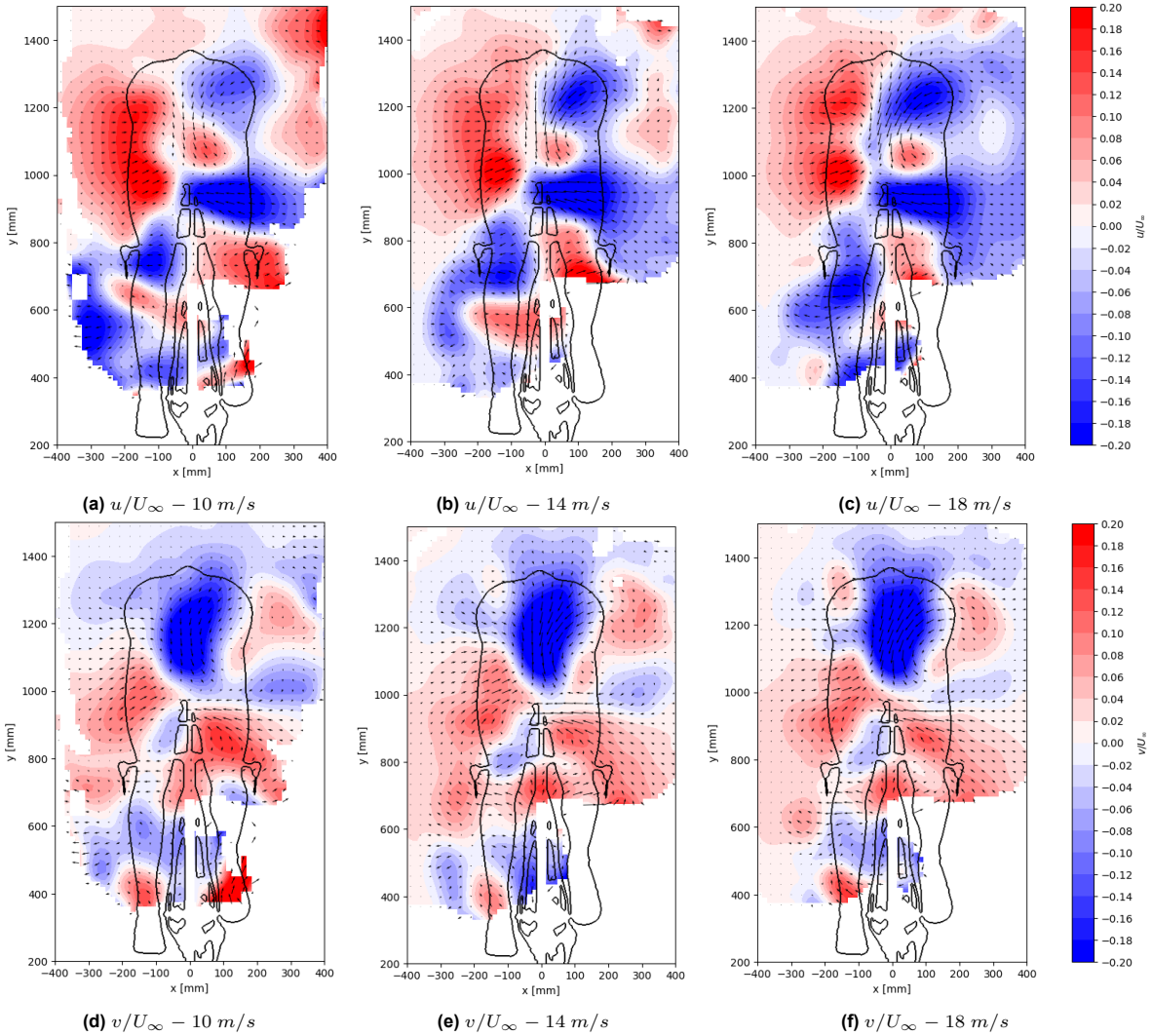

(a) $u/U_\infty - 10\ m/s$ **(b)** $u/U_\infty - 14\ m/s$ **(c)** $u/U_\infty - 18\ m/s$

(d) $v/U_\infty - 10\ m/s$ **(e)** $v/U_\infty - 14\ m/s$ **(f)** $v/U_\infty - 18\ m/s$

Figure C.2: The normalised lateral and vertical velocity flow field of the Symmetric GCM at different velocities

C.2.1. Comparison to Asymmetric GCM

The lateral and vertical velocity flow field of the Asymmetric GCM at the velocities $10\ m/s$, $14\ m/s$ and $18\ m/s$ is visualised in Figure C.3.

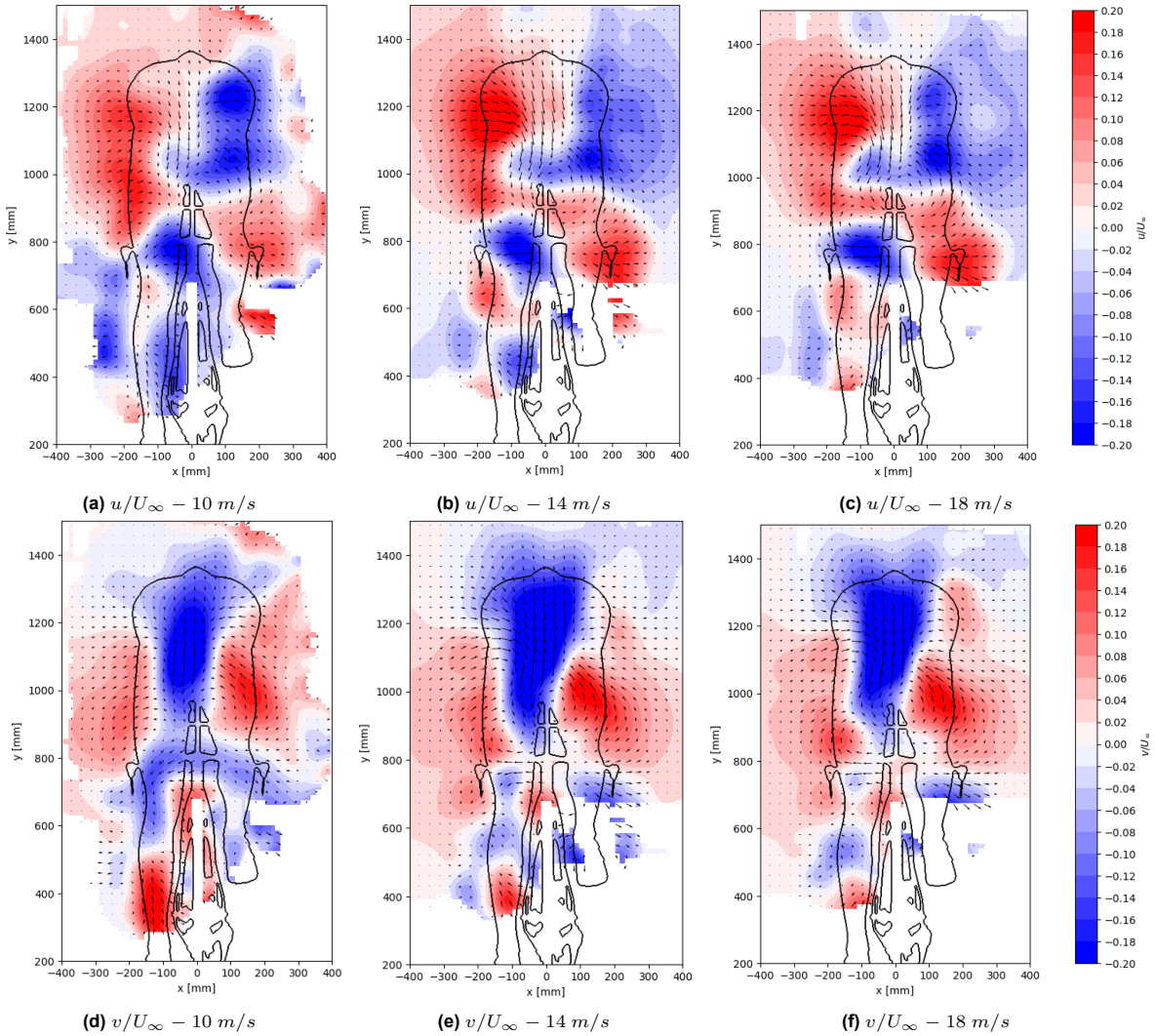

(a) $u/U_\infty - 10\ m/s$ **(b)** $u/U_\infty - 14\ m/s$ **(c)** $u/U_\infty - 18\ m/s$

(d) $v/U_\infty - 10\ m/s$ **(e)** $v/U_\infty - 14\ m/s$ **(f)** $v/U_\infty - 18\ m/s$

Figure C.3: The normalised lateral and vertical velocity flow field of the Asymmetric GCM at different velocities

The strength of the vortices of the Asymmetric GCM at the velocities $10\ m/s$, $14\ m/s$ and $18\ m/s$ is visualised by the Q-criterion in Figure C.4.

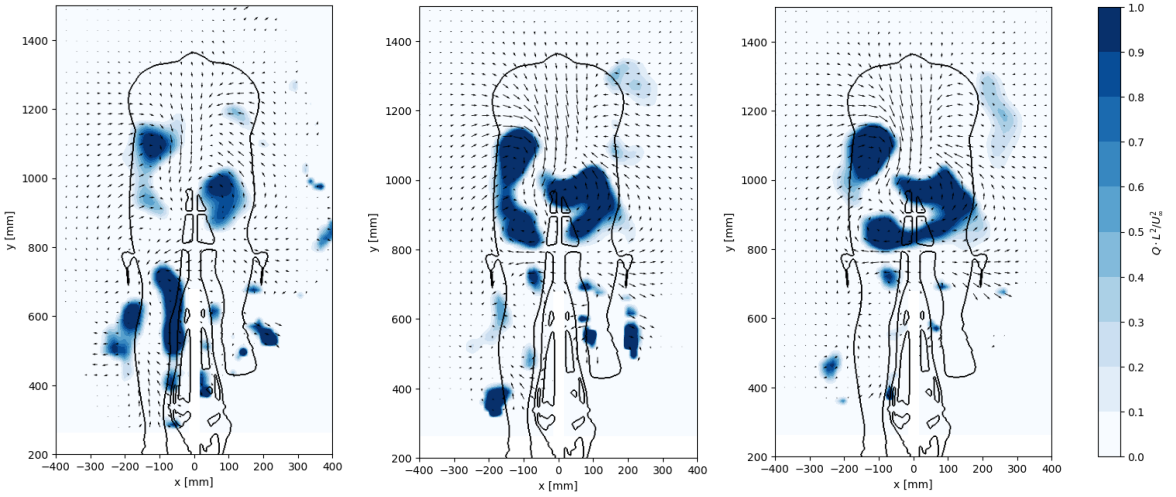

(a) $10\ m/s$ **(b)** $14\ m/s$ **(c)** $18\ m/s$

Figure C.4: The Q-criteria of the Asymmetric GCM at different velocities

D

Detailed Results - Effect of Crosswind

This appendix gives extra details of the crosswind effect on the aerodynamic loads and flow fields of the Asymmetric and Symmetric GCM.

D.1. Aerodynamic Loads

A direct comparison between positive and negative crosswind angles is given in Figure D.1. It can be seen that the negative angle results in a lower drag area than its corresponding positive angle. At the negative angle, the left leg, the straighter leg, is rotated into the oncoming airflow. At $\pm 15°$, a opposite in trend can be seen after a velocity of $15\ m/s$ as the negative angles lead to a higher drag area. Subsequently, $-20°$ leads to a higher drag area at velocities slower than $14\ m/s$.

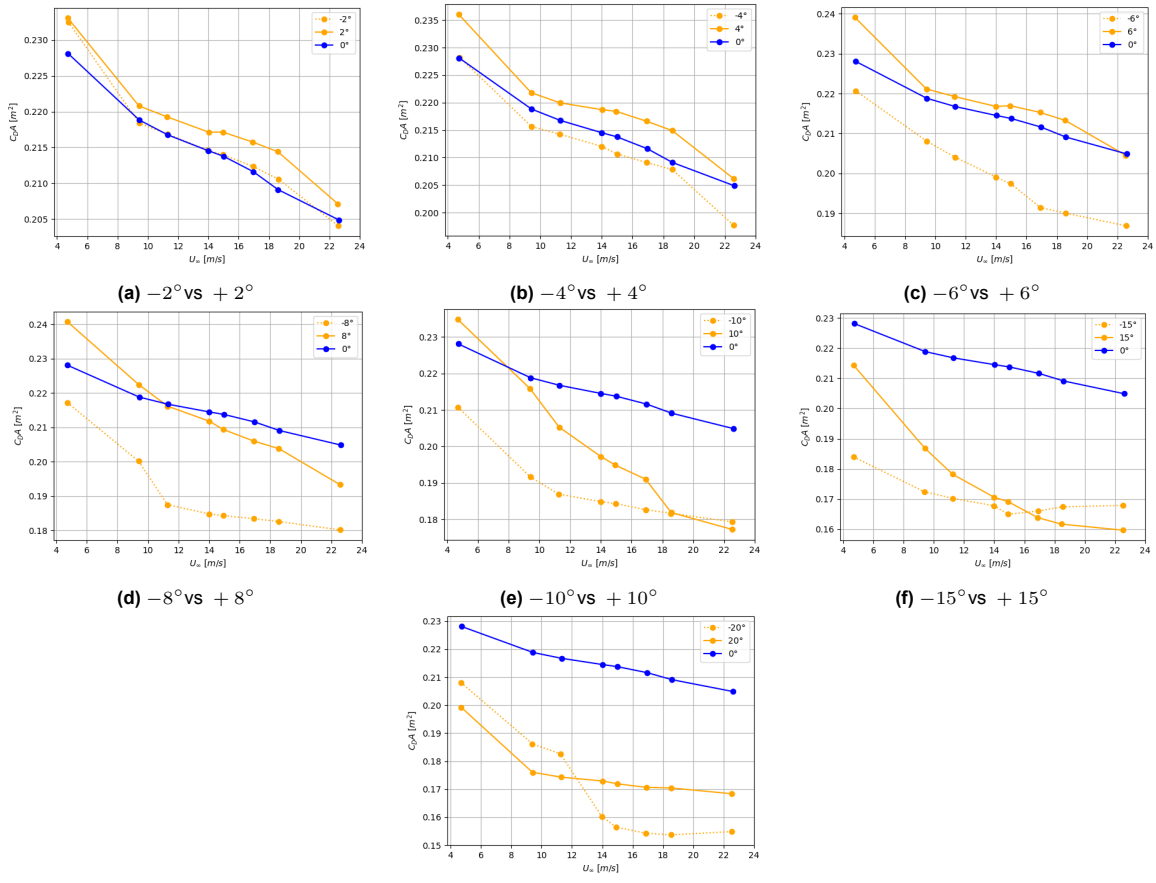

(a) $-2°$ vs $+2°$ **(b)** $-4°$ vs $+4°$ **(c)** $-6°$ vs $+6°$

(d) $-8°$ vs $+8°$ **(e)** $-10°$ vs $+10°$ **(f)** $-15°$ vs $+15°$

(g) $-20°$ vs $+20°$

Figure D.1: The comparison of negative to positive crosswind angle plotted against wind speed for the Symmetric GCM

D.2. Flow Field

The lateral and vertical velocity of the Symmetric GCM at $14\ m/s$ at the crosswind angles, $-8°$, $0°$ and $8°$ are given in Figure D.2. The lateral velocity fields indicate clear differences; similarly, the tilt in downwash is altered by the pressence of crosswind.

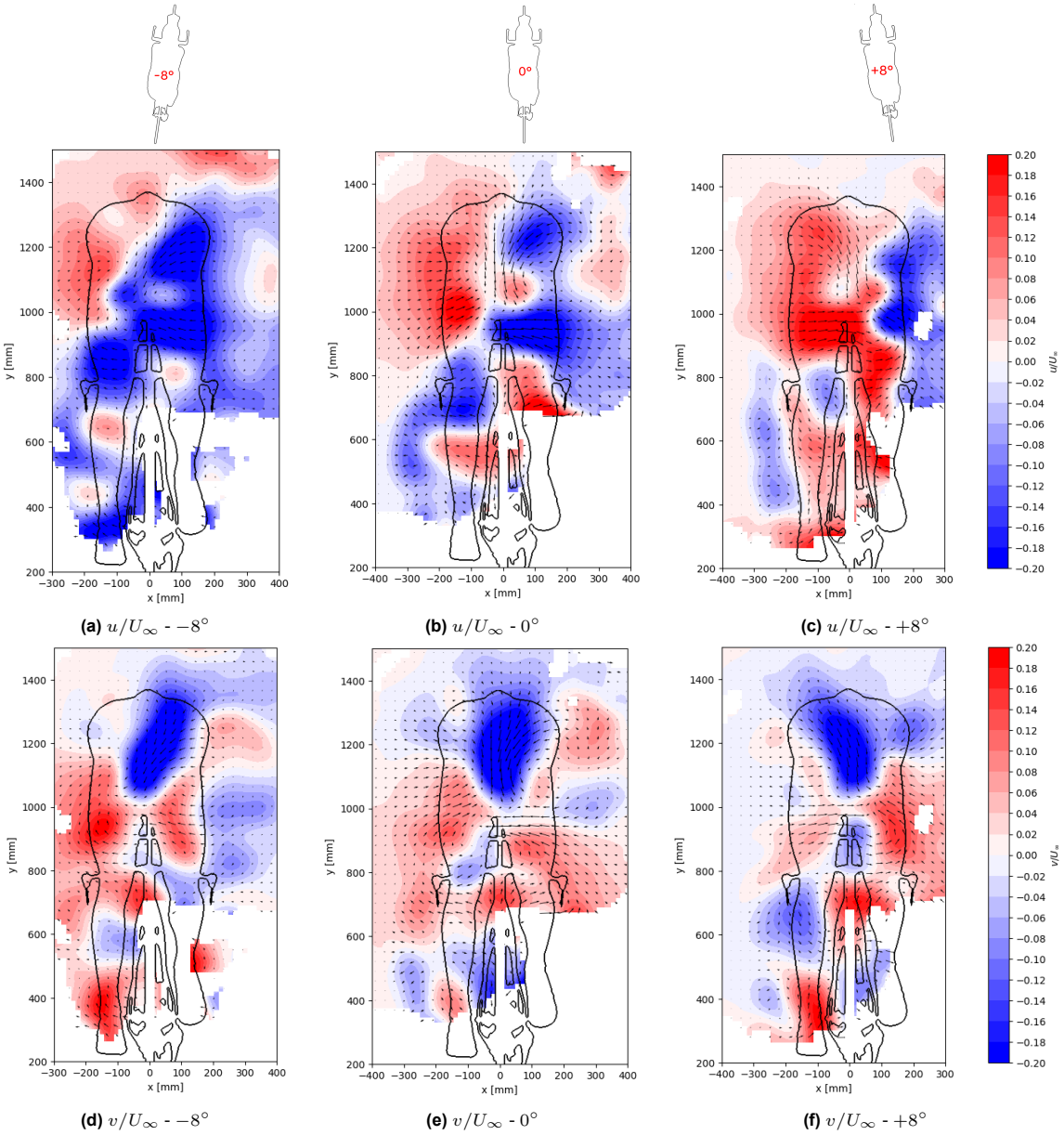

(a) u/U_∞ - $-8°$ **(b)** u/U_∞ - $0°$ **(c)** u/U_∞ - $+8°$

(d) v/U_∞ - $-8°$ **(e)** v/U_∞ - $0°$ **(f)** v/U_∞ - $+8°$

Figure D.2: The lateral and vertical velocity flow field of the Symmetric GCM at $-8°$, $0°$ and $8°$ crosswind angles at $14\ m/s$

Furthermore, the lateral and vertical velocity at the angles in between $\pm 8°$ are given in Figure D.3. These velocities are consistent with the behaviour observed at $-8°$ and $8°$.

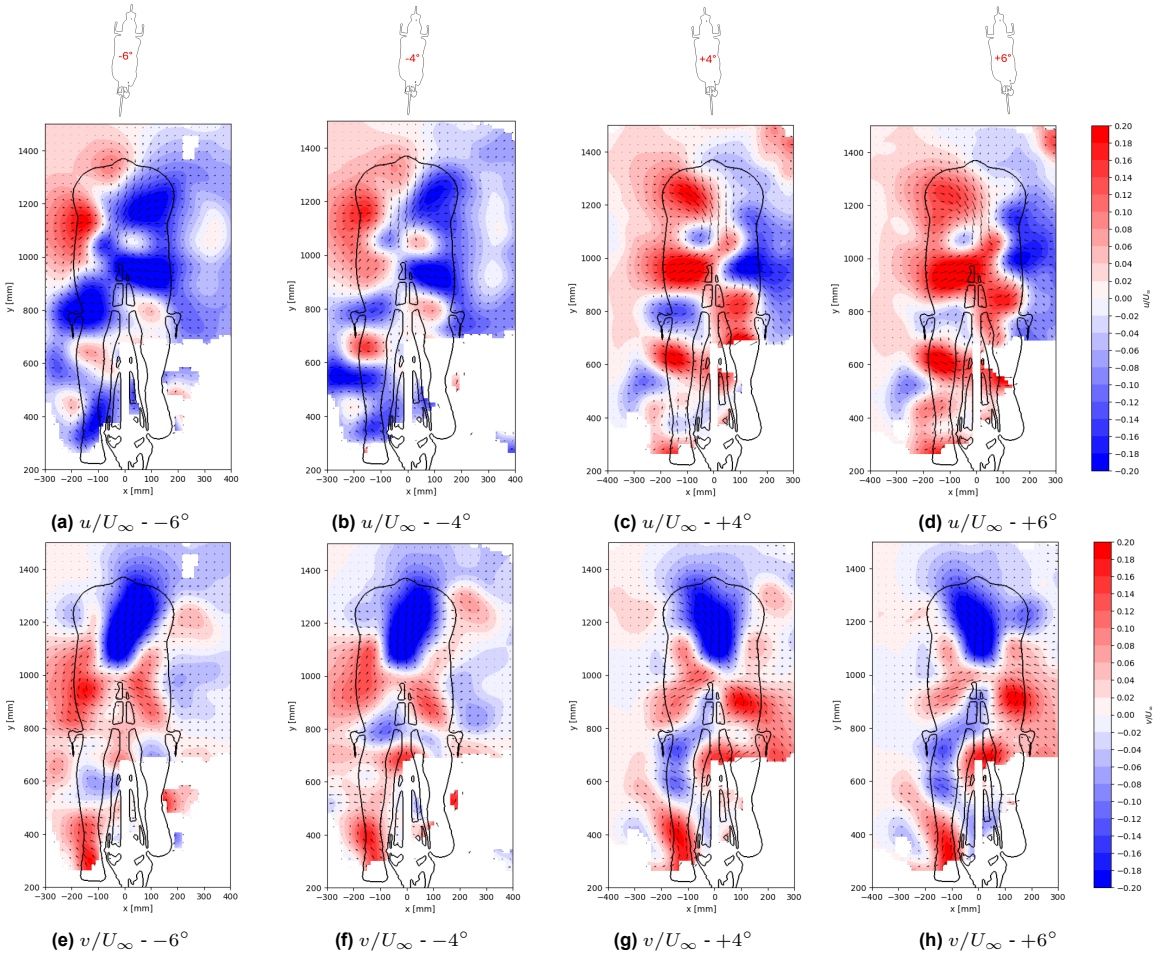

(a) u/U_∞ - $-6°$ **(b)** u/U_∞ - $-4°$ **(c)** u/U_∞ - $+4°$ **(d)** u/U_∞ - $+6°$

(e) v/U_∞ - $-6°$ **(f)** v/U_∞ - $-4°$ **(g)** v/U_∞ - $+4°$ **(h)** v/U_∞ - $+6°$

Figure D.3: The lateral and vertical velocity flow field of the Symmetric GCM at $-6°$, $-4°$, $4°$ and $8°$ crosswind angles at $14\ m/s$

The vorticity at the crosswind angles $\pm 4°$ and $\pm 6°$ is given in Figure D.4. The flow fields show similar behavioural trends to the extremes.

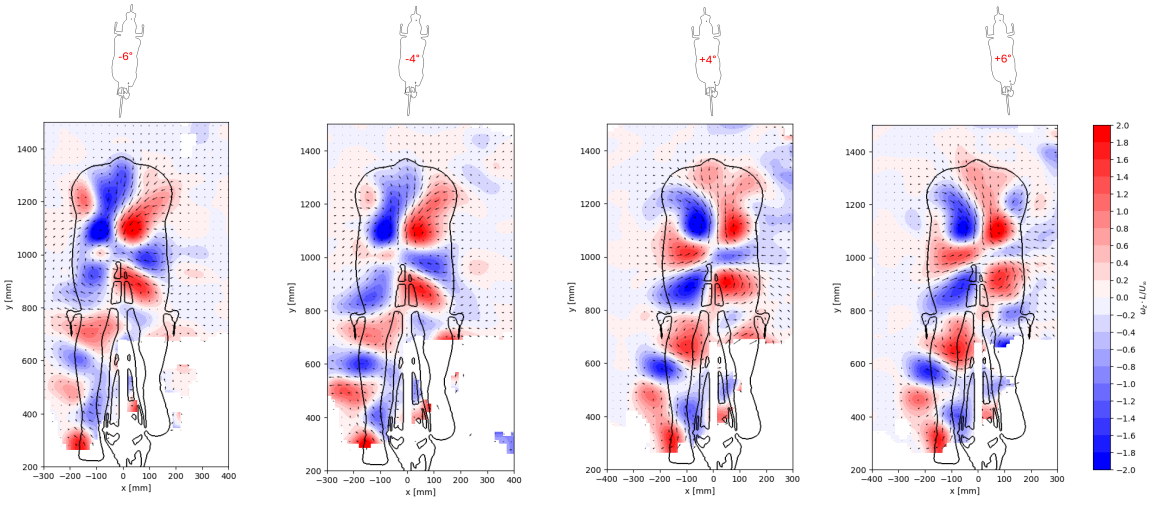

(a) u/U_∞ - $-6°$ **(b)** u/U_∞ - $-4°$ **(c)** u/U_∞ - $+4°$ **(d)** $u/U_\infty -$ $+6°$

Figure D.4: The streamwise vorticity flow field of the Symmetric GCM at $-6°$, $-4°$, $4°$ and $8°$ crosswind angles at $14\ m/s$

The Q-criterion at the crosswind angles $\pm 4°$ and $\pm 6°$ is given in Figure D.5. The strength changes are similar to those at $-8°$ and $8°$.

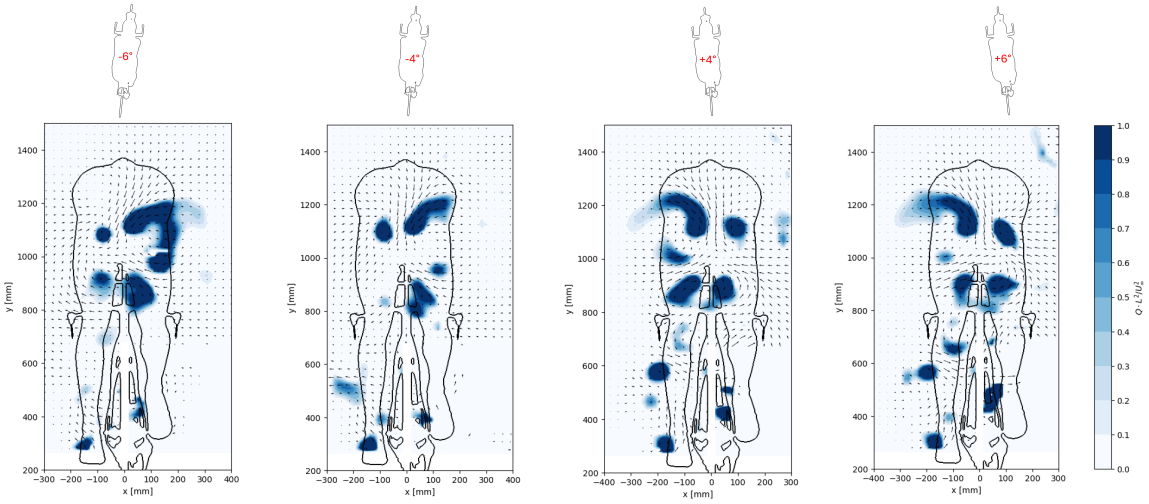

(a) u/U_∞ - $-6°$ **(b)** u/U_∞ - $-4°$ **(c)** u/U_∞ - $+4°$ **(d)** u/U_∞ - $+6°$

Figure D.5: The Q-criterion of the Symmetric GCM at $-6°$, $-4°$, $4°$ and $6°$ crosswind angles at $14\ m/s$

D.2.1. Comparison to Asymmetric GCM

The lateral and vertical velocities at the crosswind angles $-8°$, $0°$ and $8°$ for the Asymmetric GCM are given in Figure D.6.

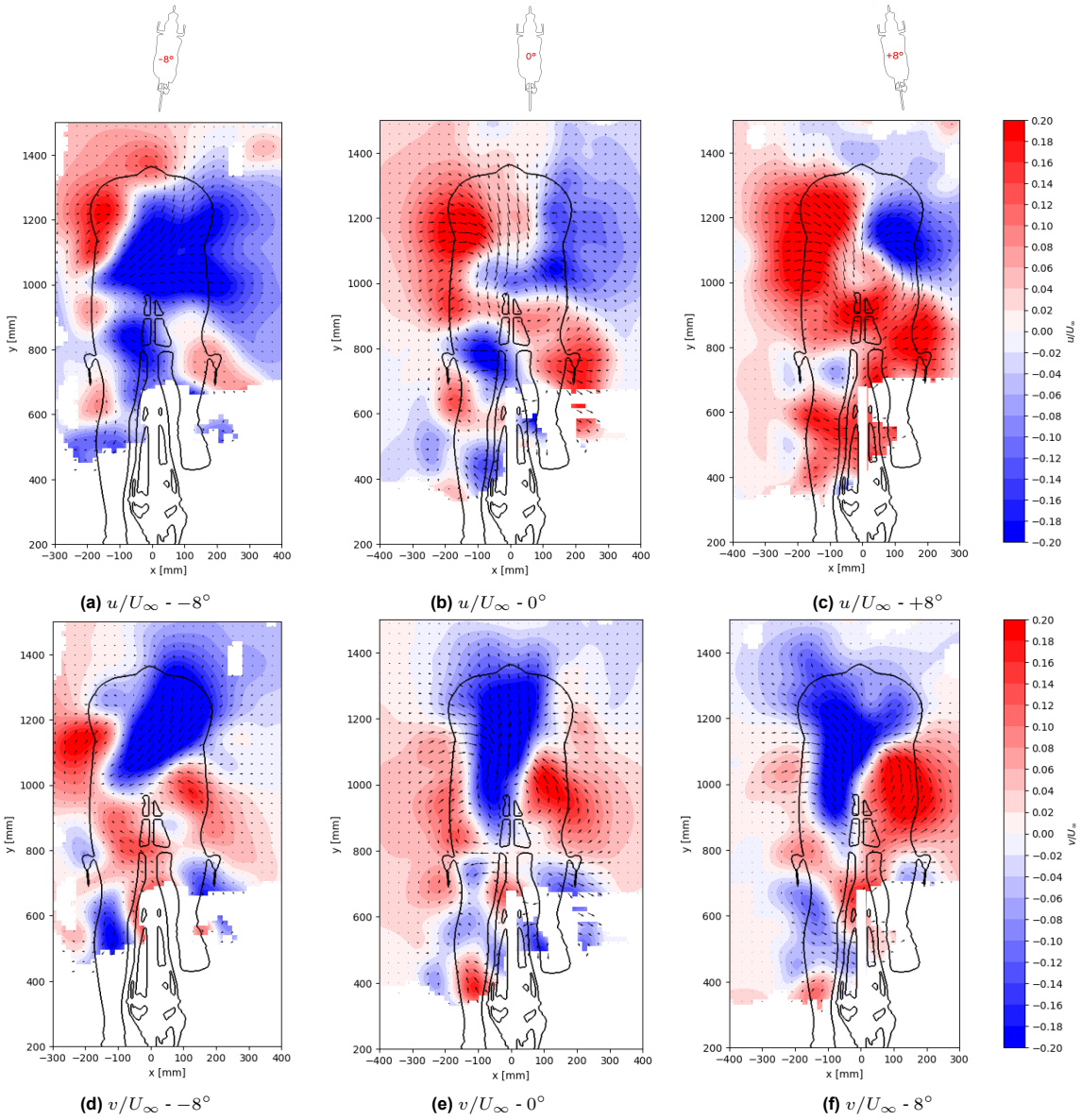

(a) u/U_∞ - $-8°$ **(b)** u/U_∞ - $0°$ **(c)** u/U_∞ - $+8°$

(d) v/U_∞ - $-8°$ **(e)** v/U_∞ - $0°$ **(f)** v/U_∞ - $8°$

Figure D.6: The lateral and vertical flow field of the Asymmetric GCM at $-8°$, $0°$ and $8°$ crosswind angles at $14\ m/s$

D.2.2. Influence of Reynolds number on the Crosswind Effect

The cross-comparison of the Reynolds number effect and the crosswind effect can be seen in Figure D.7 and Figure D.8.

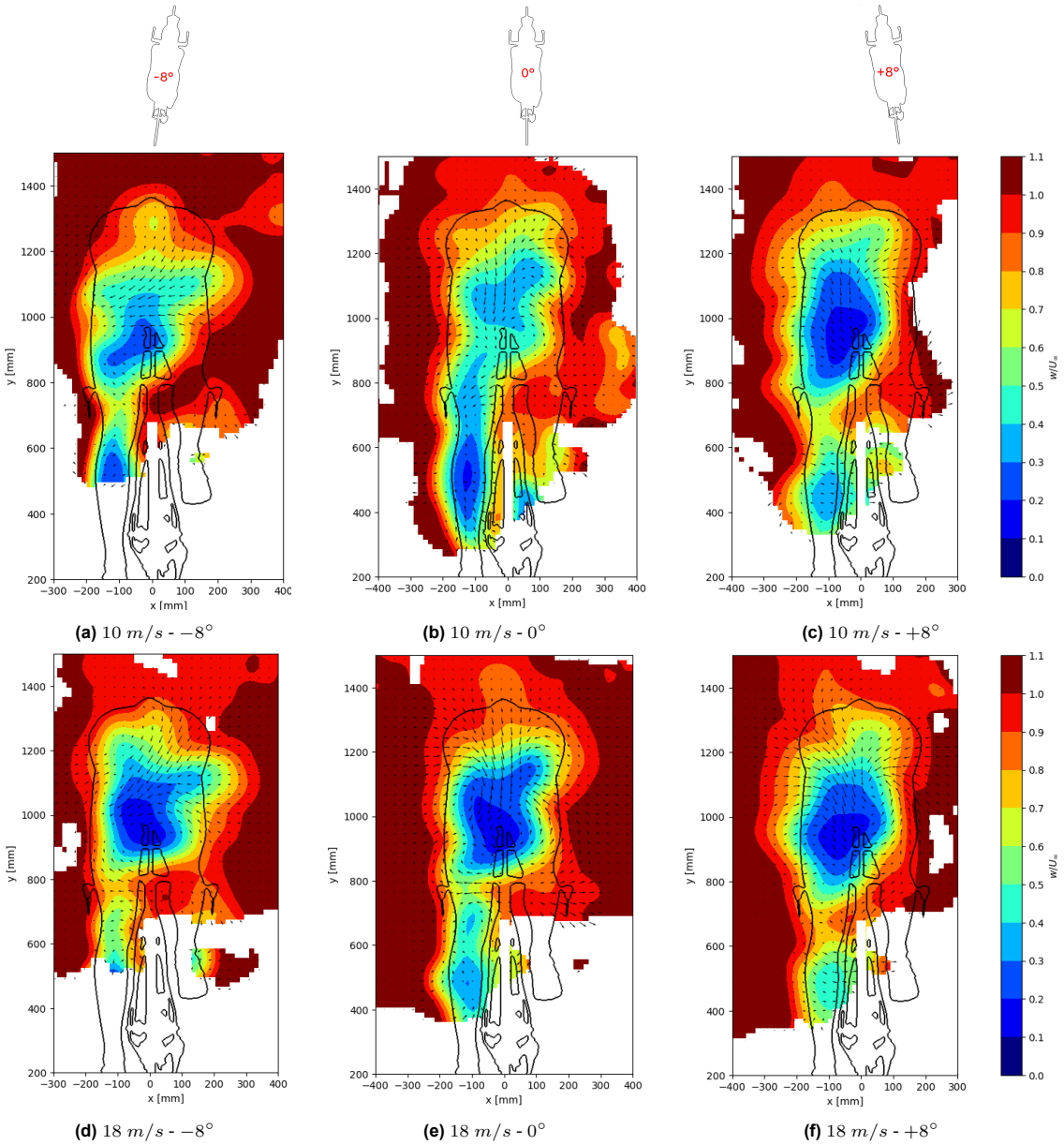

(a) $10\ m/s$ - $-8°$ **(b)** $10\ m/s$ - $0°$ **(c)** $10\ m/s$ - $+8°$

(d) $18\ m/s$ - $-8°$ **(e)** $18\ m/s$ - $0°$ **(f)** $18\ m/s$ - $+8°$

Figure D.7: The velocity flow field of the Asymmetric GCM at $-8°$ and $8°$ crosswind angles at $10\ m/s$ and $18\ m/s$

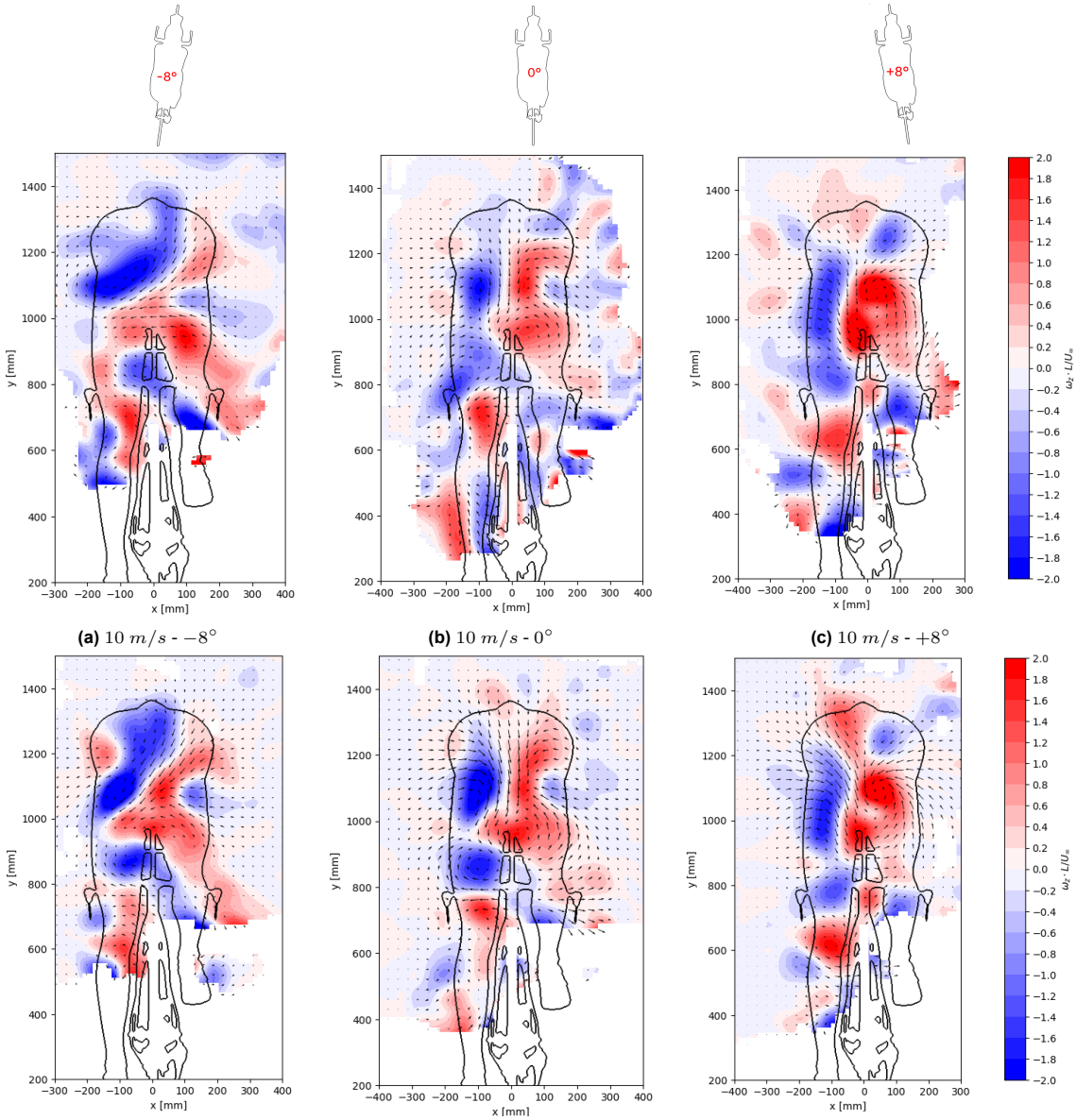

(a) $10\ m/s$ - $-8°$ **(b)** $10\ m/s$ - $0°$ **(c)** $10\ m/s$ - $+8°$

(d) $18\ m/s$ - $-8°$ **(e)** $18\ m/s$ - $0°$ **(f)** $18\ m/s$ - $+8°$

Figure D.8: The vorticity flow field of the Asymmetric GCM at $-8°$ and $8°$ crosswind angles at $10\ m/s$ and $18\ m/s$

E

Detailed Results - Effect of Flow Control Devices

This appendix gives extra details of the addition of flow control devices on the aerodynamic loads and flow fields of the Symmetric GCM.

E.1. Devices on the Arms

The changes in lateral and vertical velocity caused by the zigzag strip on the arms of the GCM are presented in Figure E.1 at $14\ m/s$

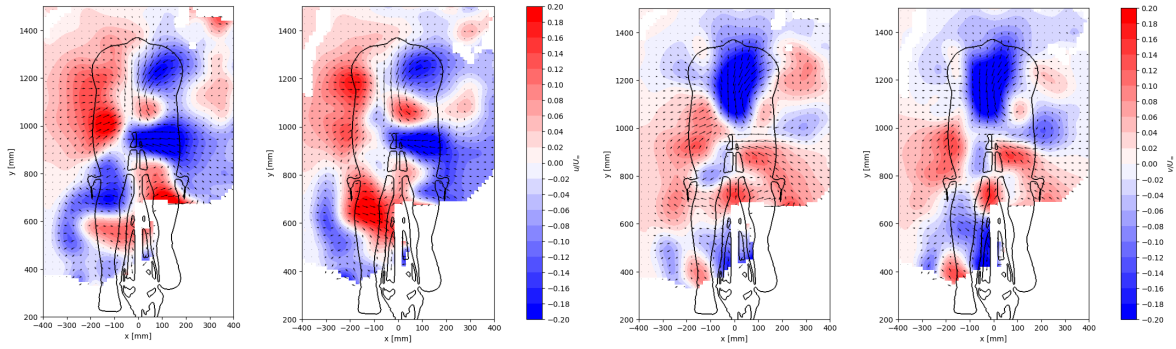

(a) Bare - u/U_∞ **(b)** Zigzag arms - u/U_∞ **(c)** Bare - v/U_∞ **(d)** Zigzag arms - v/U_∞

Figure E.1: The lateral and vertical velocity flow fields of the zigzag strip on the arms of the Symmetric GCM at $14\ m/s$

The effect on the strength of the vortices caused by the zigzag strips is visualised in Figure E.2.

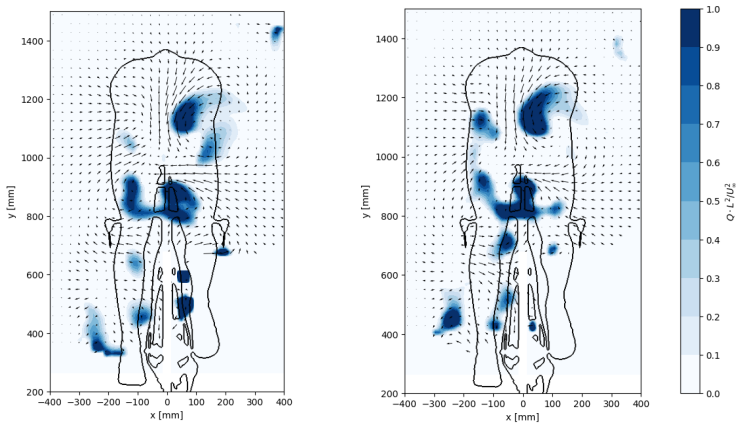

(a) Bare configuration **(b)** Zigzag on arms

Figure E.2: The effect of zigzag strips on the arms of the Symmetric GCM on the Q-criterion at $14\ m/s$

E.1.1. Reynolds Number Effect

The changes in lateral and vertical velocity caused by the zigzag strip on the arms of the GCM are presented in Figure E.3 at $18\ m/s$.

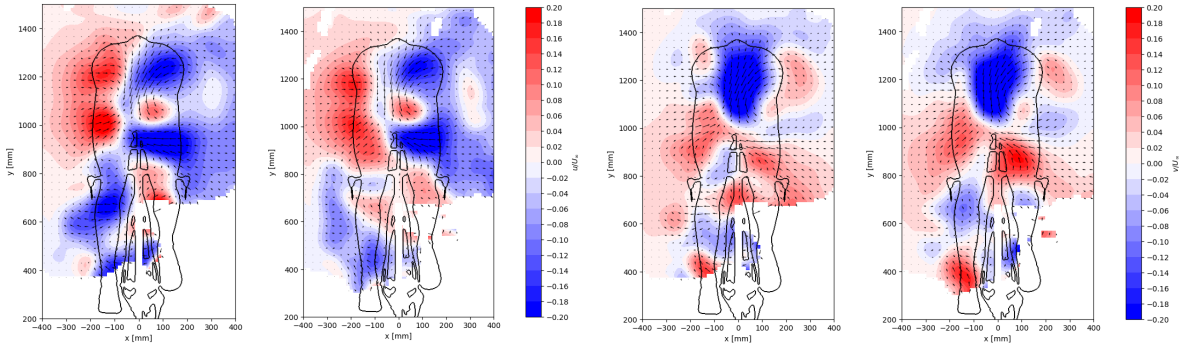

(a) Bare - u/U_∞ **(b)** Zigzag arms - u/U_∞ **(c)** Bare - v/U_∞ **(d)** Zigzag arms - v/U_∞

Figure E.3: The lateral and vertical velocity flow fields of the zigzag strip on the arms of the Symmetric GCM at $18\ m/s$

E.2. Devices on the Legs

The changes in lateral and vertical velocity caused by the zigzag strip on the lower legs of the Symmetric GCM are presented in Figure E.4 at $14m/s$.

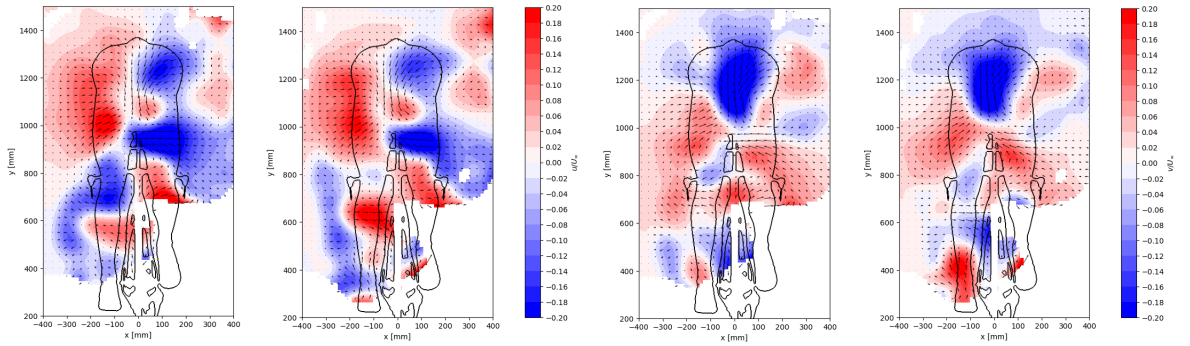

(a) Bare - u/U_∞ **(b)** Zigzag legs - u/U_∞ **(c)** Bare - v/U_∞ **(d)** Zigzag legs - v/U_∞

Figure E.4: The lateral and vertical velocity flow fields of the zigzag strip on the lower legs of the Symmetric GCM at $14\ m/s$

The effect on the strength of the vortices caused by the zigzag strips is visualised in Figure E.5.

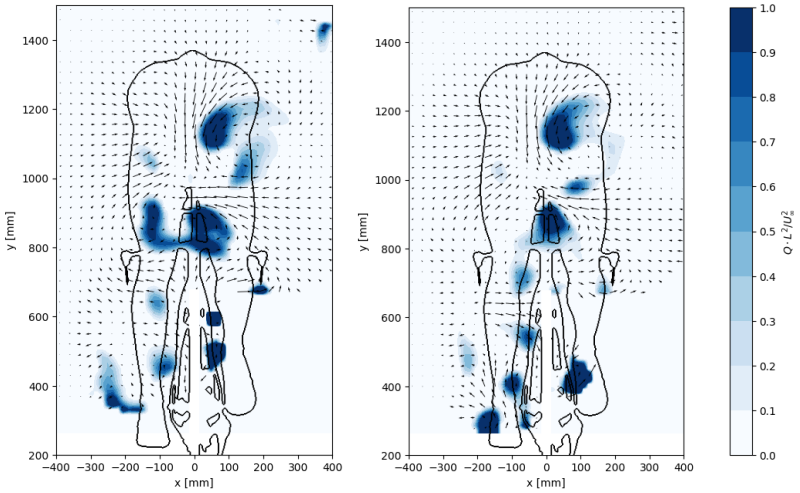

(a) Bare configuration **(b)** Zigzag on lower legs

Figure E.5: The effect of zigzag strips on the lower legs of the Symmetric GCM on the Q-criterion at $14\ m/s$

E.2.1. Reynolds Number Effect

The changes in lateral and vertical velocity caused by the zigzag strip on the lower legs of the Symmetric GCM are presented in Figure E.6 at $18m/s$.

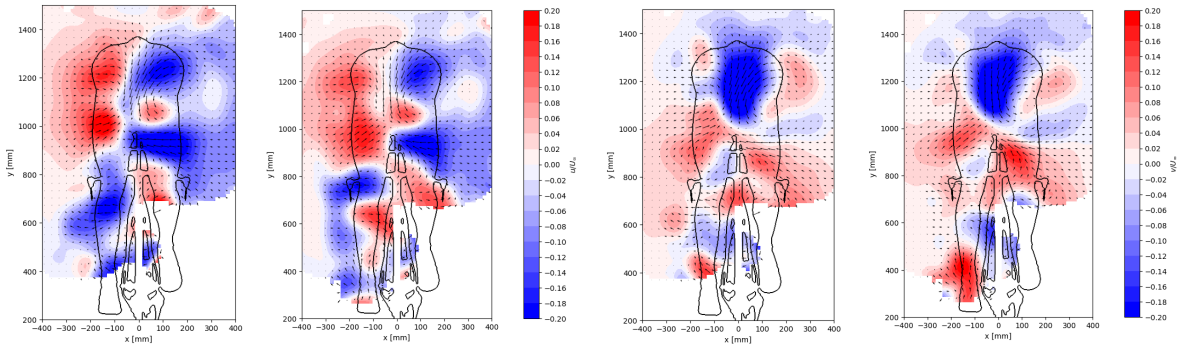

(a) Bare - u/U_∞ **(b)** Zigzag legs - u/U_∞ **(c)** Bare - v/U_∞ **(d)** Zigzag legs - v/U_∞

Figure E.6: The lateral and vertical velocity flow fields of the zigzag strip on the lower legs of the Symmetric GCM at $18\ m/s$